GFZ Helmholtz Centre Potsdam

Institute of Geosciences

Universität Potsdam

Integrated Approaches to Earthquake Forecasting:

Insights from Coulomb Stress, Seismotectonics, and Aftershock Sequences

Shubham Sharma

October, 2023

Cumulative dissertation
to obtain the academic degree
"doctor rerum naturalium" (Dr. rer. nat.)
in the scientific discipline of Geophysics
Date of disputation 08.05.2024

Submitted to the
Faculty of Mathematics and Natural Sciences
at the University of Potsdam, Germany

Supervisors
Priv. Doz. Dr. Sebastian Hainzl
apl. Prof. Dr. Gert Zöller

Reviewers
Priv. Doz. Dr. Sebastian Hainzl
apl. Prof. Dr. Gert Zöller
Prof. Dr. Eugenio Lippiello (External)

Examination Committee Members
apl. Prof. Dr. Gert Zöller
Priv. Doz. Dr. Sebastian Hainzl
Prof. Dr. Annegret Thieken (Chairwoman)
Prof. Dr. Torsten Dahm
Prof. Dr. Fabrice Cotton

Published online on the
Publication Server of the University of Potsdam:
https://doi.org/10.25932/publishup-63612
https://nbn-resolving.org/urn:nbn:de:kobv:517-opus4-636125

In loving memory of my grandmother, I dedicate this work as a heartfelt tribute to her unwavering love and everlasting impact on my life.

Acknowledgements

My research journey has been a lengthy and challenging adventure, brimming with both exhilarating moments and moments of disappointment. Nevertheless, I consider myself fortunate to have crossed paths with remarkable individuals who have not only provided unwavering support but also served as a profound source of motivation throughout every step of my progress.

I owe a profound debt of gratitude to my supervisor, PD Dr. Sebastian Hainzl, who provided unwavering support and guidance throughout my journey as a researcher. Under his guidance, I learned to cultivate critical scientific thinking, he proved to be an invaluable companion for discussing my scientific concepts, and he extended his support during challenging times, without which completing my thesis would have been impossible.

I must also extend my appreciation to my co-supervisor, apl. Prof. Dr. Gert Zöller, whose constructive criticism and insightful comments on my work continually motivated me to uncover the practical applications of my methodology in statistical seismology. None of this would have been possible without the guidance and motivation of Prof. Supriyo Mitra from IISER Kolkata. He has consistently served as the guiding star on my research career path, and his advice remains a source of great value to me.

I would like to express my gratitude for the support provided by the Deutsche Forschungsgemeinschaft (DFG) through the NatRiskChange research training group during my Ph.D. I am sincerely thankful for the valuable insights I acquired from the NatRiskChange group's members, stemming from both formal and informal scientific discussions that occurred during our collaborative efforts, group projects, and retreats.

I wish to express my sincere appreciation to the German Research Center for Geosciences (GFZ) for providing a remarkable research environment and fostering connections with a multitude of highly motivated researchers. I am deeply thankful to Prof. Dr. Torsten Dahm, Dr. Theresia Petrow, Susanne Köster, and the welcome center for their indispensable support in managing the intricate administrative responsibilities. I wish to extend my heartfelt gratitude to Dr. Rongjiang Wang for his assistance in guiding me through the PSGRN+PSCMP code, which formed the base of this research. Additionally, I am extremely grateful to my colleague, friend, and neighbor, Abhirup Banerjee, for his company during the pandemic. Furthermore, I owe a special debt of thanks to my dear friend and fellow adventurer in Potsdam, Pouria Marzban. His unwavering support and friendship not only made my stay in Germany more enjoyable but also eased the difficulties that could have arisen during my time here. His presence was instrumental in turning my experience into a memorable journey.

I'd also like to express my gratitude to my colleague and friend, Johannes Joscha Vogel and Ajay Kumar for their warm hospitality during my time in Potsdam. To my colleagues and friends from GFZ and the University — Jamal, Lorenzo, Reza, Melanie, Matthias, Lisa, and Behnam — I extend my heartfelt thanks for your unwavering support and kindness. In addition, special acknowledgment to Malte Metz for his assistance in translating the abstract into German. Your contributions have been greatly appreciated.

I want to express my heartfelt gratitude to my family for providing unwavering emotional support that served as a driving force behind my journey. I am deeply appreciative of all my teachers, who played a pivotal role in nurturing my creative curiosity. Lastly, I extend thanks to myself for displaying resilience during the challenging period of the pandemic, ultimately culminating in reaching this significant milestone today.

Abstract

A comprehensive study on seismic hazard and earthquake triggering is crucial for effective mitigation of earthquake risks. The destructive nature of earthquakes motivates researchers to work on forecasting despite the apparent randomness of the earthquake occurrences. Understanding their underlying mechanisms and patterns is vital, given their potential for widespread devastation and loss of life. This thesis combines methodologies, including Coulomb stress calculations and aftershock analysis, to shed light on earthquake complexities, ultimately enhancing seismic hazard assessment.

The Coulomb failure stress (CFS) criterion is widely used to predict the spatial distributions of aftershocks following large earthquakes. However, uncertainties associated with CFS calculations arise from non-unique slip inversions and unknown fault networks, particularly due to the choice of the assumed aftershocks (receiver) mechanisms. Recent studies have proposed alternative stress quantities and deep neural network approaches as superior to CFS with predefined receiver mechanisms. To challenge these propositions, I utilized 289 slip inversions from the SRCMOD database to calculate more realistic CFS values for a layered-half space and variable receiver mechanisms. The analysis also investigates the impact of magnitude cutoff, grid size variation, and aftershock duration on the ranking of stress metrics using receiver operating characteristic (ROC) analysis. Results reveal the performance of stress metrics significantly improves after accounting for receiver variability and for larger aftershocks and shorter time periods, without altering the relative ranking of the different stress metrics.

To corroborate Coulomb stress calculations with the findings of earthquake source studies in more detail, I studied the source properties of the 2005 Kashmir earthquake and its aftershocks, aiming to unravel the seismotectonics of the NW Himalayan syntaxis. I simultaneously relocated the mainshock and its largest aftershocks using phase data, followed by a comprehensive analysis of Coulomb stress changes on the aftershock planes. By computing the Coulomb failure stress changes on the aftershock faults, I found that all large aftershocks lie in regions of positive stress change, indicating triggering by either co-seismic or post-seismic slip on the mainshock fault.

Finally, I investigated the relationship between mainshock-induced stress changes and associated seismicity parameters, in particular those of the frequency-magnitude (Gutenberg-Richter) distribution and the temporal aftershock decay (Omori-Utsu law). For that purpose, I used my global data set of 127 mainshock-aftershock sequences with the calculated Coulomb Stress (ΔCFS) and the alternative receiver-independent stress metrics in the vicinity of the mainshocks and analyzed the aftershocks properties depend on the stress values. Surprisingly, the results show a clear positive correlation between the Gutenberg-Richter b-value and induced stress, contrary to expectations from laboratory experiments. This observation highlights the significance of structural heterogeneity and strength variations in seismicity patterns. Furthermore, the study demonstrates that aftershock productivity increases nonlinearly with stress, while the Omori-Utsu parameters c and p systematically decrease with increasing stress changes. These partly unexpected findings have significant implications for future estimations of aftershock hazard.

The findings in this thesis provides valuable insights into earthquake triggering mechanisms by examining the relationship between stress changes and aftershock occurrence. The results contribute to improved understanding of earthquake behavior and can aid in the development

of more accurate probabilistic-seismic hazard forecasts and risk reduction strategies.

Zusammenfassung

Ein umfassendes Verständnis der seismischen Gefahr und Erdbebenauslösung ist wichtig für eine Minderung von Erdbebenrisiken. Die zerstörerische Natur von Erdbeben motiviert Forscher dazu, trotz der scheinbaren Zufälligkeit der Erdbebenereignisse an Vorhersagen zu arbeiten. Das Verständnis der den Beben zugrunde liegenden Mechanismen und Muster ist angesichts ihres Potenzials für weitreichende Verwüstung und den Verlust von Menschenleben von entscheidender Bedeutung. Diese Arbeit kombiniert Methoden, einschließlich der Berechnung der Coulombschen Spannung und der Analyse von Nachbeben, um die Komplexitäten von Erdbeben besser zu verstehen und letztendlich die Bewertung der seismischen Gefahr zu verbessern.

Das Coulomb Spannungskriterium (CFS) wird oft verwendet, um die räumliche Verteilung von Nachbeben nach großen Erdbeben vorherzusagen. Jedoch ergeben sich Unsicherheiten bei der Berechnung von CFS aus nicht eindeutigen slip-inversion und der unbekannten Störungsnetzwerken, insbesondere aufgrund der Unsicherheit bezüglich der Nachbebenmechanismen (Empfänger). Neueste Studien deuten darauf hin dass alternative Spannungsgrößen und Deep-Learning-Ansätze gegenüber CFS mit vordefinierten Empfängermechanismen. Um diese Ergebnisse zu hinterfragen, habe ich 289 Slip-inversion uberlegensind aus der SRCMOD-Datenbank verwendet, um realistischere CFS-Werte für einen geschichteten Halbraum und variable Empfängermechanismen zu berechnen. Dabei habe ich auch den Einfluss von Magnitudenschwellenwerten, Gittergrößenvariationen und der Nachbeben-Dauer auf die vorhersagemöglichkeiten der Spannungsmetriken unter Verwendung der ROC-Analyse (Receiver Operating Characteristic) untersucht. Die Ergebnisse zeigen, dass die berudzsidtizung von variablen Empfangermechanism und größere Nachbeben und kürzere Zeiträume die vorhersagekraft steigern, wobei die relative Rangfolge der verschiedenen Spannungsmetriken nicht geändert wird.

Um die Coulomb Spannungsberechnungen genauer mit den Ergebnissen von Erdbebenstudien abzugleichen, habe ich die Quelleneigenschaften des Erdbebens von Kaschmir aus dem Jahr 2005 und seiner Nachbeben mit dem ziel, die Seismotektonik des NW-Himalaya Syntaxis zu entschlüsseln, detailliert untersucht. Ich habe gleichzeitig das Hauptbeben und seine größten Nachbeben unter Verwendung von seismischen Phaseneinsetzen relokalisiert und anschließend eine umfassende Analyse der Coulomb Spannungsänderungen auf den Bruchflächen der Nachbeben durchgeführt. Durch die Berechnung der Coulomb Spannungsänderungen an den während der Nachbeben aktivierten Störungen konnte ich herausfinden, dass alle großen Nachbeben in Regionen mit positiven Spannungsänderungen liegen, was auf eine Auslösung durch entweder ko-seismische oder post-seismische Verschiebungen des Hauptbebens hinweist.

Schließlich habe ich die Beziehung zwischen den durch Hauptbeben verursachten Spannungsänderungen und den damit verbundenen seismischen Parametern untersucht, insbesondere denen der Häufigkeits-Magnituden (Gutenberg-Richter) Verteilung und des zeitlichen Nachbebenabklingens (Omori-Utsu-Gesetz). Zu diesem Zweck habe ich meinen globalen Datensatz von 127 Hauptbeben-Nachbeben-Sequenzen mit den in der Umgebung der Hauptbeben berechneten Coulomb Spannungen (ΔCFS) zusammen mit den alternativen, empfänger-unabhängigen Spannungsmetriken, verwendet und die Eigenschaften in Abhängigkeit der Spannungswerte analysiert. Überraschenderweise zeigen die Ergebnisse eine klar positive Korrelation zwischen dem b-Wert der Gutenberg-Richter-Verteilung und der induzierten Spannung, was im Kontrast zu den Erwartungen aus Laborexperimenten steht. Diese Beobachtung unterstreicht die Bedeutung struktureller Heterogenitäten und Festigkeitsvariationen in seismischen Mustern. Darüber

hinaus zeigt die Studie, dass die Anzahl von Nachbeben nichtlinear mit der Spannung zunimmt, während die Omori-Utsu-Parameter c und p systematisch mit zunehmenden Spannungsänderungen abnehmen. Diese teilweise unerwarteten Ergebnisse haben bedeutende Auswirkungen auf zukünftige Abschätzungen der Nachbebengefahr.

Die Ergebnisse dieser Arbeit liefern wertvolle Einblicke in die Mechanismen der Erdbebenauslösung, indem sie die Beziehung zwischen Spannungsänderungen und dem Auftreten von Nachbeben untersuchen. Die Ergebnisse tragen zu einem besseren Verständnis des Verhaltens von Erdbeben bei und können bei der Entwicklung genauerer probabilistischer, seismischer Gefahreneinschätzungen und Risikominderungsstrategien helfen.

Contents

List of publications

This dissertation is based on the following publications.

P1. **Sharma, S.**, Hainzl, S., Zöeller, G., & Holschneider, M. (2020). Is Coulomb stress the best choice for aftershock forecasting?. *Journal of Geophysical Research: Solid Earth*, 125(9), e2020JB019553. https://doi.org/10.1029/2020JB019553

P2. Powali, D., **Sharma, S.**, Mandal, R., & Mitra, S. (2020). A reappraisal of the 2005 Kashmir (Mw 7.6) earthquake and its aftershocks: Seismotectonics of NW Himalaya. *Tectonophysics*, 789, 228501. https://doi.org/10.1016/j.tecto.2020.228501

P3. **Sharma, S.**, Hainzl, S., & Zöeller, G. (2023). Seismicity parameters dependence on mainshock-induced co-seismic stress. *Geophysical Journal International*, 235(1), 509-517. https://doi.org/10.1093/gji/ggad201

Further collaboration work (not included in this dissertation)

P4. Sharma, S., Mitra, S., **Sharma, S.**, Priestley, K., Wanchoo, S. K., Powali, D., & Ali, L. (2020). A report on broadband seismological experiment in the Jammu and Kashmir Himalaya (JAKSNET). *Seismological Research Letters*, 91(3), 1915-1926. https://doi.org/10.1785/0220190389

P5. Asayesh, B. M., Zafarani, H., Hainzl, S., & **Sharma, S.** (2023). Effects of large aftershocks on spatial aftershock forecasts during the 2017-2019 western Iran sequence. *Geophysical Journal International*, 232(1), 147-161. https://doi.org/10.1093/gji/ggac333

List of Tables

List of Figures

Chapter 1

Introduction

1.1 Background and Motivation

Earthquakes are natural events that can cause significant destruction and loss of life. Understanding and forecasting earthquakes is a crucial endeavor for mitigating their impact and ensuring the safety and resilience of affected communities. Over the years, scientists and researchers have made significant advancements in earthquake forecasting methodologies, utilizing various approaches and techniques. Large destructive mainshocks are always followed by aftershocks which can be equally destructive. Forecasting the rate of large earthquakes over long times and forecasting aftershocks (<100 km) over short periods of time (<1 year) are two major concerns. Both cases are important for mitigating hazards. Long term seismic forecasts are relevant for urban planning and building construction; and short term forecasts of aftershocks are relevant for rapid response measures and minimizing the damage already occured by the mainshock. This thesis focuses on Short-Term Aftershock (STA) forecasts that can be potentially efficient for mitigating hazards.

Multiple STA forecast approaches has been introduced from classical statistics (Gutenberg and Richter, 1944; Omori, 1895; Ogata, 1988), physics (King et al., 1994) or latest Machine Learning (ML) (Huang et al., 2018; Cao et al., 2021; Ridzwan and Yusoff, 2023; DeVries et al., 2018) based techniques. One approach that has gained considerable attention in earthquake forecasting is the use of emprical laws such as Gutenberg-Richter (GR) and Omori-Utsu (OU) law (Gutenberg and Richter, 1944; Utsu et al., 1995). This approach has been complemented by rate- and state-dependent (Dieterich, 1994) frictional modelling of earthquake initiation. A nonlinear response in earthquake nucleation times, following the Omori-Utsu law, is observed when a sudden stress jump occurs for a population of faults in the nucleation regime (Dieterich, 1994; Cocco et al., 2010). The application of this model to empirical data has provided a satisfactory explanation for the observed phenomena (Dieterich et al., 2000; Toda et al., 2002) and reasonable estimates for the regional stressing rate (Gross and Kisslinger, 1997; Gross, 2001). Another aspect of earthquake forecasting is the understanding of seismotectonics of the region. Understanding the geological and geophysical processes underlying seismic activity is crucial for identifying earthquake-prone regions and estimating their potential for future earthquakes. By combining the perspectives of both physical and statistical approaches along with the regional seismotechtonics, a comprehensive understanding of earthquake processes and the improved accuracy of their forecasts might be achieved.

My thesis titled "Integrated Approaches to Earthquake Forecasting: Insights from Coulomb Stress, Seismotectonics, and Aftershock Sequences" aims to explore the synergies between these three key components of earthquake forecasting. By integrating the study of Coulomb stress, seismotectonics, and aftershock statistics, the thesis seeks to provide a comprehensive understanding of earthquake processes and improve the accuracy of earthquake forecasting models. In particular, I address the questions (i) whether or not the classical Coulomb stress calculations is the best metric for aftershock hazard and (ii) how the freuency-magnitude relation

and aftershock decay depend on the stress changes. The research conducted in this thesis will hopefully contribute to the advancement of earthquake science and provide valuable insights for seismic hazard assessment and mitigation strategies.

In the next section, I briefly explain the theoretical aspects of advancing Coulomb stress analysis and aftershock forecasting along with the statistical features of the earthquake frequency and aftershock decay. I will also revisit the 2005 Kashmir earthquake and its aftershocks for an exemplary application of advanced Coulomb stress calculations, before the subsequent chapter describe my main findings in detail.

1.2 Stress tensor

The stress tensor provides a powerful mathematical representation of the stress state within the Earth's crust and elucidates how the accumulated stress and deformation contribute to seismic events. When considering an infinitesimal plane (Figure 1.1a) with arbitrary orientation within a homogeneous elastic medium in static equilibrium, we can define the orientation of the plane using its unit normal vector, represented as $\hat{n}$. The force per unit area exerted by the side of the cube (plane) is referred to as the "traction" and can be represented by the vector $t(\hat{n}) = (t_x, t_y, t_z)$.

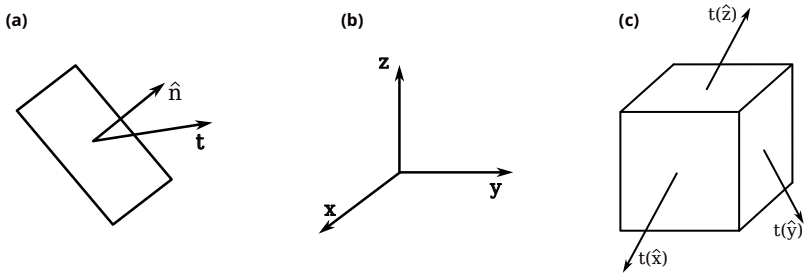

Figure 1.1: Traction vector characterizes the forces acting on an infinitesimal (a) plane or (c) cube in a given (b) cartesian coordinate system.

The orientation of an infinitesimal plane affects the traction vector, requiring a comprehensive representation of forces. This is achieved through the utilization of a stress tensor, denoted as τ. The stress tensor in a Cartesian coordinate system (Figure 1.1b-c) is represented by

$$\tau = \begin{bmatrix} t_x(\hat{x}) & t_x(\hat{y}) & t_x(\hat{z}) \\ t_y(\hat{x}) & t_y(\hat{y}) & t_y(\hat{z}) \\ t_z(\hat{x}) & t_z(\hat{y}) & t_z(\hat{z}) \end{bmatrix} = \begin{bmatrix} t_{xx} & t_{xy} & t_{xz} \\ t_{yx} & t_{yy} & t_{yz} \\ t_{zx} & t_{zy} & t_{zz} \end{bmatrix} \tag{1.1}$$

The stress tensor, τ is a linear operator that generates the traction vector, t by performing multiplication with a normal vector, $\hat{n}$. This fundamental property demonstrates that the stress tensor exists independently of any coordinate system. Moreover, a singular stress tensor can be utilized to calculate various scalar stress metrics, as elaborated in Chapter 2, Section 2.3.

1.3 Coulomb Failure Stress

Coulomb failure stress is a scalar quantity used to explain the spatial distribution of aftershocks after a mainshock. It is the most common method to calculate the static stress state of a fault and is defined as

$$CFS = \tau_\beta - \mu(\sigma_\beta - p) \tag{1.2}$$

where τ_β is the shear stress in slip direction on the fault plane, σ_β is the normal stress (positive for compression), μ is the coefficient of friction, and p is the pore fluid pressure. When CFS exceeds a threshold, failure is expected to occur on the fault plane (Figure 1.2). Figure 1.3 shows the changes in Coulomb stress (ΔCFS) for the 2005 Kashmir earthquake where the receiver faults (aftershocks) are assumed to have the same mechanism (strike=324.84, dip=29.00, rake=95.59) as the mainshock. Positive values of ΔCFS are associated with the faults with ΔCFS>0 that are therefore become more likely to fail and Vice-versa, faults with ΔCFS<0 are less likely to fail after the mainshock.

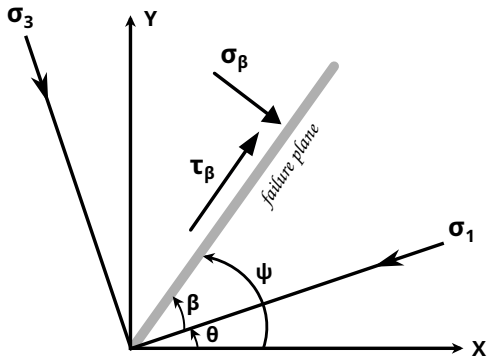

Figure 1.2: Illustration of stresses acting on faults (King et al., 1994), where σ_1 and σ_3 are principal stresses acting along the principal axes , and τ_β and σ_β are stresses acting along and normal to the failure plane, respectively.

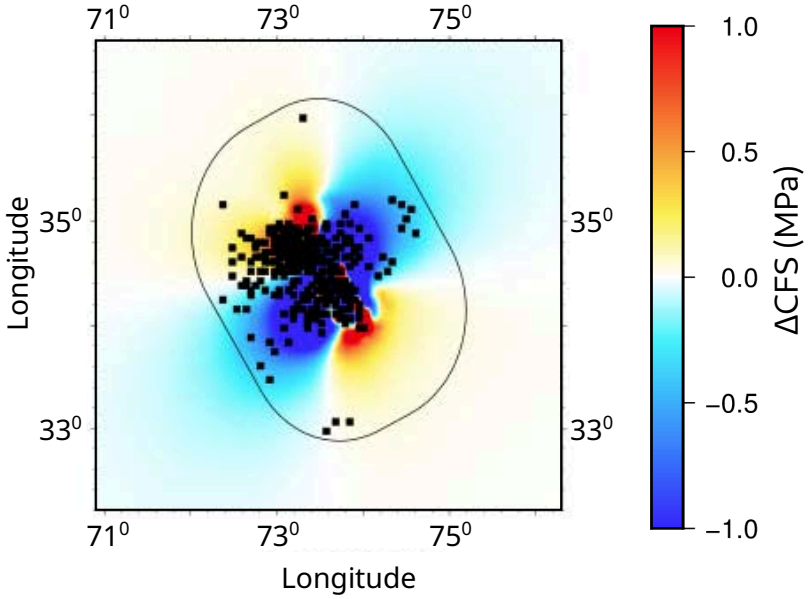

Figure 1.3: Coulomb stress change at the depth of mainshock (10 km) for the 2005 Kashmir earthquake, where black dots are aftershocks occurred within the first year after the mainshock and the black line marks the distance of 100 km from the mainshock fault plane.

1.3.1 Classical approach

Many studies have been conducted to show the correlation between static CFS changes and the spatial aftershock distribution (King et al., 1994; Harris, 1998; Stein, 1999; Steacy et al., 2005a). The method worked well in earlier studies (Toda et al., 1998; Parsons et al., 1999). However, later studies critized the approach because it fails to explain seismic silence in stress shadow

areas with ΔCFS < 0 (Felzer and Brodsky, 2005; Harris and Simpson, 2002) and dynamic stress triggering (Felzer and Brodsky, 2006).

Ideally, accurate Coulomb stress calculations require faults with well-known geometry. However, in cases where the fault geometry is poorly constrained or unknown, an alternative approach is to select faults with optimal oriented planes (OOP) that maximize the total Coulomb stress consisting of the background stress field and mainshock induced ΔCFS. Both of these approaches have limitations, including challenges posed by poorly constrained fault plane geometries, unknown background stress fields, and blind faults. To address these challenges, Steacy et al. (2005b) recommended to fix the strike of the faults based on the regional fault trend. This approach provides a practical solution when fault geometry is uncertain. On the other hand, Hainzl et al. (2010b) suggested using a distribution of receiver fault orientations to estimate ΔCFS. By considering a range of fault orientations, this method helps minimize the impact of stress shadows, as observed in earthquake occurrences. The recommendations from Steacy et al. (2005b) and Hainzl et al. (2010b) offer valuable insights into overcoming the limitations associated with fault geometry and stress field uncertainties in Coulomb stress calculations.

1.3.2 An alternative approach

During the early stages of this thesis work, around 2017-2018, the validity of CFS came into question. Meade et al. (2017) and DeVries et al. (2018) conducted studies that proposed alternative stress metrics and demonstrated the superior performance of deep neural network (DNN) techniques compared to CFS. However, the suggestion of DNN by DeVries et al. (2018) was later scrutinized by Mignan and Broccardo (2019), who proposed a simpler and more effective distance-based approach. The alternative metrics suggested are different variants of the full stress tensor or Coulomb failure criterion. These metrics have been calculated using the stress tensor in equation 1.1 and are discussed in section 2.3 of Chapter 2. In light of these discussions, my research, described in detail in Chapter 2, builds upon the findings of Meade et al. (2017) and challenges the previous results. I perform a comprehensive analysis by utilizing more appropriate stress calculations and employing alternative tests to assess their efficacy. The aim is to provide a thorough evaluation of the existing approaches and provide new insights to the field.

1.4 Seismotectonics of M_w 7.6, 2005 Kashmir Earthquake

The 2005 Kashmir Earthquake occurred near the confluence of the Karakorum, Pamir, and Hindukush ranges at the northwestern syntaxis of the Himalayas (Figure 1.4). This seismic event resulted in a surface rupture of approximately $75km$, and the slip inversion based on teleseismic waveforms indicated a bilateral rupture velocity of around $2km/s$ and an average fault offset of approximately $4m$ (Avouac et al., 2006).

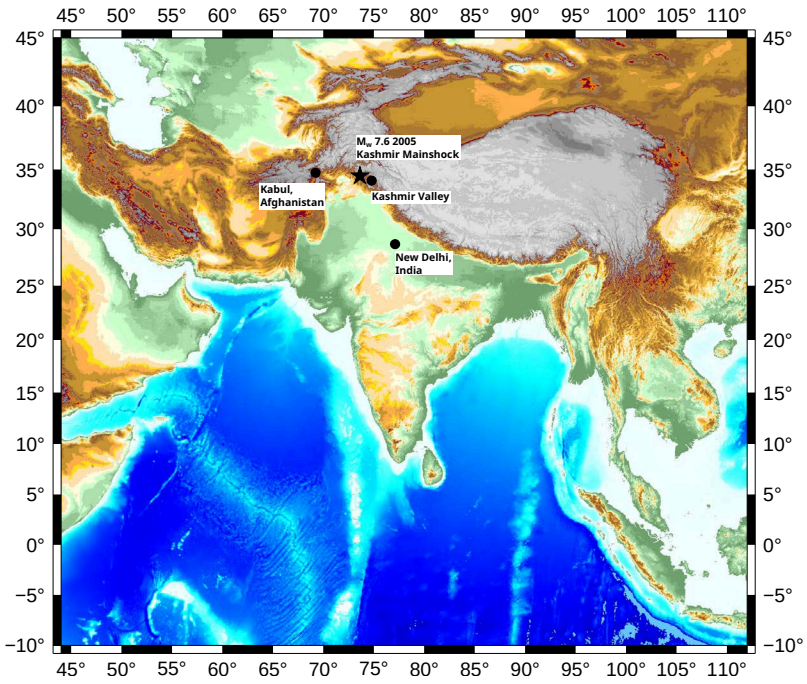

Figure 1.4: M_w7.6, 8 October 2005 Kashmir mainshock.

In this study, we revisited the earthquake's source properties to enhance our understanding of its characteristics. To achieve this, both the mainshock and aftershocks were simultaneously relocated to investigate their spatial relationship. Additionally, a back-projection technique was employed on teleseismic data to model the spatio-temporal evolution of the mainshock fault rupture. The focal mechanism and depth of both the mainshock and aftershocks with a moment magnitude ($M_w \geq 5.0$) were constrained using centroid source mechanism modeling.

Moreover, this information was correlated with Coulomb failure stress changes resulting from the mainshock rupture on aftershock fault planes. The objective was to verify the application of methods developed in the initial part of this research, and to assess the potential influence of the mainshock on subsequent aftershock activity. Through this comprehensive analysis, shown in detail in Chapter 3, I aim to enhance our knowledge of earthquake dynamics and contribute valuable insights to the broader understanding of seismic events and their implications.

1.5 Seismicity parameters

Statistical seismology plays a crucial role in understanding the aftershock occurrence and their distributions. The two most important emprical relationships that describe the statistical properties of earthquakes in terms of occurrence rates and magnitudes are the Gutenberg-Richter (GR) (Gutenberg and Richter, 1944) and Omori-Utsu (OU) (Utsu et al., 1995) laws. The GR law describes the frequency-magnitude distribution of earthquakes. It states that the number of earthquakes of a given magnitude follows an exponential relationship. Mathematically, the number N of earthquakes with a magnitude larger or equal to M is given by

$$\log_{10} N = a - bM \tag{1.3}$$

with constants a and b, where the b-value describes the relative frequency of smaller to larger events. The seismic information in earthquake catalogs is incomplete for small earthquake magnitudes, hence a magnitude cut-off (M_c) is needed to account for it. For the example of the 2004 M 6 Parfield earthquake, Figure 1.5a shows the evolution of the aftershock occurrences after the mainshock and figure 1.5b shows the corresponding frequency-magnitude distribution

along with a GR-law fit.

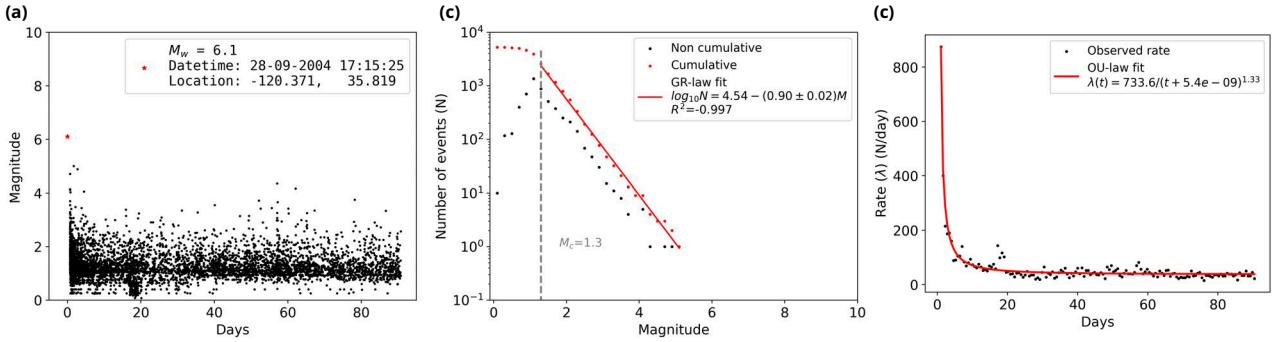

Figure 1.5: (a) Mainshock-aftershock sequence of the Sept. 28, 2004, Parkfield (California) earthquake: (a) Magnitude versus time after the mainshock. (b) Frequency-magnitude distribution where the vertical dashed line indicates the completeness magnitude of the earthquake data and the solid red line represents the GR law fit to the distribution. (c) Decay rate of the aftershock sequence following the mainshock sequence, where the solid red line represents the OU-law fit to the observed rate.

The OU law relates the rate of aftershocks following a mainshock to the time elapsed since the mainshock. It states that the frequency of aftershocks (aftershock rate, λ) decreases over time according to a power-law decay. Figure 1.4c shows the decay of aftershocks rate with time since the Parkfield mainshock along with a fit of the OU-law

$$\lambda(t) = K/(t + c)^p \tag{1.4}$$

where constant K refers to the productivity, c to the delay time of the power-law onset, and exponent p describes the rate of the aftershock decay.

1.5.1 Stress correlation of seismicity parameters

Seismicity parameters, namely b-, p-, and c-values, exhibit significant variations on a global scale, with fluctuations occurring over various timescales (El-Isa, 2013).While the global average of b hovers close to 1, individual cases show significant fluctuations around this value. In laboratory rock experiments, b is found to be negatively correlated to stress (Scholz, 1968; Smith, 1981). Therefore, the b-value variations on local scale has been utilized as a potential precursor to large earthquakes (Nanjo et al., 2012). Notably, recent studies suggest that the b-value can act as a stress sensor in the vicinity of earthquake focal areas (Nanjo and Yoshida, 2021; Scholz, 2015; Schorlemmer et al., 2005).

Extensive research has focused on stress-dependent variations of the GR parameters, but there is a notable lack of studies examining the same for the OU parameters. The present study aims to address this gap by investigating the direct correlation between b, c, and p values and the mainshock induced stresses. To accomplish this, I utilized a comprehensive global dataset comprising 127 mainshock-aftershock sequences, I seek to gain valuable insights into the aftershock patterns and their relationship to the stress distribution surrounding the mainshocks.

Furthermore, the findings from this study, which are described in detail in Chapter 4, do not only contribute to a deeper understanding of aftershock dynamics but also hold potential implications for future earthquake hazard assessment. By elucidating the stress-dependent variations of key seismicity parameters, this research may aid in the development of more accurate and region-specific seismic hazard models, ultimately assisting in mitigating the impact of future seismic events on vulnerable communities and infrastructures.

1.6 Structure of thesis

The flowchart in Figure 1.6 provides a concise outline of thesis which shows the logical progression of PhD work:

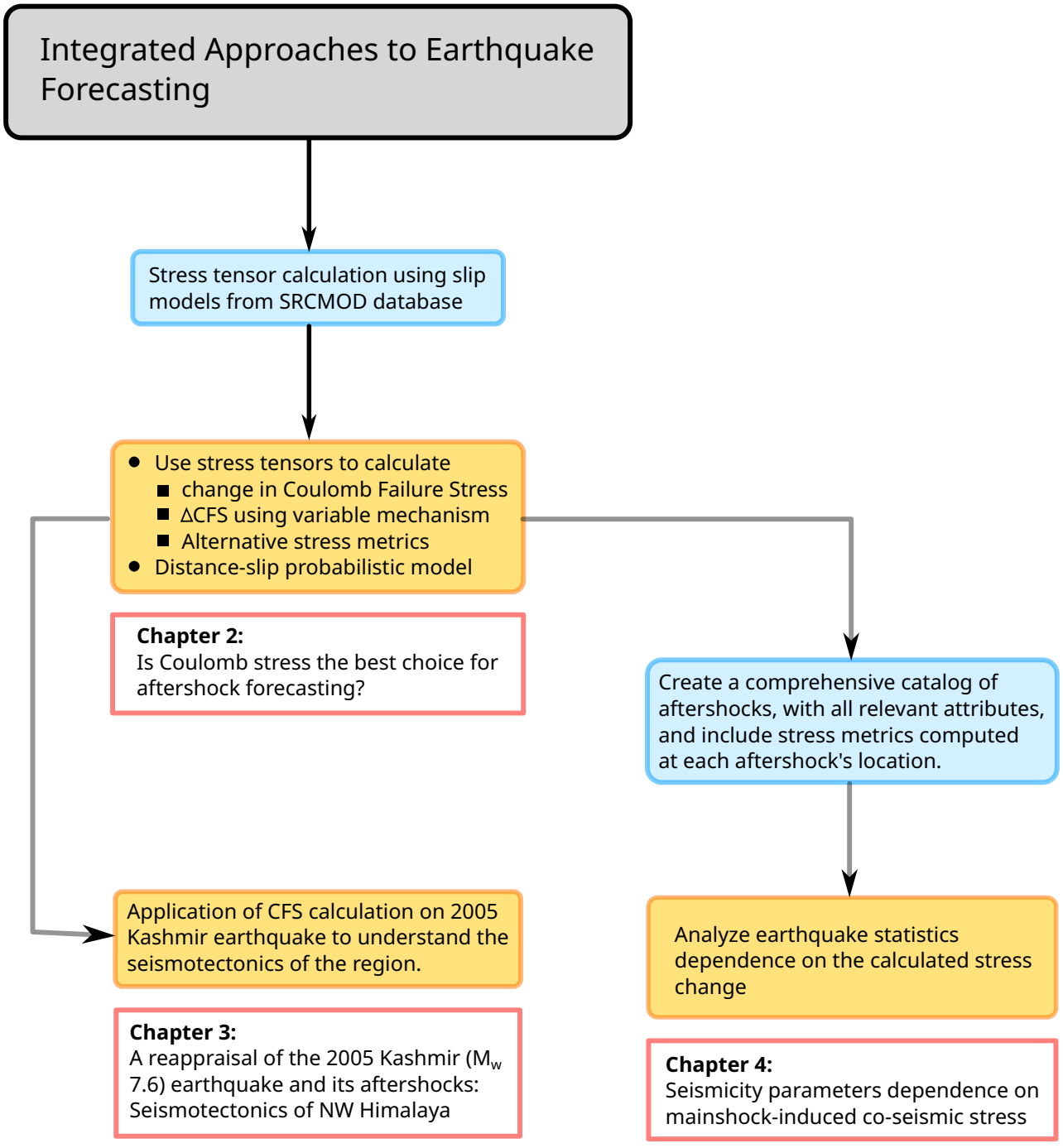

Figure 1.6: Thesis flowchart

1.6.1 Outline of thesis

This thesis integrates multiple approaches, including Coulomb stress analysis, seismotectonics, and statistical analysis of aftershock sequences. By combining these approaches, a comprehensive understanding of stress calculations and their relation to aftershock properties can be achieved, which might help to improve future aftershock forecasting.

1.6.2 Overview of publications and authors contribution

Paper 1. **Sharma, S.**, Hainzl, S., Zöeller, G., & Holschneider, M. (2020). Is Coulomb stress the best choice for aftershock forecasting?. *Journal of Geophysical Research: Solid Earth*, 125(9), e2020JB019553. https://doi.org/10.1029/2020JB019553

This paper focuses on refining the calculations of Coulomb Failure Stress (CFS) and exploring its applicability in predicting aftershocks. The study challenges previous results by using more realistic CFS calculations and alternative tests. Sensitivity tests and additional forecasts of aftershock numbers based on different stress metrics are performed. The findings contribute to improving the understanding and accuracy of aftershock forecasting.

My contribution: Formulated the study, carried out analysis and prepared the figures, and took the lead in writing the first draft of manuscript. All authors discussed the results, drew conclusions and provided the feedback to improve the manuscript. All authors were involved in deciding the context and interpretation of results.

Paper 2. Powali, D., **Sharma, S.**, Mandal, R., & Mitra, S. (2020). A reappraisal of the 2005 Kashmir (Mw 7.6) earthquake and its aftershocks: Seismotectonics of NW Himalaya. *Tectonophysics*, 789, 228501. https://doi.org/10.1016/j.tecto.2020.228501

The second paper examines the 2005 Kashmir earthquake and its aftershocks, focusing on source properties and seismotectonic analysis. The earthquake occurred in a complex region characterized by syntaxis structures and active faults. The study includes relocation, spatio-temporal evolution analysis, back-projection of teleseismic data, modeling of mainshock rupture, and computation of Coulomb failure stress changes. The results are combined with regional tectonics to develop a seismotectonic model of the northwest Himalayan syntaxis.

My contribution: Relocation the mainshock and its largest aftershocks (M_w>5.0), and calculation of ΔCFS. I was also involved in preparing the figures for the manuscript. SM supervised and conceptualised the study along reviewing and editing the manuscript. All authors discussed the results, drew conclusions, and provided critical feedback to the manuscript text.

Paper 3. **Sharma, S.**, Hainzl, S., & Zöeller, G. (2023). Seismicity parameters dependence on mainshock-induced co-seismic stress. *Geophysical Journal International*, 235(1), 509-517. https://doi.org/10.1093/gji/ggad201

The third paper explores the variations of Gutenberg-Richter (GR) and Omori-Utsu (OU) parameters in response to induced stress changes and rupture distance. The GR and OU laws are fundamental in explaining earthquake frequency-magnitude distribution and aftershock occurrence. The study analyzes a dataset of 127 mainshock-aftershock sequences and considers Coulomb Failure Stress changes and receiver-independent stress metrics. The results reveal systematic stress- and distance-dependent variations of the GR and OU parameters, providing valuable insights for aftershock hazard estimations.

My contribution: Formulated the study, collected and processed the datasets, carried out analysis and prepared the figures, and took the lead in writing the first draft of manuscript. All authors discussed the results, drew conclusions and provided the feedback to improve the manuscript. All authors were involved in deciding the context and interpretation of results.

Chapter 2

Is Coulomb stress the best choice for aftershock forecasting?

Abstract

The Coulomb failure stress (CFS) criterion is the most commonly used method for predicting spatial distributions of aftershocks following large earthquakes. However, large uncertainties are always associated with the calculation of Coulomb stress change. The uncertainties mainly arise due to non-unique slip inversions and unknown receiver faults, especially for the latter, results are highly dependent on the choice of the assumed receiver mechanism. Based on binary tests (aftershocks yes/no), recent studies suggest that alternative stress quantities, a distance-slip probabilistic model as well as deep neural network (DNN) approaches all are superior to CFS with predefined receiver mechanism. To challenge this conclusion, which might have large implications, we use 289 slip inversions from SRCMOD database to calculate more realistic CFS values for a layered-half space and variable receiver mechanisms. We also analyze the effect of the magnitude cutoff, grid size variation, and aftershock duration to verify the use of receiver operating characteristic (ROC) analysis for the ranking of stress metrics. The observations suggest that introducing a layered-half space does not improve the stress maps and ROC curves. However, results significantly improve for larger aftershocks and shorter time periods, but without changing the ranking. We also go beyond binary testing and apply alternative statistics to test the ability to estimate aftershock numbers which confirm that simple stress metrics perform better than the classic Coulomb failure stress calculations and are also better than the distance-slip probabilistic model. [1]

- Our tests for many mainshocks indicate that considering the variability of aftershock mechanisms significantly improves Coulomb forecasts.
- A distance-slip probabilistic model outperforms all stress based metrics concerning the forecast of the aftershock area.
- The best forecasting metric for aftershock forecasting is simple shear scalars.

[1] Originally published as (P1): Sharma, S., Hainzl, S., Zöeller, G., & Holschneider, M. (2020). Is Coulomb stress the best choice for aftershock forecasting?. *Journal of Geophysical Research: Solid Earth*, 125(9), e2020JB019553. https://doi.org/10.1029/2020JB019553.

2.1 Introduction

Large earthquakes are almost always followed by a sequence of aftershocks in the first months to years, which might themselves be destructive as e.g. in the case of the 2011 M_w6.2 Christchurch event which was triggered by the M_w7.1 Darfield mainshock (Stramondo et al., 2011). It is generally accepted that aftershocks result from stress changes induced by the mainshock. In particular, the Coulomb Failure Stress (CFS) is commonly used as scalar quantification of the stress state. It is defined as

$$CFS = \tau - \mu(\sigma - p) \tag{2.1}$$

where τ is the shear stress in slip direction on the fault plane, σ is the normal stress (positive for compression), μ is the coefficient of friction, and p is the pore fluid pressure. Positive CFS changes, ΔCFS>0, indicate areas of potential aftershock activity, while no aftershocks are expected in regions with ΔCFS<0. Many studies have demonstrated a clear correlation of the spatial aftershock pattern with static CFS changes calculated based on slip models (King et al., 1994; Harris, 1998; Stein, 1999; Steacy et al., 2005a). However, the applicability is still ambiguous, especially because of the lack of observational evidence for seismic quiescence in stress shadow areas associated to ΔCFS>0 (Felzer and Brodsky, 2005; Harris and Simpson, 2002) and the missing effect of dynamic stress triggering (Felzer and Brodsky, 2006).

In general, ΔCFS calculations rely on information that contains large uncertainties, such as non-unique inversion of slip models (Hainzl et al., 2009), secondary stress triggering (Helmstetter et al., 2005), and unknown receiver fault mechanisms. CFS calculations require a definition of the fault geometry and slip direction to calculate the Coulomb stress. This is typically done by resolving stress (1) on faults with known geometry, or (2) on optimally oriented planes (OOP) having maximum total Coulomb stress. Both approaches are limited either due to poorly constrained fault geometries, ignoring blind faults that could pose significant threat, or to an unknown background stress field. To account for these problems, Steacy et al. (2005b) suggested to fix the strike according to the regional fault trends and vary dip and rake to maximize the total stress tensor, while Hainzl et al. (2010b) proposed to use a distribution of receiver fault orientation to estimate the ΔCFS net effect. As a result, stress shadows are less pervasive in agreement with observations. Statistical space-time seismicity models have also been developed based on ΔCFS calculations (so-called hybrid models), e.g. Bach and Hainzl (2012) implemented ΔCFS maps as spatial kernel in the epidemic-type aftershock sequence (ETAS) model, Steacy et al. (2013) combined the spatial constraints from Coulomb stress with the short term earthquake probability (STEP) model (Gerstenberger et al., 2005), and Cattania et al. (2014, 2015) implemented ΔCFS in the rate-state model of Dieterich (1994) accounting for uncertainties. Those models are shown to be successful in explaining the observed trends in seismicity (Cattania et al., 2018).

Recently, the use of CFS has been questioned in general by the studies of Meade et al. (2017) and DeVries et al. (2018) showing that CFS is clearly outperformed by alternative stress metrics and deep neural network (DNN) techniques. They used receiver operating characteristic (ROC) analysis to assess the ability to forecast aftershock areas. The results suggest that alternative stress metrics such as maximum shear and von-Mises stress are more accurate and reliable than CFS. Mignan and Broccardo (2019) recently questioned the results of the DNN approach and stress metrics, proposing a distance-based approach which is simpler and superior. In this study, we challenge the previous results by repeating the analysis with more appropriate stress calculations as well as alternative tests. In particular, we use all available slip inversions from SRCMOD database to calculate more realistic CFS values assuming layered-half spaces and variable receiver mechanisms. Furthermore, we explore the previously ignored effect of different magnitude cutoffs, grid size variations, and aftershock durations to verify the use of

ROC analysis for ranking the stress metrics. We also perform a sensitivity test for aftershock locations using Monte-Carlo simulations of catalogs with spatial uncertainties drawn form a Gaussian distribution around the real hypocenter. Because of limitations of the binary forecasts and the ROC analysis, we finally perform additional tests of forecasts of aftershock numbers based on the different stress metrics.

2.2 Data

We use finite-fault rupture models from the SRCMOD (`http://equake-rc.info/SRCMOD/`) database by Mai and Thingbaijam (2014). As of 27 November 2019, the database consist of 406 models from 188 earthquakes. However, in this study we use only a subset of 289 models related to 130 distinct earthquakes for which reviewed aftershock data were available. The slip models are based on single or joint inversion of seismic, geodetic and other available data.

We use the International Seismological Center (ISC) catalog and select all events occurred within one year and within 100 km horizontal distance to the mainshock fault, with a depth range from 0 to 50 km. The catalog is obtained in the form of a pickle file (binary format) taken from the released data of DeVries et al. (2018). These events are called aftershocks, despite the fact that some of them were probably not be related to the mainshock. The catalog covers the period between January 1, 1964 and November 30, 2012. Out of 1,689,845 total events in the reviewed catalog, selection yields 410,064 aftershocks for the analysis.

2.3 Stress metrics and distance model

The finite-fault rupture models are used to calculate stress changes in a region up to 100 km away from the rupture plane and from 0 to 50 km depth. We use the PSGRN+PSCMP tool by Wang et al. (2006) to calculate the stress tensor in a $5 \times 5 \times 5$ km gridded volume. Given the stress tensor, we calculate 5 different scalar quantifications. Additionally, we also use the distance-slip probabilistic model suggested by Mignan and Broccardo (2019) comparing the performance of stress based metrics:

1. ΔCFS on master fault orientation (MAS), where ΔCFS is calculated for a receiver mechanism identical to mainshock mechanism.

2. ΔCFS on optimally oriented planes (OOP), assuming a background stress field with principal stress components $\sigma_1 = 1$, $\sigma_2 = 0$ and $\sigma_3 = -2$ MPa, i.e. a differential stress of 3 MPa which is in agreement to the average stress drop of interplate earthquakes (Allmann and Shearer, 2009a). The orientation of the principle components is in a way that the stress field is optimally oriented for the mainshock rupture.

3. ΔCFS assuming fault variability (VM): Here the average ΔCFS-value is calculated for receiver faults with positive stress changes (no aftershocks are expected on other faults) according to

$$\overline{\Delta CFS} = \frac{1}{N_p} \sum_{i=1}^{N_p} \Delta CFS_i \cdot H(\Delta CFS_i) \tag{2.2}$$

   where H is a Heaviside function and $N_p = 1500$ is the number of random planes which are selected from a Gaussian distribution centered around the mainshock mechanism, with an assumed standard deviation of 30 degrees for strike, dip and rake.

4. Maximum Shear (MS)

$$\Delta\tau_{max}(\chi) = |\chi_1 - \chi_3|/2 \tag{2.3}$$

where, χ is the stress tensor and χ_1 and χ_3 are corresponding eigenvalues of the deviatoric stress tensor.

5. von-Mises stress (VMS)
$$\sqrt{3J_2} = \sqrt{I_1^2(\sigma) - 3I_2(\sigma)} \tag{2.4}$$
where, I_1 and I_2 are 1^{st} and 2^{nd} invariant of stress deviatoric tensor. VMS is a scaled version of second invariant of the deviatoric stress change tensor (DeVries et al., 2018). If VMS of a material under a load is equal or greater to the yield limit, then the material will yield.

6. Distance-slip probabilistic model (R), which was introduced by Mignan and Broccardo (2019) by a logistic regression based on average slip, d, and the minimum distance, r, between the fault and grid node. The probability $Pr(r, d)$ of earthquake occurrence in each grid is given by
$$\Pr(r, d) = \frac{1}{1 + e^{-(\beta_0 + \beta_1 \log r + \beta 2 \log d)}} \tag{2.5}$$
with parameters, $\beta_0 = 10.18 \pm 0.07$, $\beta_1 = -2.32 \pm 0.02$ and $\beta_2 = 1.16 \pm 0.01$ which were obtained by a fit to 75% of the data set.

In general, the stress metrics are calculated for a layered half-space, where the layering is based on the CRUST 2.0 (Bassin, 2000) velocity model. However, as a reference model we use the ΔCFS values calculated for a homogeneous half-space (MAS_0) with assumed Lamé's parameter $\lambda = \mu = 30$ Gpa. For the Coulomb stress calculations, we use the constant apparent friction model (Cocco and Rice, 2002), according to which the Coulomb-stress changes can be written as $\Delta CFS = \Delta\tau - \tilde{\mu}\Delta\sigma$ with the effective friction coefficient $\tilde{\mu} = (1 - B)\mu$, where B is the Skempton's coefficient. In our study, we use a value of $\tilde{\mu} = 0.4$ (King et al., 1994).

2.4 Methods

To evaluate the forecasting capability, we use the same binary classification method, i.e. receiver operating characteristic (ROC) analysis, which has been introduced in previous studies to rank the performance of metrics (DeVries et al., 2018; Meade et al., 2017). In ROC analysis, a two-by-two table (Fig. 2.1) is defined to compare results of model outcomes with observed aftershocks. For different thresholds, the number of true positive (TP), false positive (FP), true negative (TN), and false negative (FN) cases are counted and the true positive rate (TPR) and false positive rate (FPR) are calculated as
$$TPR = \frac{TP}{TP + FN} \tag{2.6}$$
$$FPR = \frac{FP}{TN + FP}. \tag{2.7}$$

The cutoff thresholds are defined by stress change values, where stress values are firstly arranged in ascending order before each stress value is used as a cutoff to calculate TPR and FPR. A test with random classification of binary data has equal rates of true-positive and false-positive classification. For such a case, the area under the curve (AUC) value of a ROC curve is equal to 0.5. A model that has AUC>0.5 is better than a random classifier. A model performing no better than a random classifier (AUC < 0.5) can be rejected. Therefore, we use

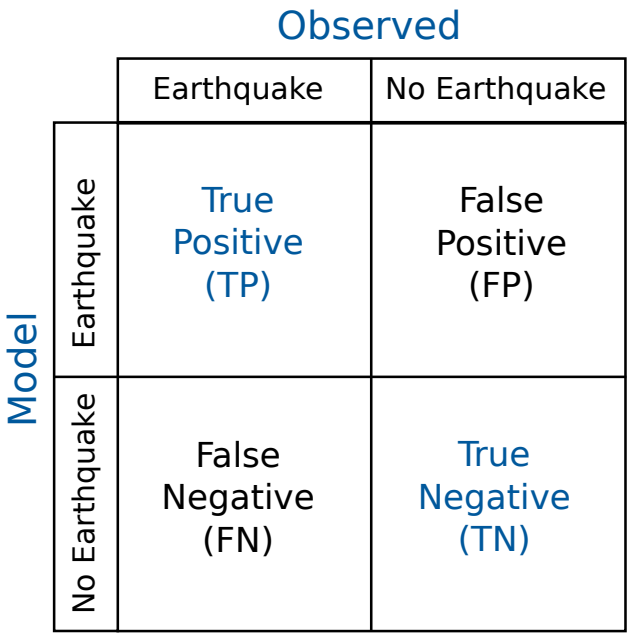

Figure 2.1: Table defining the true positive, true negative, false positive and false negative classes.

the ROC analysis to quantify the accuracy of our metrics for classifying areas with or without aftershocks.

The ROC-results can be biased by the inhomogeneity of the earthquake catalog due to, varying completeness over time and space, associated location uncertainties, as well as the occurrence of background activity which is not related to the mainshock.To test the potential effect of these issues, we also calculated AUC for different aftershock durations (aftershocks up to 1 year excluding first 24 hours, aftershocks in the first 3, 9 and 12 months after the main shock). Furthermore we explore the potential dependence of the results on the grid size (2.5, 5 and 10 km). We also perform a sensitivity test concerning the effect of location uncertainties by repeating the analysis for 25 randomized catalogs, where the original earthquake location is perturbed in each direction by a Gaussian distribution with standard deviation of 3 km.

Parsons (2020) recently discussed the fact that the imbalance of typical aftershock distributions with most areas lacking events inhibits resolving power of the ROC analysis. The binary ROC-test generally suffers from the fact that the test is dependent on the magnitude cutoff. This can be easily seen by considering the end-member case of an earthquake catalog which is complete to very low magnitudes. In this case, earthquakes would likely be recorded in all sub-volumes due to ongoing background activity which make the ROC results insensitive to the tested metric. The same holds for the opposite case that the threshold is too high and no aftershock is found. For intermediate cases, the test has some statistical power which depends on the cutoff value. For illustration of the dependence, we present in Sec. 2.5 the ROC-results for different magnitude cutoffs in the case of the 1999 Chi-Chi sequence. Later on we also present the results of a systematic test of the dependence of the AUC values on aftershock duration and magnitude cutoff for all slip models to find the best possible combination of both choices for forecasting aftershocks. The four chosen combinations are (1) aftershocks within the first year and a cutoff magnitude $M_m - 3$ with M_m being the mainshock magnitude, (2) aftershocks within the first 3 months without cutoff magnitude, (3) aftershocks within the first 3 months and cutoff magnitude $M_m - 3$, and (4) all aftershocks within one year without any cutoff magnitude.

Because of the general flaws of the ROC analysis, we additionally perform tests of the number forecasts as used in CSEP tests for seismicity models (Jordan, 2006). In this way, we test both the ability to forecast the activated area and the strength of the activation, which is

important for real hazard assessment. For this, we transform the spatial stress values into a spatial probability map of aftershock occurrences, which is based on the assumption of a linear dependence of the triggering potential on the stress change (if positive). In particular, the number of events in each grid cell (λ_n) is assumed to be proportional to the positive stress metric change ($S_n > 0$)

$$\lambda_n = c \cdot S_n \cdot H(S_n) \tag{2.8}$$

where, H is the Heaviside function. The normalization factor c is determined by the condition that summing over the whole region results in the total number of observed aftershocks

$$\sum_{n=1}^{N_g} \lambda_n = c \cdot \sum_{n=1}^{N_g} S_n \cdot H(S_n) = N_{obs} \tag{2.9}$$

where N_{obs} is the total number of observed aftershocks within one year after the mainshock and N_g is the number of grids cells in the region. Equation 2.8 and 2.9 can be used to determine the number of events in each grid cell. The likelihood of the observation in each cell is calculated by assuming a Poissonian process with an average rate λ_n. However, this approach would lead to an immediate falsification of a model, if the model predicts 0 activity in a grid cell, where one or more events occurred. While this is theoretically correct, real aftershock catalogs are potentially contaminated by background activity and incorrect locations. To minimize this problem, we distribute a fraction f of aftershocks homogeneously in space, i.e.

$$\lambda_n = \frac{N_{obs}}{\sum S_n \cdot H(S_n)} \cdot S_n \cdot H(S_n)(1-f) + \frac{N_{obs}}{N_{grid}} f \tag{2.10}$$

Here we choose a fraction ($f = 0.01$) which is uniformly distributed. The probability that N_n events will occur in a given time period and in the n^{th} grid with predicted rate λ_n is described by to the Poisson model with

$$P_n(N_n|\lambda_n) = \exp(-\lambda_n)\frac{\lambda_n^{N_n}}{N_n!} \tag{2.11}$$

and the joint-loglikelihood for all grid cells becomes

$$LL = \sum_{n=1}^{N_g} \log(P_n(N_n|\lambda_n)). \tag{2.12}$$

The joint log-likelihood has a negative value, and the values closer to zero indicate that forecasts are close to the observations.

2.5 Results

The stress tensors generated from the PSGRN+PSCMP (Wang et al., 2006) program are used to calculate the stress metrics described in Sec. 2.3. While our quantitative analysis is always done for the calculated stress in the whole gridded volume extending ± 100 km horizontally and from 0 to 50 km in depth, we first illustrate the calculations by selecting a specific depth level for one specific case, namely the slip distribution of 1999 Chi-Chi earthquake derived by Ma et al. (2001). In Fig. 2.2, we compare the stress maps generated by the different scalar stress calculations. Classical Coulomb stress calculations have positive and negative values which mark the regions with and without possible aftershocks, respectively. Correspondingly the values of MAS_0, MAS and OOP are negative and positive. In contrast, VM, MS and VMS are only positive. In order to compare the results on a same scale we use a Sigmoid filter $sig(10S_n - 1)$ (where $sig(x) = \frac{1}{1+e^{-x}}$). The stress maps are computed at the depth of

the mainshock hypocenter (7.5 km), where the epicenter of the mainshock is marked by the yellow star. The stress maps are compared to areas (black squares) where aftershocks occurred within one year after the mainshock in the depth interval of 7 ± 2.5 km. ΔCFS for MAS_0 and MAS (Fig. 2.2a-b respectively) show very little to no difference in their maps. However, the OOP-type Coulomb stress map (Fig. 2.2c) is significantly different from the former as verified in previous studies. There are few regions with high sigmoid values and no aftershocks, and few aftershocks occurring in the stress shadows. Fig. 2.2c, related to ΔCFS calculated on distributed planes shows maximum sigmoid values in the near fault region with decreasing values in the far field. Fig. 2.2e-f, which are related to maximum stress and von-Mises stress, indicate increased stress values in the near as well as the far field.

For the same example, we also performed a detailed analysis of the ROC test. The availability of a large number of aftershocks in the catalog of the Chi-Chi event makes it a suitable case for testing. The catalog is downloaded from ISC and contains 41,351 events. Unlike the catalog mentioned in Sec. 2.3 this is an updated catalog with significantly lower magnitude cutoff. Fig. 2.3a shows the aftershocks in a volume of 100 × 100 × 50 km plotted as magnitude versus time. We use the frequency magnitude distribution (Fig. 2.3b) to estimate the magnitude of completeness ($M_c \approx 2.2$). The ROC curves using all aftershocks and stress metrics in the gridded 100 × 100 × 50 km region are plotted in Fig. 2.3c. The analysis reveals that the best performing metrics are maximum shear (AUC = 0.744) and von-Mises stress (AUC = 0.749). The AUC value for the VM model with ΔCFS calculated on distributed planes is lower but also performs well (AUC = 0.721). For the specific case of the VM model, we additionally check the dependence of ROC curves on the magnitude cutoff (M_{cut}), aftershock duration, and grid size. The magnitude cutoff test (Fig. 2.3d) was performed for cutoff magnitudes of -1 (complete catalog), 2, 2.2 (M_c), 3, 4 and 5. A clear dependence of AUC on cutoff magnitude is observed, where AUC increases with increasing M_{cut}. This result indicates that larger aftershocks are in better agreement with the calculated stress maps.

The ROC analysis might be significantly biased by background activity which may begin to dominate with increasing time, as well as catalog incompleteness directly after the mainshock. To explore the potential effects, we also analyzed the ROC curves for different aftershock durations. We find that ignoring the first day, where the catalog is likely incomplete, does not have a significant effect (AUC of 0.696 instead of 0.698). However, ignoring later events does have a clear impact. The results for the first 3, 6, 9 and 12 months after the mainshock show that the AUC value systematically decreases (Fig. 2.3e) with increasing aftershock duration. The maximum AUC is observed for the aftershocks occurring within the 3 months of the mainshock. This indicates that the occurrence of background events in the later phases can significantly blur the test results. The dependence of AUC on grid size is tested by calculating the stress tensors at the centroid of cubes with edge length of 2.5, 5, and 10 km cells. Fig. 2.3f shows the resulting ROC curves for the VM stress metric calculated on different grid sizes. A systematic dependence of AUC on grid size is observed where smaller grid sizes increase the performance of the metric, indicating that the details in the stress maps are useful for aftershock forecasting.

To analyze whether the results for the Chi-Chi event can be generalized, we generated ROC curves for all 289 slip distributions and corresponding aftershock distributions. All resulting ROC curves are plotted in Fig. 2.4 (thin grey lines) for all stress metrics introduced in Sec. 2.3, where the thick blue line refers to the average curve for each stress metric. The average is calculated by averaging true positive rates in false positive rate bins. We then determined the corresponding AUC for the average curve. We observe no clear difference between the reference metric MAS_0 and MAS calculated for regional layered crust models (Fig. 2.3a-b). As expected, ΔCFS resolved on OOP results in a higher AUC (0.659) than MAS_0 and MAS (0.491 and 0.490 respectively). Furthermore, the AUC value (0.718) for ΔCFS calculated for variable mechanism (VM) is significantly higher as compared to the other CFS-metrics, but lower than the stress

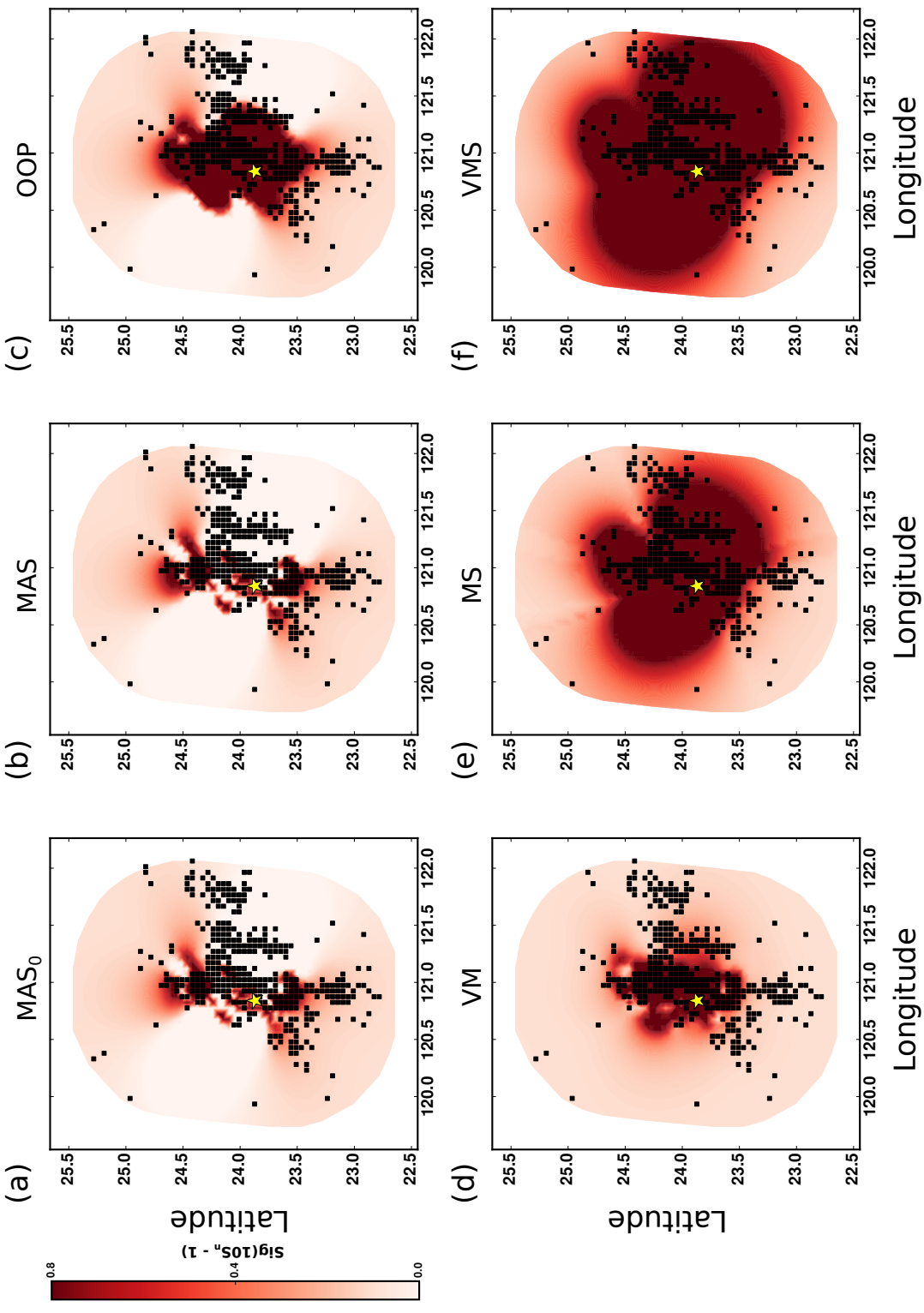

Figure 2.2: Stress maps calculated for 1999 Chi-Chi earthquake at the hypocentral depth of 7.5 km and passed to Sigmoid filter. (a) shows the reference model for comparison, (b-f) are stress metrics MAS, OOP, VM, MS and VMS respectively. Black squares indicate areas, where one or more aftershocks occurred in the $\pm$ 2.5 km depth interval. The yellow star refers to the mainshock epicenter.

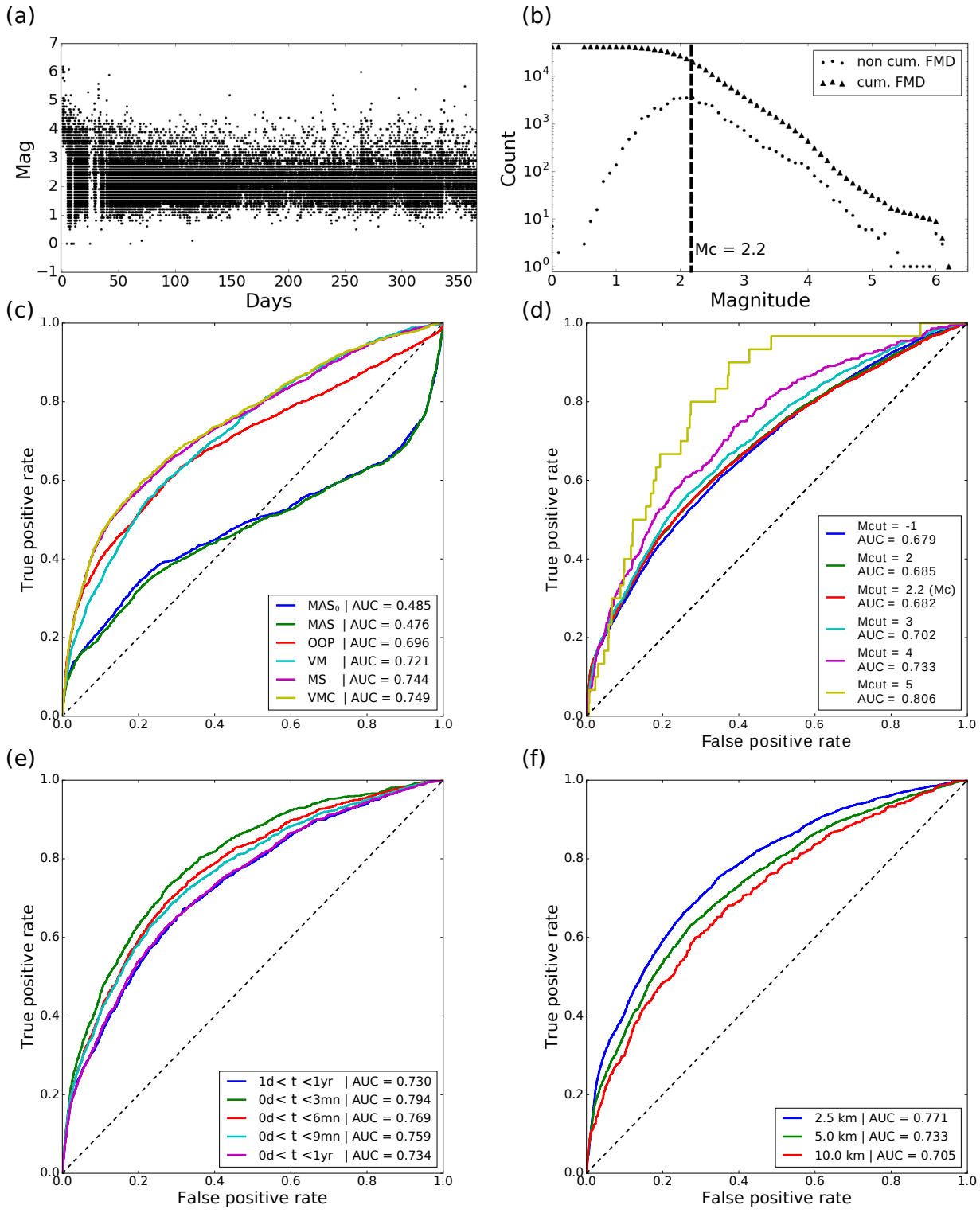

Figure 2.3: ROC analysis of 1999 Chi-Chi sequence: (a) shows the aftershocks within the first year after the mainshock; (b) cumulative and non-cumulative frequency-magnitude distribution, where the estimated completeness magnitude M_c is marked at 2.2; (c) shows the ROC curves for the different stress metrics, and (d-f) are the ROC curves for the VM stress metric with different M_{cut}, aftershock duration, and grid size, respectively.

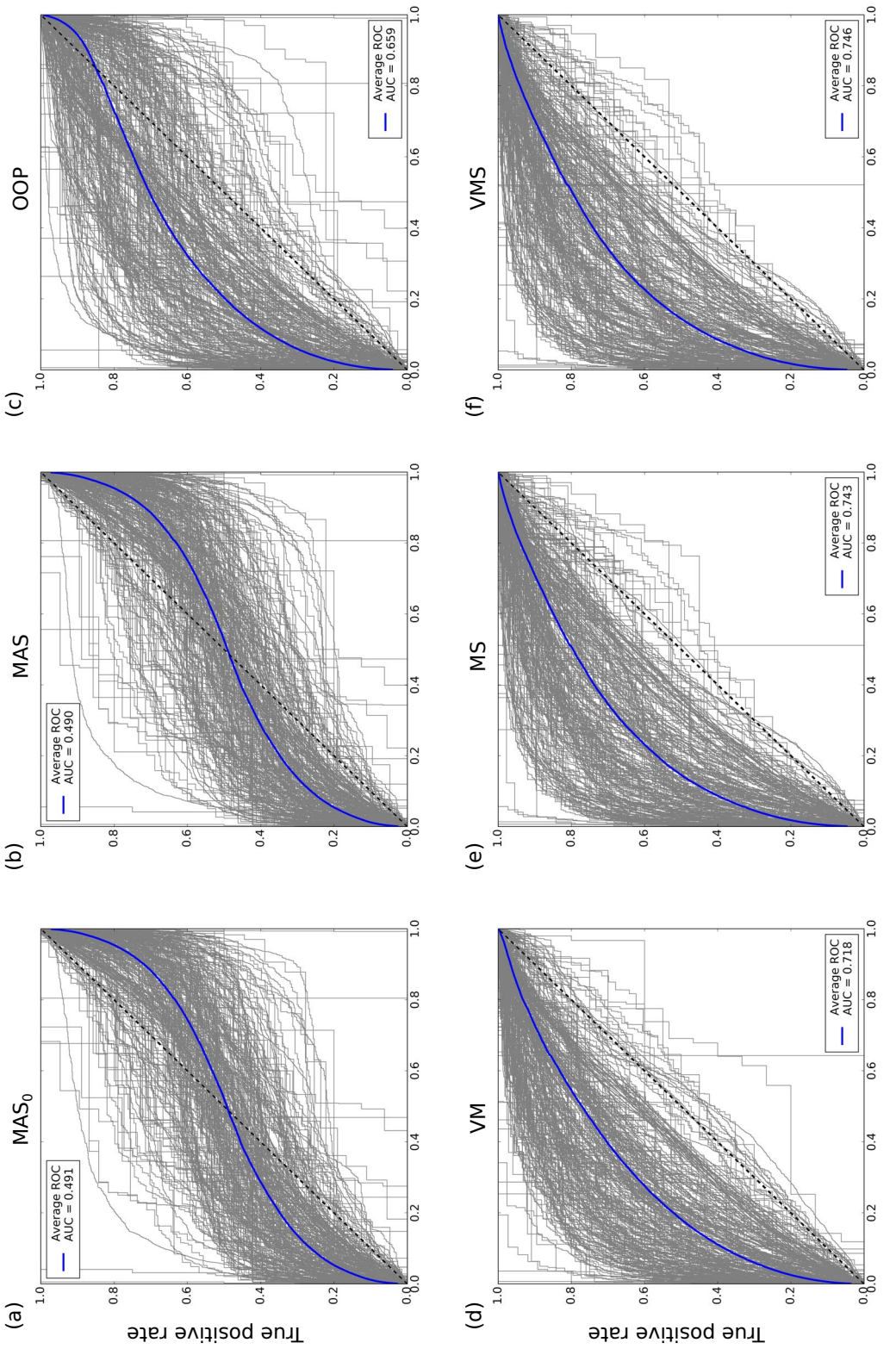

Figure 2.4: ROC analysis (a-f) for all analyzed slip distributions and stress metrics (a) MAS_0, (b) MAS, (c) OOP, (d) VM, (e) MS, and (f) VMS, where thin lines are related to the result of individual slip distributions and the thick blue line is the binned average with corresponding AUC value mentioned in the legend. A reference line is plotted as black dotted line, which refers to the result for random data.

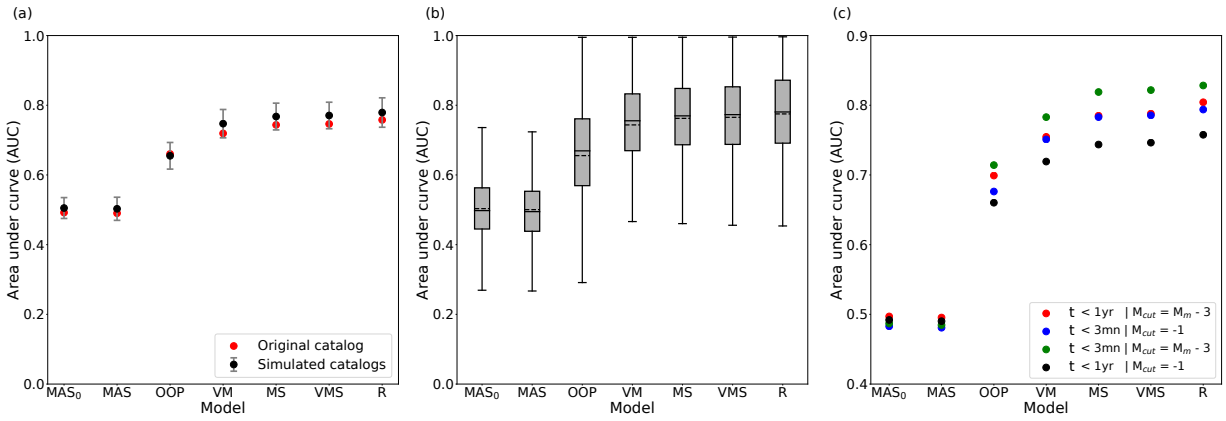

Figure 2.5: AUC results as a function of the model type: (a) mean AUC values with its uncertainties (± on standard deviation) assuming a location error of 3 km (see Sec. 2.4) (b) AUC results for all slip distributions represented as box plots. The grey part of the box shows the interquartile region (IQR) with first and third quartile as bounds. The solid and dotted horizontal lines inside the box refer to the median and mean values, and the extreme ends (whiskers) indicate the minimum and maximum of all results. (c) shows the average AUC value for the different aftershock sets mentioned in Sec. 2.4.

scalars MS and VMS (0.743 and 0.746 respectively). However, the maximum AUC value of 0.758 is obtained for the distance-slip probabilistic model (R) for which the figure is included in the supplementary information as Fig. S3. Note that the R-model was optimized on a large fraction of the data, while the stress metrics are not optimized. Thus this comparison might be biased, but the comparison of Mignan and Broccardo (2019) which was performed only on a subset of the test data showed the same tendency.

Fig. 2.5a shows the effect of location uncertainties of 3 km on the AUC values. We find the standard deviation of the resulting mean AUC values are small and the ranking remains the same. Fig. 2.5b shows a box plot to indicate the distribution of mean, median, quartiles and extremes of AUC values for all slip models and stress scalars. The metrics OOP, VM, MS and VMS, and distance-slip model (R) have their mean, median and first quartile all above the AUC threshold (0.5), while the mean and median for MAS_0 and MAS does not even cross this threshold. R performs best in terms of mean, median and quartile range, but the distribution strongly overlaps with those of VMS, MS and VM as the next best performing metrics. To test the robustness of the ranking, we repeated the calculation for different combinations of M_{cut} and the aftershock period (see Sec. 2.4). Fig. 2.5c shows the results of the test, which confirms the robustness of the ranking. However, the AUC scores systematically vary for all metrics and for the distance-slip model depending on the different settings. In particular, the best performing scenario (Fig. 2.5c green dots) is obtained for aftershocks within the first 3 months after the mainshock and $M_{cut} = M_m$ - 3.

Now, we go beyond binary testing and use a statistical test to estimate the aftershock numbers because real aftershock forecasts rely on the event density as discussed in Sec. 2.4. The result of the Log-Likelihood (LL) test is shown in Fig. 2.6. For a better comparison of LL-values for mainshock-aftershock sequences with different number of aftershocks, the resulting LL-value was divided by the number of aftershocks in each case. The results are presented by box plots (whisker diagrams), which are used to study the distribution of LL values. We observe a very similar trend as in the case of the ROC analysis. However, in this case, the distance-slip probabilistic model (R) now ranks below the ΔCFS based VM metric. Stress metrics VM perform significantly better than the conventional Coulomb stress calculations, but MS and VMS are still better. The best result in terms of number forecasts is obtained for VMS.

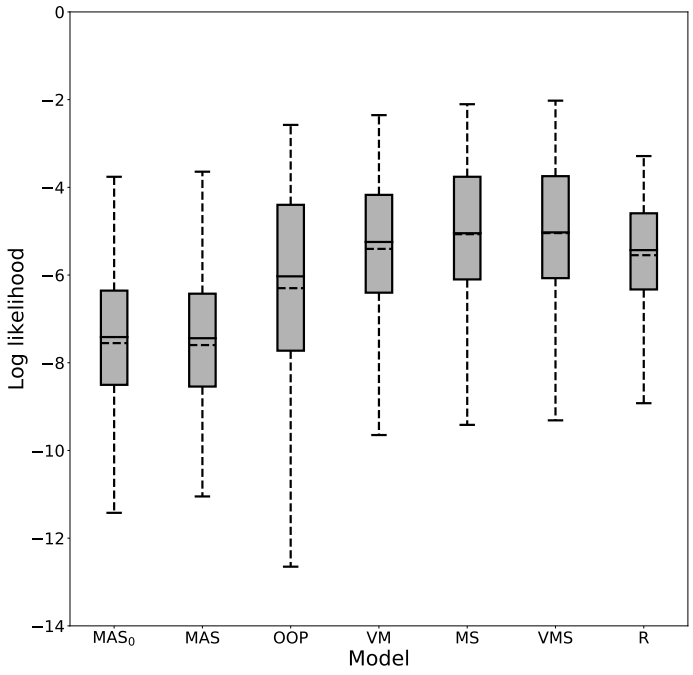

Figure 2.6: Result of the number forecast test: Box plots of the distribution of normalized LL-values for all analyzed slip models in dependence of the stress metric. The symbols are defined as in Fig. 4a.

2.6 Discussion

Coulomb failure stress has been largely used to explain earthquake triggering and particularly to describe the locations of aftershocks by separating the region into positive and negative stress change areas. Theoretically, aftershocks are only expected in regions with increased CFS value. However, it has been already recognized that aftershocks frequently occur in regions with calculated, negative stress changes, so-called stress shadows (Felzer and Brodsky, 2005; Harris and Simpson, 2002). It has been suggested that this is related to uncertainties in the slip models (Helmstetter and Shaw, 2006; Marsan, 2006; Hainzl et al., 2009) as well as the variability of the receiver mechanisms (e.g. Hainzl et al. (2010b)). Taking these uncertainties into account has been previously shown to improve the forecasts significantly (Cattania et al., 2014). A study conducted by Steacy et al. (2005b) suggests, in a poorly defined regional stress area, or in a structurally complex area, the strike of the receiver planes should be fixed to that of the mainshock plane and let the dip and rake vary to calculate the Coulomb stress.

The uncertainties and finite resolution of finite-fault models reduces the capability of Coulomb stress to reproduce the on-fault aftershocks (Steacy et al., 2004). With majority of aftershocks occurring in the proximity of the mainshock rupture plane (Moradpour et al., 2014; Felzer and Brodsky, 2006; Gu et al., 2013), the Coulomb stress metric is expected to suffer more strongly than the simple metrics from those limitations. In order to test whether this explains our results, we repeated the ROC analysis by eliminating near fault grid cells as well as their respective aftershocks (see Fig. S2). While MAS_0 and MAS do not significantly improve, the performance of the OOP metric deteriorates when excluding near fault aftershocks. While this is counterintuitive, it is likely related to the effect of background activity, which is not associated to the mainshock stress. Excluding the near-fault area also excludes the area with the highest signal-to-noise ratio.

The recent studies of Meade et al. (2017) and DeVries et al. (2018) claimed that simple

stress metrics, which do not need any specification of the receiver mechanism, are superior to the Coulomb stress calculations. However, their claim can be challenged because of the unrealistic CFS calculations, which did not account for the known uncertainties in the CFS calculations, as well as the potential artifacts and shortcomings of their ROC analysis. Thus we performed a systematic re-analysis including (i) previously introduced CFS-scalars accounting for receiver fault variability (OOP and VM), (ii) improved stress calculations based on regional, layered velocity models, (iii) different time windows and magnitude cutoffs, and (iv) the LL-test quantifying the forecasts of the spatial distribution of aftershock numbers. Countering the approach of DeVries et al. (2018), Mignan and Broccardo (2019) shows that a logistic regression model using average mainshock slip and measured distance performs better than DNN approach. Hence, we consider the distance-based model as reference model and perform a detailed analysis to compare the performance of stress metrics.

Our comprehensive analysis shows that the results of OOP and VM are significantly better than the previously tested MAS-value. This indicates the importance in accounting for the variability of aftershock mechanisms to get more realistic CFS-predictions. Further, geological constraints can be used to narrow down the standard deviation in receiver fault distribution to obtain more realistic results. While there are improvements observed in the performance of OOP and VM, scalar stress metrics still performed significantly better than receiver dependent metrics. The underlying reason is not yet clear and needs further research. It might be that MS and VMS are more efficient in accounting for triggering mechanisms which are not directly considered, such as afterslip, poro/visco-elastic deformations, and dynamic stress triggering. However, our tests show that distance-slip (R) is the best performing model for forecasting the aftershock area (binary forecast). This result indicates that there might not be any need to calculate stress tensors when forecasting the activation area. In contrast, the best stress metrics are found to outperform the R-model in regards to forecasting earthquake numbers, i.e. the spatial density of aftershocks which is more important for seismic hazard studies. It should be noted that our analysis of alternative stress metrics is not exhaustive and other metrics might be even better. For example, Terakawa et al. (2020) just introduced a new energetics-based stress metrics ΔETS, jointly accounting for coseismic stress changes and the background stress field. While their test for the case of the Landers aftershock sequence shows encouraging results, Mignan and Broccardo (2020) replied that it is likely not better than their distance-based approach. Whether or not ΔETS systematically improved forecasts might be tested in a future study similar to the present one.

For our analysis, we tried to use some meaningful parameters for the CFS-calculations. Using more realistic friction coefficients, background stresses (OOP), or uncertainties in the receiver mechanisms (VM) might improve the results of the CFS-metrics. However, such a retrospective optimization of model parameters would bias the comparison, because MS and VMS have no free parameters. Although the background stress field for the OOP model could be set according to alternate rules. For example, Mignan (2020) suggested that the pre-stress is released by the mainshock stress drop. So, we recalculate the OOP metric for deviatoric background stress which is calculated for each mainshock individually to equal the estimated stress drop (see details in the supporting information, Fig. S4). A notable improvement is observed in the OOP results, but it does not change the ranking of stress metrics and distance-slip model.

Our test results might be distorted by background events and aftershocks triggered by aftershocks, so-called secondary triggering. Our analysis already indicates that the results change for different time windows, with best results for aftershocks in the shortest time period after the mainshock. This points to the blurring effect of background activity. Declustering may possibly remove the effect of higher order aftershocks, but no simple method exists which could be applied on our diverse data set. In general, the epidemic type aftershock sequence (ETAS) model accounts systematically for background as well as secondary aftershock triggering. Im-

plementing a spatial kernel based on the stress metrics could be one way to do systematic tests including background and secondary aftershock triggering. However, those studies can only be performed for individual sequences with high data quality.

In our study, we do not consider the effect of dynamic stress changes which is used to explain aftershock locations within a week of a large mainshock (Prejean et al., 2004). However, our results indicate that the stress metrics works best for the largest aftershocks triggering in the shortest time period after the mainshock. This is encouraging, because they have the largest impact on seismic hazard. A thorough analysis can be performed like in Fig. 2.5c to specify the forecasting thresholds on the time period and cutoff magnitudes for different tectonic regions.

It is important to note that our study does not discard the use of CFS in general and Coulomb failure theory might still describe the physics for earthquake triggering. It rather indicates that CFS in the case of limited fault information is not the best choice for aftershock forecasting. However, if precise information about the receiver planes are available, CFS might still be the best choice e.g. to evaluate the trigger potential on well known neighboring fault segments.

2.7 Conclusion

Despite its frequent application for several decades, Coulomb failure stress calculations have been questioned by recent studies and shown to be outperformed by other stress scalars and state-of-the-art methods like deep neural network in forecasting aftershocks. However, the recent results are also questionable because of an artificial DNN application (Mignan and Broccardo, 2019) as well as simplified CFS calculations. As this has broad implication for this research area, we performed a comprehensive re-analysis of the previous ROC-based study. Here we include CFS-metrics accounting for the variability of aftershock mechanisms and additionally taking account of the incompleteness of catalogs as well as the occurrence of background activity into account. In addition to the previously conducted ROC-analysis for binary forecasts, we also tested forecasts of aftershock numbers.

To summarize, we find that the results of the ROC-analysis are dependent on the magnitude cutoff, aftershock duration and grid-sizes and that more realistic CFS calculations (OOP and VM) can significantly improve the results. However, our analysis verifies that the stress scalars MS and VMS, and distance-slip probabilistic model (R), all of which do not rely on any specification of receiver mechanisms, outperform on average the CFS metrics in all test setups. While CFS might still be used for the evaluation of the stress changes on well-defined fault segments, our results indicate that spatial forecasts of the aftershock density might be generally improved by using von-Mises stress (VMS) instead of Coulomb stress.

Chapter 3

A Reappraisal of the 2005 Kashmir (M_w 7.6) Earthquake and its Aftershocks: Seismotectonics of NW Himalaya

Abstract

We study the source properties of the 2005 Kashmir earthquake and its aftershocks to unravel the seismotectonics of the NW Himalayan syntaxis. The mainshock and larger aftershocks have been simultaneously relocated using phase data. We use back projection of high-frequency energy from multiple teleseismic arrays to model the spatio-temporal evolution of the mainshock rupture. Our analysis reveal a bilateral rupture, which initially propagated SE and then NW of the epicenter, with an average rupture velocity of ∼2 $km\ s^{-1}$. The area of maximum energy release is parallel to and bound by the surface rupture. Incorporating rupture propagation and velocity, we model the mainshock as a line source using P- and SH-waveform inversion. Our result confirms that the mainshock occurred on a NE dipping (∼35∘) fault plane, with centroid depth of ∼10 km. Integrated source time function show that majority of the energy was released in the first ∼20 s, and was confined above the hypocenter. From waveform inverted fault dimension and seismic moment, we argue that the mainshock had an additional ∼25 km blind rupture beyond the NW Himalayan syntaxis. Combining this with findings from previous studies, we conjecture that the blind rupture propagated NW of the syntaxis underneath a weak detachment, overlain by infra-Cambrian salt layer, and terminated in a wedge thrust. All moderate-to-large aftershocks, NW of the mainshock rupture, are concentrated at the edge of the blind rupture termination. Source modeling of these aftershocks reveal thrust mechanism with centroid depths of 2–10 km, and fault planes oriented sub-parallel to the mainshock rupture. To study the influence of mainshock rupture on aftershock occurrence, we compute Coulomb failure stress on aftershock faults. All these aftershocks lie in the positive Coulomb stress change region. This suggest that the aftershocks have been triggered by either co-seismic or post-seismic slip on the mainshock fault. [1]

- The 2005 Kashmir mainshock had a bilateral rupture (V_r ∼2 $km\ s^{-1}$) on a NE dipping thrust plane (∼35∘) with major energy released within top 10 km of the surface.
- The mainshock ruptured the surface for ∼75 km, and was blind for another ∼25 km, NW of the Himalayan syntaxis, underneath a wedge thrust.
- The aftershocks NW of the mainshock surface rupture were triggered by co-seismic or post-seismic slip on the mainshock fault.

[1] Originally published as (P2): Powali, D., **Sharma, S.**, Mandal, R., & Mitra, S. (2020). A reappraisal of the 2005 Kashmir (Mw 7.6) earthquake and its aftershocks: Seismotectonics of NW Himalaya. *Tectonophysics*, 789, 228501. https://doi.org/10.1016/j.tecto.2020.228501

Keywords –Kashmir earthquake, aftershocks, high frequency back-projection, source mechanism, Coulomb failure stress, seismo-tectonics

3.1 Introduction

The 8th October 2005 Kashmir earthquake (M_w 7.6) originated close to the junction of the Karakorum, Pamir and Hindukush ranges at the northwestern (Kashmir-Hazara) syntaxis of the Himalaya and produced a surface rupture on the Tanda and the Muzzafarabad faults (Avouac et al., 2006). This region is marked by the sharp hairpin bend of the Main Boundary Thrust (MBT), striking SE-NW in the Kashmir Himalaya, to NE-SW along the Hazara Arc (Quittmeyer and Jacob, 1979) (Fig. 3.1). The surface rupture of the 2005 event is observed to truncate at this MBT syntaxial bend. Local geological study by Wadia (1931) suggested that the syntaxis is produced by a resistant spur of the Indian shield which indents into the Himalaya and the structural features wrap around it. However, Armbruster et al. (1978) argued that a thick layer of infra-Cambrian salt (evaporite layer) associated with the detachment causes decoupling and anomalous southward translation of the shallower segment of the MBT forming the syntaxial bend. Small-to-moderate earthquakes recorded by a local seismograph network around the Tarbela Dam, close to the syntaxis, had revealed a NW-SE aligned seismicity belt, referred to as the Indus Kohistan Seismic Zone (IKSZ) (Seeber et al., 1980). The seismicity in this zone extends ∼100 km in length, ∼20–40 km in width and is confined within the top ∼25 km from the surface. The IKSZ dips to the NE and is conjectured to be an extension of the sub-surface ramp associated with the MBT. It extends beyond the syntaxial bend to the northwest and correlates with the pronounced topographic step (Armbruster et al., 1978). From the distribution of seismicity and composite fault plane solutions Seeber et al. (1980) proposed a decollement style of tectonics in the Kashmir-Hazara syntaxis, similar to the central Himalaya, with an exception of a thick layer of infra-Cambrian salt which causes the detachment to slip aseismically in patches.

The last major earthquake in the Kashmir Himalaya, before the 2005 event, occurred in 1555 (M_w ∼8.0), west of the 1905 Kangra earthquake (M_w 7.8) (Bilham et al., 2004; Khan et al., 2010). The meisoseismal zone of the 1555 earthquake lies immediately SE of the surface rupture of the 2005 earthquake and possibly extended up-to the rupture zone of the 1905 Kangra earthquake. This region has experienced a number of moderate-to-strong earthquakes, which occurred on a series of thrust faults striking parallel to the MBT and on either sides of the syntaxis (Seeber and Armbruster, 1981). Two of these are the 1974 (m_b 6.0) Patan earthquake (Jackson and Yielding, 1983) to the northwest of the syntaxis, and the 2013 (M_w 5.7) Kishtwar earthquake (Mitra et al., 2014; Paul et al., 2018) to the southeast of the Kashmir Valley (Fig. 3.1). Recent GPS observations across the Kashmir Himalaya, spanning the Zanskar Ranges, the Kashmir Valley and the Pir Panjal Ranges, reveal a range-normal convergence of 11±1 mm/yr with a dextral shear of 5±1 mm/yr (Schiffman et al., 2013). This is ∼30% lower than the arc-normal convergence across the Central Nepal Himalaya (Avouac, 2003). Modeling of the GPS velocities on a NE-dipping detachment revealed a ∼170 km wide locked decollement (Main Himalayan Thrust - MHT) beneath the Kashmir Himalaya. This is significantly wider than the ∼110 km wide locked MHT beneath the Central Himalaya (Ader et al., 2012). Comparing the GPS data with geological convergence rates (Gavillot et al., 2016), it has been argued that the observed arc normal convergence is partitioned into ∼5–6 m$m\ yr^{-1}$ convergence on the Main Frontal Thrust (MFT) and ∼6–7 m$m\ yr^{-1}$ convergence on hinterland faults, such as the Riasi Fault, SW of the Kashmir Valley. The Tanda and the Muzzafarabad faults (Avouac et al., 2006), which hosted the 2005 earthquake, is considered to be the westward extension and northward stepping of the Riasi Fault. All these faults outcrop between the MBT and the MFT, southwest of the Kashmir Valley (Fig. 3.1).

Analysis of satellite ASTER images had revealed that the 2005 earthquake occurred on a steeply NE dipping thrust fault (dip ∼30∘) with a clear surface rupture of ∼75 km, aligned with the mapped Tanda and Muzaffarabad faults. Slip modeling using teleseismic waveforms

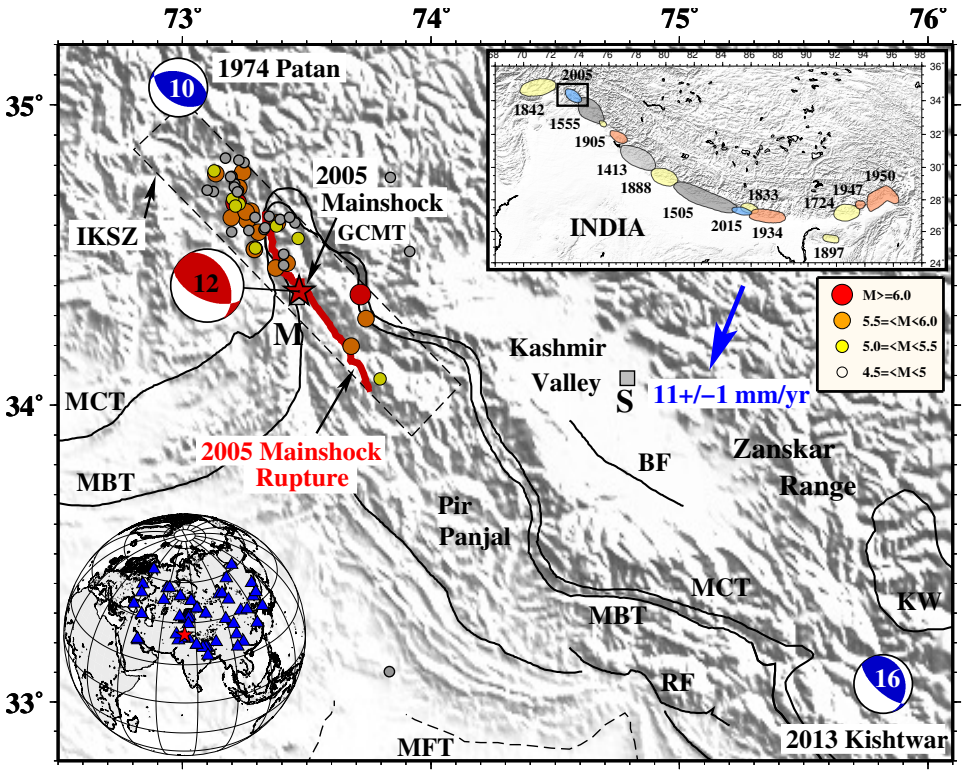

Figure 3.1: Inset top right: Topographic map of the Himalaya with the rupture patches of major earthquakes labeled by the year of occurrence. Main plot: Topographic map of Kashmir Himalaya (boxed in the inset top right) with plot of relocated epicenter of the 8 October 2005 mainshock and its aftershocks (color coded and scaled by size – see label). The stations used for the relocation are plotted in the inset bottom left. The mainshock G-CMT solution (Dziewonski et al., 1981; Ekström et al., 2012) is plotted as a red star (location) and red focal mechanism, with the centroid depth written on the mechanism. The surface rupture taken from Avouac et al. (2006) is plotted as a red line. The source mechanisms of the 1970 Patan earthquake and the 2013 Kishtwar earthquake are plotted as blue focal spheres. Structural elements: MFT – Main Frontal Thrust, MBT – Main Boundary Thrust, MCT – Main Central Thrust, RF – Riasi Fault, KW – Kishtwar Window, BF – Balpora Fault, and IKSZ – Indus Kohistan Seismic Zone are taken from Avouac et al. (2006); Gavillot et al. (2016). The arc-normal GPS shortening rate across the Kashmir Valley, taken from Schiffman et al. (2013), is plotted as a blue arrow.

had revealed a bilateral rupture with velocity of ∼2 km s^{-1}, lasting ∼25 s and average fault offset of ∼4 m (Avouac et al., 2006). Ground deformation modeling using SAR data (Pathier et al., 2006) reveal a fault line oriented NW-SE over a distance of ∼80 km and the majority of the energy released within the top 10 km from the surface. The southern segment of the fault line is almost straight between Muzaffarabad and Bagh, over a length of ∼55 km. Whereas the northern segment of the fault line between Muzaffarabad and Balakot is curved over a length of ∼25 km. Parsons et al. (2006) labels these two faults as the Balakot and Bagh faults. The hanging wall, east of the fault trace, is modeled to have the largest displacement along the northern segment which was used to explain the strongest ground shaking in Muzaffarabad and Balakot. From these studies, the surface rupture was observed to truncate at the MBT syntaxis and had been used to suggest a strong structural control on the rupture termination (Fig. 3.1). However, Bendick et al. (2007) used global positioning system observations of surface displacement and aftershock locations to propose slip on a blind rupture extending NW from Balakot and also on a flat dislocation at ∼5 km depth, forming an active wedge thrust. The mainshock was followed by a series of moderate-to-strong aftershocks, most of which lie NW of the co-seismic surface rupture.

In this study we revisit the source properties of the 2005 Kashmir mainshock and the aftershocks. Our study adds to the existing knowledge of this earthquake in the following ways. We simultaneously relocate the mainshock and the larger aftershocks using phase data to study their spatial relationship. We study the spatio-temporal evolution of the mainshock fault rupture using back-projection of teleseismic data from global arrays. We use the rupture directivity obtained from the back-projection study to model the mainshock for a propagating-line-source mechanism. We model the centroid source mechanisms of the larger aftershocks ($M_w \geq 5.0$) to obtain precise focal mechanism parameters and depth. Using this information we compute the Coulomb failure stress changes due to the mainshock rupture on the modeled aftershock fault planes. Finally, the results of our study are combined with the present understanding of the regional tectonics to obtain a seismotectonic model of the northwest Himalayan syntaxis.

3.2 Earthquake Relocation

The 2005 Kashmir mainshock and the moderate-to-strong aftershocks ($M_w \geq 4.5$) were recorded by the global network of stations. We relocated the mainshock and 49 aftershocks, which occurred within the next 12 months, using phase arrival-time information from the International Seismological Center (ISC) catalogs. The modified Joint Hypocentral Determination (JHD) method of Jordan and Sverdrup (1981) was used to perform the relocation. The P-wave arrival times from 62 local, regional and teleseismic stations, within a distance range of 1–51∘, have been used for the analysis (Fig. 3.1 inset). In order to minimize the bias from cluster of stations in a particular azimuth, we perform a station calibration. This is done by computing synthetic phase-arrival data at all stations, for a known source, through the IASP91 velocity model (Kennett and Engdahl, 1991). This process is repeated a number of times to ascertain the relative weights for the stations, which produces the best fitting relocation (minimum misfit solution) for the known source. These set of calibrated stations are then used to jointly relocate the mainshock and aftershocks. In the joint relocation algorithm, the observed arrival times at each station is weighted by the relative weight obtained from the calibration. Travel-time variance is used as an a priori information to compute the confidence ellipsoids. The location uncertainty of the aftershocks are within ±5 km. Result of the relocation show that the majority of the aftershocks are clustered NW of the mainshock rupture, with a couple at the SE end, and one close to the mainshock epicenter. The spatial distribution of the clustered aftershocks show a SE-NW trend, following the surface trace of the mainshock fault (Fig. 3.1). The epicenter of the larger aftershocks ($M_w \geq 5.0$) are distributed up-to ∼30 km NW of the mainshock surface

rupture.

3.3 Spatio-temporal evolution of the mainshock rupture

We use broadband teleseismic data from the Australian network (16 stations), European network (68 stations) and Taiwan network (28 stations) to image the spatio-temporal evolution of the 2005 Kashmir mainshock rupture, through back-projection of high-frequency P-waves (Fig. 3.2). The data was acquired from the Incorporated Research Institutions in Seismology - Data Management Center (IRIS–DMC) in the epicentral distance range of 30∘ to 90∘ (Fig. 3.2a inset). This particular epicentral distance range was chosen to avoid waveform triplication for short distances arising from the crust and upper-mantle heterogeneity; and for long distances due to interference from the core-mantle boundary.

The back-projection method utilizes the curvature of wavefronts and their time-reversal property, from dense seismic arrays, to resolve the source locations from where the energy emanated. This is done by time-shifting and stacking the seismograms on to a potential source grid located around the hypocenter (Ishii et al., 2007). The source grid points can be considered in three dimensions, but for simplicity we fixed it at the hypocentral depth to highlight only the lateral variations in the earthquake rupture process. This assumption of constant depth is logical as the depth resolution of released energy, for shallow but large earthquakes, is not well constrained from teleseismic waveforms (Kiser et al., 2011; Kiser and Ishii, 2012). Use of data from multiple arrays provide a good back-azimuthal coverage and reduces swimming artefacts that are likely to be introduced due to small aperture of a single array. Multiple arrays also enhance the lateral resolution of the solution (Kiser et al., 2011).

We used vertical component P-waveform data for the back-projection analysis and follow the methodology of Kiser and Ishii (2012). The detailed steps for data processing are adopted from Kumar et al. (2017). We filter the P-waveform data in frequency range of 0.2 Hz to 5 Hz for utilizing a broad band of frequencies. The chosen frequency range is broader than most studies. This allows first-order, low frequency evolution of the rupture process, and also highlights high-frequency spatio-temporal variations of the energy distribution during the rupture propagation. The source zone is parameterized as a horizontal plane at the hypocentral depth with 0.02∘ by 0.02∘ square grids. For each station, within an array, the teleseismic P-wave is windowed between 30 s before and 150 s after the P-wave arrival time. A station close to the center of the array is chosen as the reference station. The windowed P-waves from each station are cross-correlated with the reference station P-wave to estimate the time shift required to account for 3-D variation in the velocity structure. Each grid point on the parameterized hypocentral plane is assumed as a source point and the P-wave travel time is calculated, using the IASP91 velocity model (Kennett and Engdahl, 1991), to all stations within the array. The waveforms from each station are adjusted using the time shifts computed from cross-correlation, and stacked together. While stacking, the waveforms are weighted inversely by the density of stations within an array, and by the cross-correlation coefficient. The weighted stacked energy is back projected onto the source grid. This procedure is repeated for all potential source grids, for each array. Next we combine the information from different arrays following a weighting procedure. The stacked energy on hypocentral grids from each array are cross-correlated with a chosen reference array. We chose the Australian network as the reference array for this analysis as it contains maximum number of stations distributed in a wide aperture. The stacked waveforms from each array, for every potential source grid, are adjusted by the estimated time shift and summed by normalizing the amplitude. To remove possible high-frequency artefacts from the stacked waveform in each potential source grid, we use a moving average time-window. The choice of the time-window was done by analyzing a number of time-window lengths between 5 s and 10 s, and observing its relationship to high-frequency artefacts. Such artefacts cause random shift to the peak

energy at every time step and produces unrealistic rupture velocity variations. It is observed that the 5 s time-window optimally removed such artefacts and preserved the required details of the source time function (STF). Finally, the relative energy distribution is contoured on the parameterized hypocentral plane. At each time sample (i.e 1 s), the maximum energy release points are highlighted by circles, with radius scaled by their relative amplitude (Fig. 3.2a). The energy contour plot is truncated at ∼50% of the total energy level. A profile of relative energy, constructed parallel to the surface rupture of the mainshock and along the maximum energy points (≥80%) matches with the direction of the rupture propagation (Fig. 3.2b).

Result of the back-projection analysis show that the rupture occurred over a duration of ∼35 s. The STF has two pulses with major peaks at ∼10 s and ∼25 s (Fig. 3.2c). The rupture initiated with a sharp rise in the STF peaking at ∼10 s releasing the major energy within the first ∼20 s. The second peak is smaller and dies out within the next ∼10 s. From the maximum energy plot, it is observed that the mainshock rupture initiated close to the epicenter and propagated southeastward, along ∼141∘, in the first few seconds and broke the Muzzafarabad fault. Following this the rupture propagated northwestward, along ∼321∘ and ruptured the Tanda fault. The rupture is therefore bi-lateral with an average rupture velocity of ∼2 k$m\ s^{-1}$(Fig 3.2).

3.4 Source mechanism of the mainshock

The centroid moment tensor (CMT) solution for the 2005 Kashmir mainshock given by Global-Centroid-Moment-Tensor (G-CMT) (Dziewonski et al., 1981; Ekström et al., 2012) and the United States Geological Survey (USGS), is a thrust fault earthquake on a NE dipping plane. The fault plane from the G-CMT solution has strike of 334∘, dip of 40∘, rake of 123∘, and seismic moment of 2.94×10^{20} N-m. We use this as our starting model and compute synthetics for teleseismic waveforms in a distance range of 30∘ to 80∘. Fit to data was not satisfactory and we decided to remodel the mainshock as a centroid source using teleseismic long period waveforms. It was observed that this modeling of the mainshock as a single centroid source failed to fit the initial body waves pulse due to rupture directivity effects. We then remodeled the mainshock using a propagating line source model by using the rupture azimuth and velocity from the back-projection results.

The methodology for computation of source mechanism using long period teleseismic waveform has been described in detail in the literature (McCaffrey and Nabelek, 1987; Berberian et al., 1999; Paul et al., 2015; Kumar et al., 2017). We model the source mechanism of mainshock as propagating line source. For this purpose we used broadband teleseismic data from Global Digital Seismic Network (GDSN) stations which are acquired from IRIS-DMC. We use waveform data from 47 GDSN stations distributed in an epicentral distance range of 30∘ to 80∘. The teleseismic waveform data are deconvolved with instrument response and then reconvolved with a filter to reproduce the 15-100 s response of the WWSSN long-period instruments. Using the back-azimuth angles, the horizontal components of the 3-component waveforms are rotated to produce radial and transverse components. P- and SH-waveforms are then windowed with a window length of 40 s duration on the vertical and tangential components, respectively. The window length is chosen based on STF from the back-projection study. The windowed waveforms are modeled using the moment tensor inversion routine by McCaffrey and Nabelek (1987). The algorithm gives the strike and dip of the best fitting nodal plane(s), rake of the slip vector(s), the depth of the centroid source and variation of the moment released with time (STF). The time integral of STF gives the seismic moment. By minimizing the least squares misfit, iteratively between the observed and synthetic P- and SH-waveforms the final solution is obtained. For a given double couple source within a simplified Earth structure the synthetic waveform is calculated by convolving STF with the computed Green's functions for direct ar-

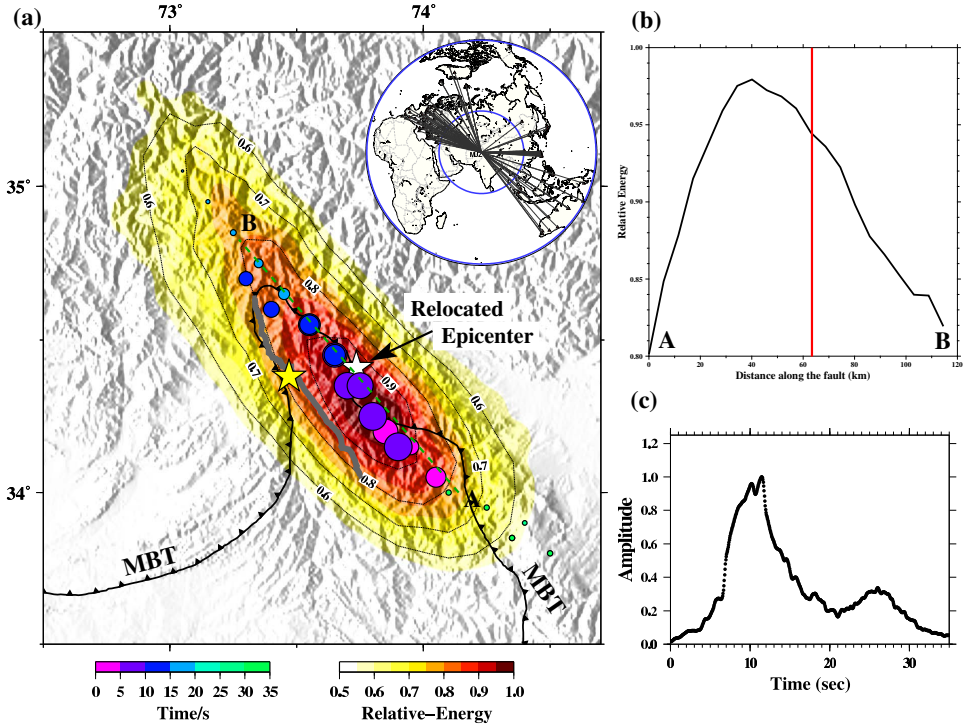

Figure 3.2: (a) Plot of P-wave high-frequency (0.2–5.0 Hz) back-projection result for the 2005 Kashmir mainshock, using global data from stations plotted in the inset map. Relative energy released from the mainshock is contoured and color coded to highlight the ruptured area on the fault. Relocated epicenter and G-CMT centroid location of the mainshock are plotted as white and yellow stars, respectively. Points of maximum amplitude released during faulting are marked by circles scaled by size, denoting relative amplitudes, and color coded by time delay following the initiation of the rupture. The rupture propagated linearly, first to the SE and then NW, parallel to the surface rupture (plotted as a grey line). The points of maximum energy released ($\geq$80%) surrounds the relocated epicenter and matches well with the maximum energy contours. (b) Profile A–B showing the relative energy released ($\geq$80%) as a function of distance along the rupture direction. The red line marks the position of the epicenter. (c) The amplitude normalized STF computed from the stack of all vertical component seismograms.

rivals (P or S), for near source reflections (pP, sP or sS) and for all the multiples. The shape and amplitude of the waveforms are related to the source parameters non-linearly, so these parameters are perturbed iteratively to minimize the misfit. From broad-band record according to the P-wave arrival time, the observed and synthetic waveforms are aligned. The SH-waveform has twice as large amplitude compared to the P-waveform. Therefore the SH-waveform are weighted half of the P-waveform. To remove the bias from cluster of stations along a particular azimuth, the observed seismograms are azimuthally weighted. For the inversion the G-CMT solution has been used as the starting model. The source parameters are best fitted by minimizing the misfit in both the amplitude and shape, between the observed and synthetic waveforms.

The rupture directivity has a significant effect on both the shape and amplitude of the waveforms as a function of station azimuth. From the back-projection study we use the rupture velocity (V_r) of 2 km s^{-1} for the propagating line source model of the mainshock. The rupture velocity is computed by dividing the along strike length of the fault by the total duration of faulting (∼35 s), estimated from STF. The rupture azimuth is chosen from the propagation direction of high amplitude pulses. As the rupture is bi-lateral, we did our waveform fitting for both azimuths of ∼141∘ and 321∘. We observe that the waveform fit is slightly better for the ∼141 ∘ azimuth. We use a ten elements STF with half-widths of 4 s each. The fault plane solution for the propagating line source model has strike of 339∘, dip of 35∘, rake of 130∘, and seismic moment of 2.844×10^{20} N-m (Fig. 3.3). Our line source solution is similar to the G-CMT solution except for the fault plane having a ∼5∘ gentler dip and the seismic moment being 3% smaller. We compared our line source solution to a point source solution, G-CMT solution and finite fault solution (Avouac et al., 2006), by comparing the fit between the synthetic and observed waveforms at a number of key stations (Fig. 3.4). We observed that the fit for the line source model is significantly better than the other solutions, mainly for the SH-waveforms.

The uncertainties and trade-offs between the modeled parameters are obtained by number of tests (Fig. 3.5). We estimate the uncertainty in depth of the main-shock line source solution by fixing the depth of the earthquake to values bracketing the best-fitting solution and reinvert the waveform data for the other focal parameters. This reveals possible trade-off between depth and other parameters in the focal mechanism and also allows us to estimate the uncertainty associated with the parameter. We follow the same procedure to estimate the uncertainty in strike, dip and rake of the best-fitting solution (Fig. 3.5). For all tests we use 1-σ bound as the uncertainty of modeled parameter. The 1-σ bound for the depth sensitivity test is estimated to be ±3 km of it's best fitting value, and the obtained solution does not trade-off with depth. For all other parameter we list the best fitting values and its uncertainties in Table 3.1.

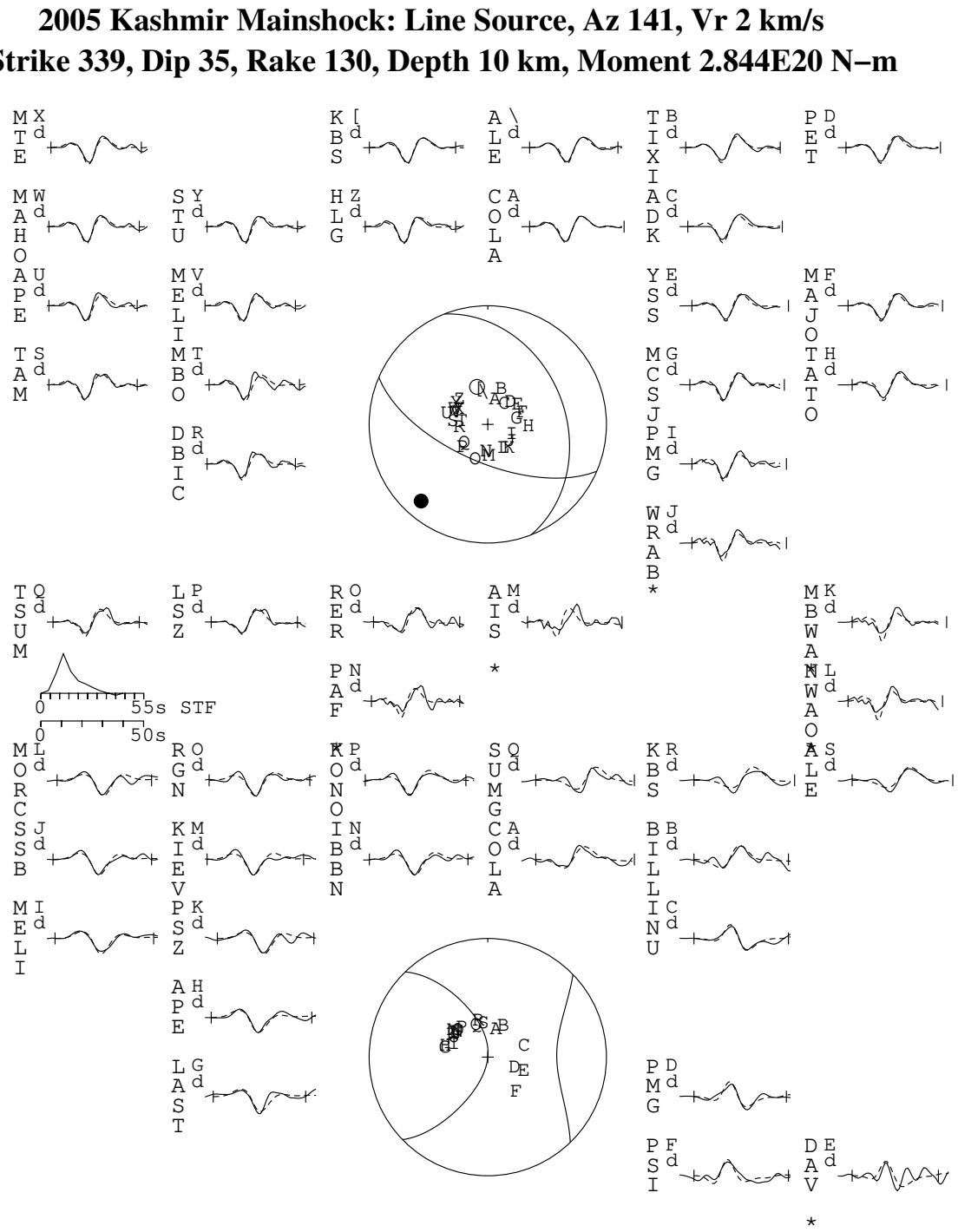

Figure 3.3: P (top) and SH (bottom) focal mechanism and waveforms (observed – bold, synthetic – dashed) for our minimum-misfit solution of the 2005 Kashmir mainshock, calculated for a line source propagating along azimuth 141◦ with a velocity of 2 k$m\ s^{-1}$. Source parameters for the best fitting solution are written on top. The station code for each waveform is accompanied by a letter corresponding to its position in the focal sphere. The time-window used for the inversion is marked by vertical lines on each waveform. The pressure and tension axes are plotted as solid and open circles on the P-wave focal sphere. The STF is plotted as triangular elements.

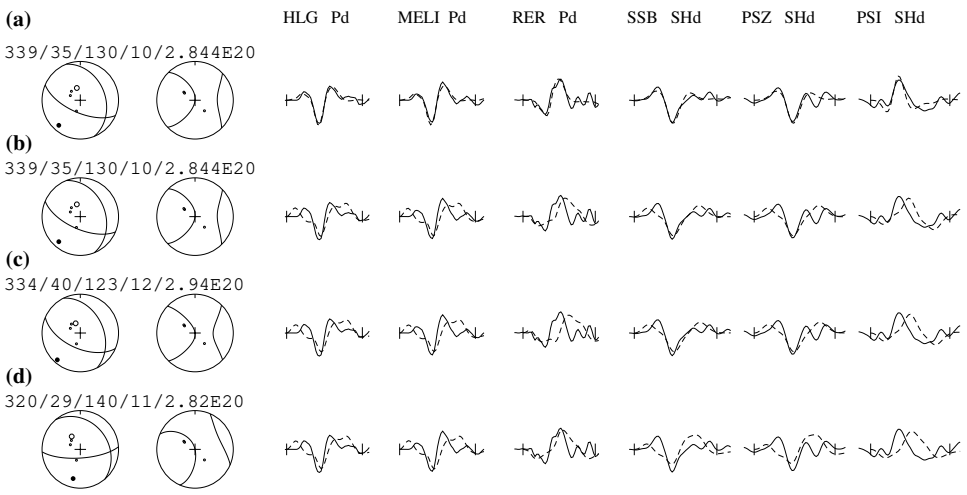

Figure 3.4: Sensitivity analysis for the 2005 Kashmir mainshock done with three seismograms each for the P- and SH-waveforms. (a) Minimum misfit solution for the propagating line source plotted in Fig. 3.3, (b) point source solution, (c) G-CMT solution and (d) finite fault solution of Avouac et al. (2006). Observe the poorer match for the first pulse and the depth phase for models in (b), (c) and (d), compared to (a).

3.5 Source mechanism of the aftershocks

Within a fortnight of the mainshock, a number of strong-to-moderate aftershocks occurred NW of the mainshock rupture within the IKSZ and one close to the hypocenter of the mainshock (Fig. 3.1 and Table 3.1). We model the source mechanism of seven of these aftershocks as point (centroid) source using the moment tensor inversion algorithm described in section 3.4 (Fig. 3.6). Source parameters of the aftershocks are described in time sequence of their occurrence following the mainshock. On the same day as the mainshock a couple of aftershocks ($M_w \geq 5.0$) occurred on the NW edge of the mainshock rupture. Of these, the first one was the largest aftershock (M_w 6.5) and had a centroid depth of ∼5 km (labeled b in Fig. 3.6a and Table 3.1). The source mechanism is a thrust fault with fault orientation and dip similar to the mainshock. The second aftershock on the day was M_w 5.7 and had a centroid depth of ∼10 km (labeled c in Fig. 3.6a and Table 3.1). The thrust fault occurred on a plane steeper (dip ∼44∘) than both the mainshock and the largest aftershock. Two aftershocks occurred on the next day, of which the first originated close to the centroid of the largest aftershock, but occurred on a steeper thrust fault (dip ∼46∘) (labeled d in Fig. 3.6a and Table 3.1). The second aftershock (M_w 5.7) on this day is the most interesting, as it occurred very close to the hypocenter of the mainshock and had a thrust fault mechanism (labeled e in Fig. 3.6a and Table 3.1). The NE dipping plane has a dip of ∼61∘, much steeper than the mainshock or any of the aftershock fault plane. If we consider this to be the fault plane, this could be explained by the presence of structural heterogeneity on the mainshock rupture plane (e.g. an undulating surface), which would accumulate residual stresses during the mainshock faulting and would lead to an aftershock on steeper dipping plane. Alternatively, if we consider the SW dipping plane as the fault plane, it can be conjectured to be a back-thrust to the mainshock with a dip of 29∘ to the SW (Fig. 3.6c). The centroid depth of this aftershock is ∼6 km and matches with the region where the mainshock slip was minimum, increasing up dip (Avouac et al., 2006). The slip increase from the centroid depth of the mainshock (∼4 m) to the surface (∼7 m) would leave a slip void at depth, which could be compensated by slip on the back thrust. We discuss further our choice of the fault plane for this aftershock following the Coulomb failure stress computation (Section 3.6). The other three aftershocks which occurred in the next couple of weeks were all located close to the NW edge of the mainshock rupture and had centroid depths between ∼2–6 km (labeled f-h in Fig. 3.6a and Table 3.1). All these were on thrust faults similar to the mainshock and largest aftershock

mechanisms.

3.6 Coulomb Failure Stress

We model the change in state of stress due to the mainshock rupture in the aftershock source zone to ascertain the triggering effects of the mainshock rupture. Mohr-Coulomb failure criterion states that, failure on a fault occurs when shear stress exceeds the frictional strength. The frictional strength is linearly related to the normal stress, hence failure on a fault can occur if shear stress increases or normal stress decreases. Coulomb stress changes are defined as:

$$\Delta CFS = \Delta\tau - \mu\Delta\sigma_{ef} \tag{3.1}$$

Where τ is the shear stress, μ is the coefficient of friction, and $\sigma_{ef} = \sigma - p$ is the effective normal stress, with σ loading stress and p the pore pressure. The shear and normal stresses are calculated by resolving the stress tensor on a given fault plane, hence geometry of a receiver plane is crucial to calculate the coulomb failure stress (CFS). Coulomb failure criterion states that an earthquake can be triggered where CFS > 0.

In order to calculate the CFS, receiver fault orientation must be known. This can be done in two ways: (1) either on fixed receiver fault orientations which requires prior knowledge of the geology of the region or the exact orientation of the aftershock fault plane, or (2) on optimally oriented planes (OOP) where it is assumed that faults exist with all orientations but the faults with maximum coulomb stress change are more prone to failure. In this study we used the approach suggested by Hainzl et al. (2010b), where the orientation of the receiver faults is described by a distribution function. Instead of choosing a single value of strike, dip and rake at a point, a uniform distribution $f(strike, dip, rake) = f_1(strike).f_2(dip).f_3(rake)$ is used. This method helps in getting rid of so-called stress shadows (Felzer and Brodsky, 2005; Harris and Simpson, 2002) by calculating average ΔCFS value on receiver faults with positive stress changes. After calculating ΔCFS for the distribution of planes, the mean ΔCFS gives the final Coulomb stress change at a point. The mean value for the strike, dip and rake distribution is taken from the particular aftershock moment tensor solution computed in section 3.5. The ΔCFS has been calculated for this distribution.

ID	Event Date (dd-mn-yy)	Origin Time (hr:mm:ss)	Lat (◦ N)	Long (◦ E)	M_w	Misfit (R/D%)	Depth (km)	Strike (◦)	Dip (◦)	Rake (◦)	Reference (TWI)
Mainshock											
a.	08-10-05	03:50:35	34.370	73.717	7.6	18.1	10±3	339±5	35±5	130±5	LS
Aftershocks											
b.	08-10-05	10:46:28	34.675	73.216	6.5	40.3	5±3	325±5	34±5	95±4	CS
c.	08-10-05	21:13:31	34.647	73.276	5.7	27.1	10±3	344±5	44±5	82±4	CS
d.	09-10-05	08:30:00	34.617	73.260	5.5	45.5	5±3	323±5	46±5	100±6	CS
e.	09-10-05	19:20:36	34.290	73.738	5.7	55.2	6±3	282±6	61±5	83±5	CS
f.	12-10-05	20:23:37	34.777	73.242	5.5	31.5	6±3	311±5	51±4	79±4	CS
g.	19-10-05	02:33:28	34.772	73.135	5.6	35.1	5±3	318±6	20±5	108±5	CS
h.	23-10-05	15:04:20	34.781	73.128	5.2	56.4	2±3	298±5	25±4	76±6	CS

Table 3.1: Event date, origin time, location, magnitude, misfit and best fitting focal mechanism parameters (depth, strike, dip and rake) with associated uncertainties. The misfit is given as percent of the weighted residual variance to the weighted data variance (R/D%). The ±1-σ uncertainty for the modeled parameters are listed along-with. TWI – Teleseismic waveform inversion, LS – Line Source, CS – Centroid Source. The corresponding focal mechanisms are plotted in figure 3.6.

We use the PSCMP+PSGRN code of Wang et al. (2006) to calculate co-seismic stress for the layered velocity and density structure. The slip model for the 2005 Kashmir mainshock rupture is taken from Shao and Ji (2005). We modeled for the seven aftershocks for which we have obtained the source mechanism. The six aftershocks which are located to the NW of the mainshock rupture, we consider the NE dipping plane to the fault plane and use its orientation for the CFS computation (Fig. 3.7) However, for the aftershock which lies close to

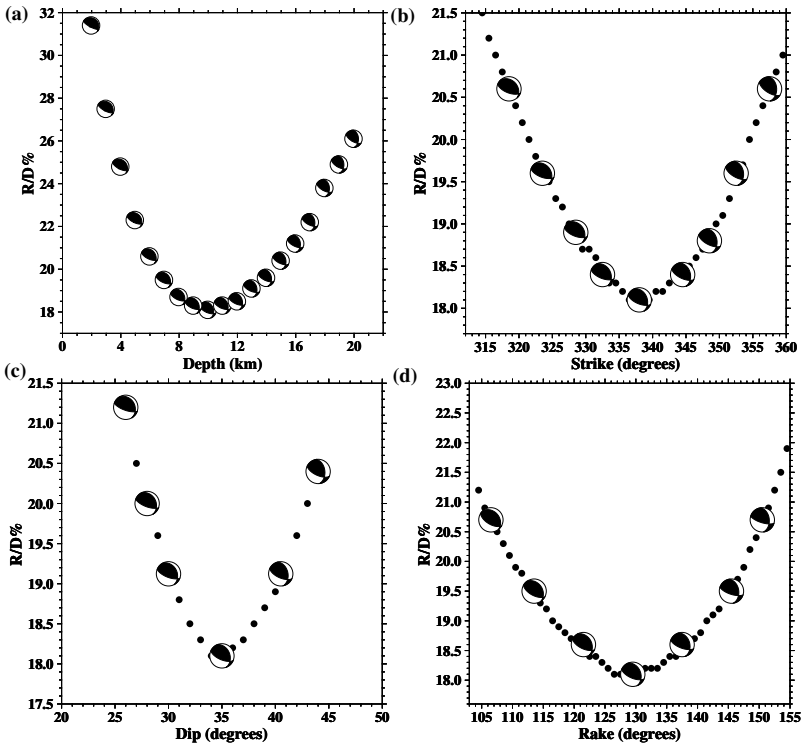

Figure 3.5: Uncertainty analysis for the focal mechanism parameters of the 2005 Kashmir mainshock line source solution: (a) depth; (b) strike; (c) dip; and (d) rake. To estimate the uncertainty, each parameter is fixed at values surrounding the minimum misfit solution (plotted on the x-axis) and all other parameters are allowed to vary freely in the inversion. Misfit value is shown as the percent of weighted residual variance to the weighted data variance (R/D%) on the y-axis. To demonstrate the trade-off between focal mechanism with the modeled parameters, focal mechanism for selected parameter values are overlay plotted on the misfit curves.

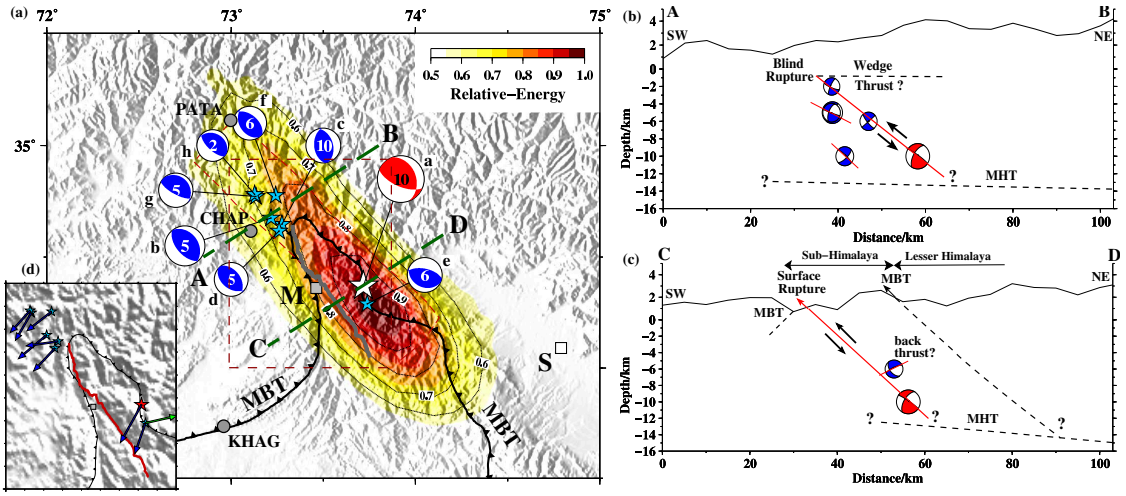

Figure 3.6: (a) Map of the 2005 Kashmir earthquake surface rupture with overlay plot of mainshock back-projection energy and focal mechanisms for the mainshock (red) and larger aftershocks (blue), modeled in this study. The focal mechanisms are plotted at the relocated epicenters and are labeled a to h as listed in Table 3.1. The modeled centroid depths are written within the focal sphere. The GPS points of PATA, CHAP and KHAG taken from Bendick et al. (2007) are plotted as grey circles. Plot of profiles (b) A–B and (c) C–D across Kashmir Himalaya (marked on (a)) with overlay plot of focal mechanisms within ±20 km projected onto the profile. The fault plane for the aftershocks are marked by the red line on the focal sphere. Profile A–B is chosen north of the surface rupture of the mainshock, through the region of the aftershocks and profile C–D is chosen through the epicenter of mainshock. The geometry of the MBT and its location have been taken from Gavillot et al. (2016) and projected onto the profile. (d) Plot of slip vector for the preferred fault plane (black arrow) and the back-thrust (green arrow).

the hypocenter of the mainshock we do this calculation for both planes (Fig. 3.8). The CFS change calculation shows the stress-increased region (i.e. positive CFS) are along the mainshock rupture surface exposure and in the area perpendicular to the rupture plane. Whereas parallel to the surface rupture, slightly away from the edge are regions of stress-depletion (i.e. negative CFS). All the aftershocks to the NW of the mainshock, lie in regions of positive CFS change. These aftershock faults may have been brought closer to failure by either the co-seismic or post-seismic slip of the mainshock. However, the aftershock near the mainshock hypocenter lies in the negative CFS change region and is possibly driven by residual stresses.

3.7 Discussion

In order to understand the seismotectonics of the NW Himalayan syntaxis, we discuss our results of the earthquake source properties in context of the regional tectonics. The majority of moderate-to-large aftershocks are concentrated in the NW, where the mainshock rupture terminated. These aftershocks lie in the depth range of the mainshock rupture (within the top ∼10 km) and is is the zone of positive CFS change. Therefore, these aftershocks could have been stress-triggered following the mainshock rupture. It is most likely that these aftershocks occurred on the NE dipping thrust planes, similar to the mainshock (Fig. 3.6a). The slip vectors, computed for these NE dipping planes are consistent with the mainshock slip vector (Fig. 3.6d) and are sub-parallel to the GPS convergence vector (Fig. 3.1). These confirm that the Himalaya slipped over the Indian sub-continent in the SW direction. The cluster of farthest aftershocks is ∼30 km NW of the mainshock rupture, which is much larger than the uncertainty of the relocated hypocenters. To explain this, we consider the fault model proposed by Bendick et al. (2007), of an active blind wedge thrust north of the surface rupture. We use the seismic waveform inverted mainshock centroid depth of ∼10 km and fault dip of ∼35∘, to estimate the fault width of ∼18 km. Given an average slip of ∼4 m (Avouac et al., 2006), crustal μ of $4 \times 10^{10}\ Nm^{-2}$, and waveform inverted seismic moment of 2.844×10^{20} N m, we compute the fault length to be ∼100 km.

This is ∼25 km longer than the observed surface rupture of ∼75 km (Avouac et al., 2006). This argument is supported by the significantly lower seismic moment computed from geodetic observations, as compared to the seismic waveform inversion. We conjecture that the mainshock faulting either extended as a blind thrust or caused post-seismic slip at least by ∼25 km, NW of the Tanda fault (Fig. 3.6b). However, it is evident that the surface rupture stops at the syntaxial bend of the MBT (Fig. 3.1). The plausible explanation for the rupture to continue subsurface comes from the presence of a flat detachment at ∼5 km overlain by a thick layer of infra-Cambrian salt north and west of the MBT syntaxis (Seeber et al., 1980). Seeber and Armbruster (1981) proposed that the presence of this weak detachment, west of the Kashmir Himalaya, superficially translates the thrust system southward to form the NW Himalayan syntaxis. But the NE dipping micro-seismicity extends northwestward beyond the syntaxis and is concentrated on the IKSZ (Armbruster et al., 1978; Seeber et al., 1980). The fault plane solutions of the 2005 Kashmir earthquake and its aftershocks, along with the NE dipping micro-seismicity (Armbruster et al., 1978) suggest that the blind rupture extended along the IKSZ, a ramp thrust which splays from the basal detachment (MHT) and has the same geometry as the Tanda fault (Fig. 3.6). It is noteworthy that the 1974 Patan earthquake (m_b 6.0) occurred on the northwest edge of the IKSZ, at a depth of ∼10 km, and had similar thrust fault mechanism as the 2005 Kashmir earthquake and its aftershocks (Fig. 3.1). This active wedge thrust model (Fig. 3.9) dominates the seismotectonics of the NW Himalayan syntaxis.

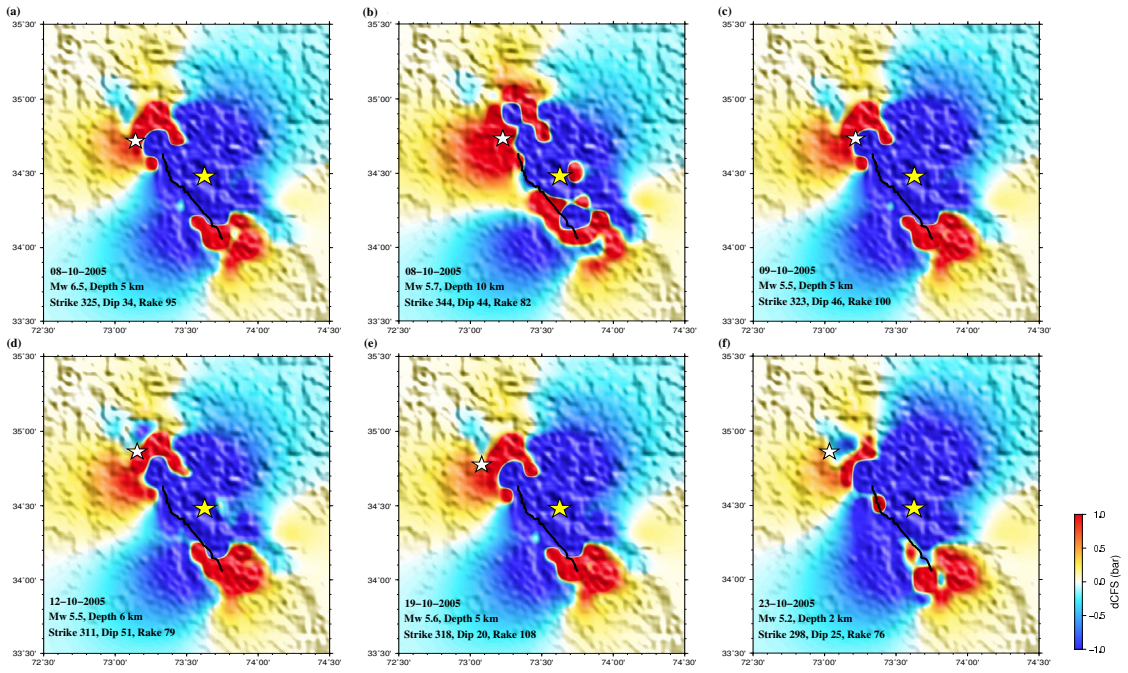

Figure 3.7: (a) to (f) Coulomb failure stress plot for the aftershocks on the NW edge of the mainshock rupture. Red and blue regions mark heightened and lowered stress, respectively, due to the mainshock rupture. The relocated epicenter of the mainshock and the aftershock are plotted as yellow and white stars, respectively. The details of the aftershock are given at the lower left corner of each plot and tabulated in Table 3.1.

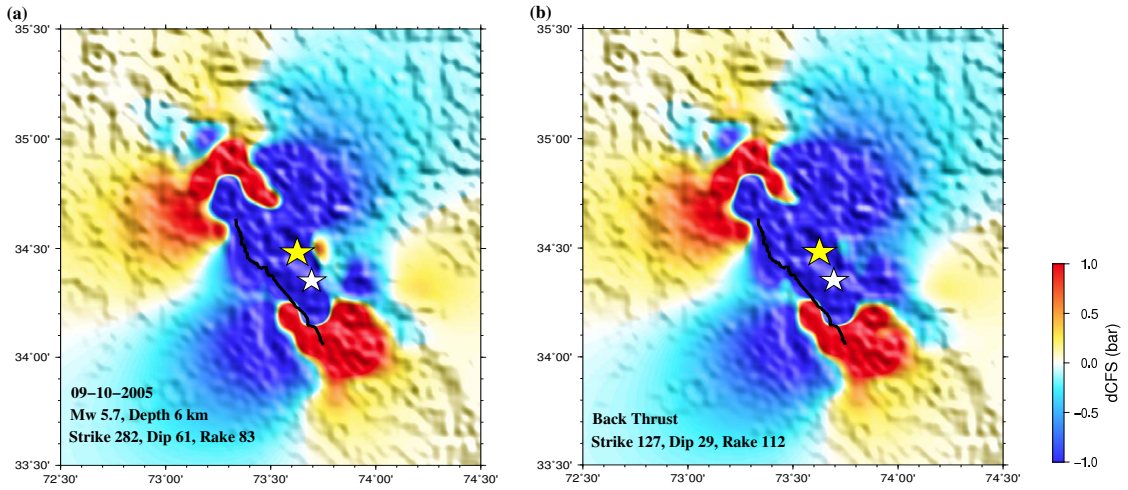

Figure 3.8: Coulomb failure stress plot for the aftershock close to the hypocenter of the mainshock (e in Table 3.1). Computation has been done (a) for the NE dipping plane, and (b) for the SW dipping back-thrust. However, both planes show that the epicenter lies in negative CFS zone. Color scale and symbols are same as figure 3.7.

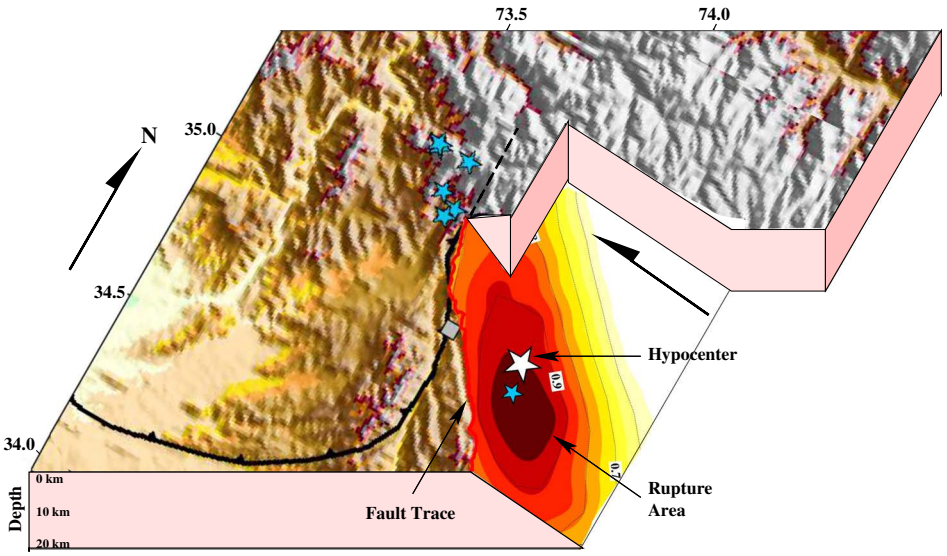

Figure 3.9: Schematic diagram of the 2005 Kashmir earthquake with back projected energy plotted on the 3-D disposition of the mainshock fault plane. The fault plane is truncated at the surface rupture shown as a red line. The rupture is blind beyond the NW Himalayan syntaxis. The mainshock and aftershocks modeled in this study are plotted as white and blue stars, respectively. The city of Muzzafarabad is plotted as grey square.

3.8 Conclusions

We study the source properties of the 2005 Kashmir earthquake and its aftershocks to unravel the seismotectonics of the NW Himalayan syntaxis. Back projection of high-frequency energy from multiple teleseismic arrays, as a function of time, has been used to study the spatio-temporal evolution of the rupture process and to estimate the average rupture velocity and azimuth. We incorporate this information to model the mainshock source mechanism as a propagating line source, using P- and SH-waveform data from GDSN stations. We also modeled the centroid source mechanism of seven large-to-moderate aftershocks which occurred within the next fortnight of the mainshock. The mainshock focal mechanism has been used to compute the Coulomb failure stress on the aftershock fault planes, to understand the aftershocks triggering effect due to the mainshock. The main conclusions of this study are as follows:

- The 2005 Kashmir (M_w 7.6) earthquake occurred on the Muzzafarabad-Tanda fault (also known as the Balakot-Bagh fault), an active thrust fault SW of the MBT syntaxis, and the northernmost of the en-echelon faults south of the Kashmir Valley. The mainshock had a bilateral rupture, which initially propagated SE from the epceinter and then to the NW, with average rupture velocity of $\sim$2 $km\ s^{-1}$.

- Modeling the mainshock mechanism as a propagating line source along 141$\circ$ reveal an oblique thrust fault on a NE dipping plane of $\sim$35$\circ$, with a centroid depth of $\sim$10 km. The STF from the back-projection and focal mechanism modeling show that the earthquake ruptured over $\sim$35 s and majority of the energy was released in the first $\sim$20 s, close to the surface, within top $\sim$10 km.

- From source mechanism and seismic moment we compute that the mainshock ruptured over a length of $\sim$100 km, requiring a $\sim$25 km blind thrust NW of the $\sim$75 km surface rupture. This is supported by differences in seismic moment from geodetic observations and waveform inversion. A wedge thrust model is suggested to explain the termination of the mainshock fault, underneath a weak detachment due to overlying infra-Cambrian salt layer. The moderate-to-large aftershocks, NW of the mainshock, are concentrated at the edge of the rupture termination as a blind thrust.

- Aftershocks at the NW edge of the mainshock rupture, have similar thrust mechanism as the mainshock fault. We conjecture these to have occurred on the IKSZ, which is a northwestward extension of the mainshock fault and is a NE dipping splay of the MHT. The 1974 Patan earthquake, which had a similar mechanism as the 2005 Kashmir mainshock and the aftershocks, possibly occurred at the northern edge of the IKSZ.
- One aftershock (M_w 5.7) within 48 hours of the mainshock occurred close to the mainshock hypocenter. This aftershock had a thrust fault mechanism similar to the mainshock, but the NE dipping (in the direction of the mainshock rupture plane) had a much steeper dip angle of $\sim$61$\circ$. We therefore conjecture that this event could have either been driven by residual stresses on a mainshock fault heterogeneity or could have occurred on a SW dipping back-thrust.
- Coulomb failure stress computation shows that the moderate-to-large aftershocks, NW of the mainshock rupture, occurred in the positive CFS region. This suggests that the aftershocks were triggered by either co-seismic or post-seismic slip on the mainshock fault.

Chapter 4

Seismicity parameters dependence on mainshock-induced co-seismic stress

Abstract

The Gutenberg-Richter (GR) and the Omori-Utsu (OU) law describe the earthquakes' energy release and temporal clustering and are thus of great importance for seismic hazard assessment. Motivated by experimental results, which indicate stress-dependent parameters, we consider a combined global dataset of 127 mainshock-aftershock sequences and perform a systematic study of the relationship between mainshock-induced stress changes and associated seismicity patterns. For this purpose, we calculate space-dependent Coulomb Stress (ΔCFS) and alternative receiver-independent stress metrics in the surrounding of the mainshocks. Our results indicate a clear positive correlation between the GR b-value and the induced stress, contrasting expectations from laboratory experiments and suggesting a crucial role of structural heterogeneity and strength variations. Furthermore, we demonstrate that the aftershock productivity increases nonlinearly with stress, while the OU parameters c and p systematically decrease for increasing stress changes. Our partly unexpected findings can have an important impact on future estimations of the aftershock hazard. [1]

- Statistical seismology,
- Earthquake interaction, forecasting, and prediction,
- Earthquake hazards,
- b-value

[1] Originally published as (P2): **Sharma, S.**, Hainzl, S., & Zöeller, G. (2023). Seismicity parameters dependence on mainshock-induced co-seismic stress. *Geophysical Journal International*, 235(1), 509-517. https://doi.org/10.1093/gji/ggad201

4.1 Introduction

Statistical seismology relies on two fundamental relations to explain the earthquakes' frequency-magnitude distribution and the temporal decay of aftershock occurrence: the Gutenberg-Richter (GR) and the Omori-Utsu (OU) law. The number N of earthquakes with a magnitude larger or equal to M is given by

$$\log_{10} N = a - bM \tag{4.1}$$

according to the GR-law (Gutenberg and Richter, 1944). Here, a and b are constants, with the b-value describing the relative frequency of smaller to larger events. The Omori-Utsu law describes the temporal decay of the aftershock rate, λ, after a mainshock,

$$\lambda(t) = K/(t+c)^p \ . \tag{4.2}$$

The constants K and c refer to the productivity and delay time of the power-law onset, while the exponent p is related to the rate of the aftershock decay (Utsu et al., 1995).

Due to its importance in seismic hazard assessment, many studies have focused on parameter variations of the GR and OU laws in space and time. For example, Cao and Gao (2002) observed temporal variations of the b-value beneath the NE Japan island arc, and Ogata et al. (1991) found a depth dependence of the b-value in the Kanto area of Japan. A comparative study of different aftershock sequences by Wiemer and Katsumata (1999) shows variation in b and p value ranging from 0.6 to 1.4 and 0.6 to 1.8, respectively.

Several other studies focused on the dependence of the GR and OU parameters on the mainshock magnitude and source mechanism. Hainzl and Marsan (2008) observed a significant increase in p with mainshock magnitude, while a common variation of the b and c values with source mechanism was documented by Schorlemmer et al. (2005) and Narteau et al. (2009), with the smallest b and c values for thrust events, and intermediate and largest values for strike-slip and normal mainshocks, respectively. The other OU-parameters also vary on average with the mainshock source mechanism (Tahir and Grasso, 2015).

Laboratory experiments can partly explain these observations. The b-values of acoustic emissions during rock fracturing decrease with increased differential stress (Scholz, 1968), suggesting that b may serve as a stress-sensor and predictor of mainshocks in nature (Scholz, 2015; Gulia and Wiemer, 2019). Furthermore, the laboratory-derived rate- and state-dependent friction law predicts a faster power-law onset, i.e., smaller c-value, for higher stress changes (Dieterich, 1994).

However, a systematic and detailed study of mainshock-induced stress changes and seismicity patterns has not yet been performed. Nowadays, detailed slip distributions of more than 100 mainshocks are accessible, allowing the calculation of static stress changes in the surrounding crust. In this study, we analyze the GR and OU parameters as a function of the induced stress change and rupture distance for the combined data set of 127 mainshock-aftershock sequences. In doing so, we not only adhere to calculations of Coulomb Failure Stress changes (ΔCFS) with alternative definitions of receiver mechanisms, but we also compute receiver-independent stress metrics, recently shown to be superior in forecasting spatial aftershock distributions (Meade et al., 2017; Sharma et al., 2020). Our results show systematic stress- and distance-dependent variations of the GR and OU parameters that can be useful for aftershock hazard estimations.

4.2 Data and methods

We use the reviewed International Seismological Center (ISC) catalog from 16 May 1968 to 5 December 2016, consisting of 2,885,040 events and filter this catalog according to the following

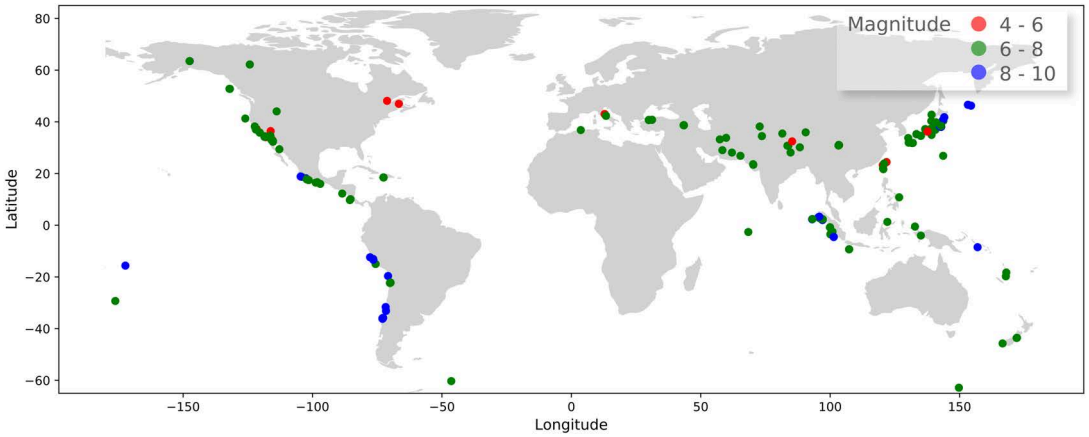

Figure 4.1: Map showing the locations of the 127 mainshocks, which are analyzed together with their associated aftershocks in this study.

procedure to select the aftershocks. First, we consider the 127 distinct mainshocks, with magnitudes ranging between 4.4 and 9.2 (Figure 4.1), related to the 277 finite-fault rupture models of the SRCMOD database by (Mai and Thingbaijam, 2014). For mainshocks with multiple slip models, we choose one at random, but we test the results' robustness to different choices by bootstrapping. All earthquakes that occurred within the first three months after each mainshock with horizontal distances less than 100 km from the mainshock's fault and depths less than 50 km are selected. Note that the hypocenters of six out of the 127 considered mainshocks are deeper than 50 km, but we have verified that their exclusion does not significantly affect our results. Although some aftershocks are likely to occur after the selection period, we choose the three months to limit the contamination by background activity because the relative fraction of background events increases with time. The filtered catalog finally contains 54,032 events.

For each mainshock, we calculate the static stress changes in the same crustal volume in which the aftershocks were selected, i.e., within horizontal distances up to 100 km from the mainshock's fault and depths between 0 and 50 km. Specifically, we use the PSGRN + PSCMP code by (Wang et al., 2006) to calculate the stress change tensor on a regularly gridded volume with a grid spacing of 5 km in all three dimensions. Using the calculated stress change tensor, we compute the Coulomb failure stress (ΔCFS) at each grid point based on different assumptions for the receiver mechanism (MAS, OOP, VM) and two alternative simple stress scalars (MS, VMS), which are good predictors of the spatial aftershock distribution (Meade et al., 2017; Sharma et al., 2020). In particular, we determine the following five stress metrics:

MAS: In this case, $\Delta\text{CFS} = \Delta\tau - \mu\Delta\sigma$ is calculated for a master fault orientation (MAS). In particular, the shear stress changes $\Delta\tau$ and the changes of the effective normal stress $\Delta\sigma$ are calculated for receivers with the mainshock mechanism. Here, we use $\mu = 0.4$ as the effective friction coefficient. MAS is a classical way of calculating stress changes, but it can erroneously indicate negative stress changes at aftershock locations because it ignores heterogeneities, model uncertainties, and variable aftershock mechanisms (Steacy et al., 2005c; Hainzl et al., 2009).

OOP: ΔCFS is calculated on receivers optimally oriented to the total stress, which is the sum of the stress change tensor and the background stress field. We assume a background stress field with principal stress components σ_1=1, σ_2=0, and σ_3=-2 MPa, oriented in a way that the background stress is optimally oriented for the mainshock rupture. Note that the 3 MPa differential stress of the background stress field agrees with the average stress drop of interplate earthquakes (Allmann and Shearer, 2009b). The assumed small

background stress can be considered as one end member case, while MAS is the other end member, as OOP converges to MAS at larger values.

VM: Here, a distribution of receiver mechanisms is considered, for which the average value

$$\overline{\Delta\mathrm{CFS}} = \frac{1}{N_p}\sum_{i=1}^{N_p} \Delta\mathrm{CFS}_i \cdot H(\Delta\mathrm{CFS}_i)$$

is calculated by Monte-Carlo sampling of the receiver mechanisms (Hainzl et al., 2010b; Bach and Hainzl, 2012). We use $N_p = 1500$ samples from normal distributions centered around the mainshock mechanism, with standard deviations of 30° for the strike, dip, and rake. Note that the Heaviside ($H(x) = 1$ for $x > 0$ and 0 else) accounts for the fact that only on faults with positive stress changes are any aftershocks expected.

MS: Maximum shear is calculated by $(\chi_1 - \chi_3)/2$, where χ_1 and χ_3 are the largest and smallest eigenvalues of the deviatoric stress change tensor.

VMS: The von-Mises stress is a scaled version of second invariant of the deviatoric stress change tensor (DeVries et al., 2018).

We use the stress calculations from our previous study, where detailed information is provided (Section 3 in Sharma et al. (2020)). The stress metrics are calculated for a layered half-space, where the layering is based on the CRUST 2.0 (Bassin, 2000) velocity model. Each aftershock is then associated with the stress scalars calculated at the grid point closest to the event's hypocenter.

Furthermore, we compute the minimum distance (R) to the respective mainshock's rupture for each aftershock. Specifically, R is defined as the minimum three-dimensional distance between the aftershock's hypocenter and the rupture area. Because slip estimations are smoothed and usually inverted on large fault planes, slip inversions include many patches with insignificant slip values. Thus, we define the rupture area by the patches where slip exceeded a certain level, namely 80% of maximum slip. Results for other choices are shown in the supplementary material.

The varying completeness levels of the mainshock-aftershock sequences are considered in detail. Local earthquake data are only complete above a basic completeness level $M_{c,0}$ which depends on the seismic network configuration and environmental noise conditions. This value defines the minimum magnitude, which can generally be detected everywhere in the selected region. However, immediately after a mainshock, a catalog is incomplete even above $M_{c,0}$ because of seismic noise due to overlapping waveforms (Kagan, 2004; Hainzl, 2016). We account for the short-time aftershock incompleteness (STAI) by assuming $M_c(M_m, t) = \max\{M_m - 4.5 - 0.75\log(t), M_{c,0}\}$, where t (in days) denotes the time since the mainshock, and magnitude M_m the mainshock's magnitude (Helmstetter et al., 2006; Hainzl, 2016). Here, the value of $M_{c,0}$ was independently estimated for each mainshock-aftershock sequence by the maximum curvature method (Wiemer and Wyss, 2000). Four examples are presented in the supplementary Fig. S11.

Thus, we end up with a combined earthquake catalog where each aftershock with magnitude larger than $M_c(M_m, t)$ is listed with its attributes, namely its fault distance and the five stress metrics listed above. In particular, the catalog includes for each aftershock (1) the mainshock magnitude, (2) the event magnitude, (3) the completeness magnitude $M_c(M_m, t)$ at the time of its occurrence, (4) the time relative to the mainshock, (5) R, and (6-10) the five different stress metrics. This data set is then analyzed to explore the potential dependencies of the GR and OU parameters on distance and stress metrics.

The selected events (aftershocks) are then divided into either distance or stress bins to study the dependence of the seismicity parameters on distance and stress. To account for strongly varying aftershock numbers, we use logarithmic bins. For presentation purposes, we also consider cumulative values for all events with distances smaller than R or absolute stress changes larger than S. In this way, we highlight for small R and large S values the results for events most affected by the mainshock.

4.2.1 b-value estimation

We use a modified version of Aki's maximum likelihood estimator (MLE) (Aki, 1965) to estimate the b-value for the case of time-varying completeness magnitude. For a given bin with index n, the b-value can then be estimated by considering the magnitude differences of the events relative to their individual completeness values, $M_c(M_{m,i}, t_i)$, at their occurrence times t_i as

$$b_n = \left\{ \ln(10) \left[\sum_{i=1}^{N_n} M_i - M_c(M_{m,i}, t_i) \right] / N_n \right\}^{-1} \tag{4.3}$$

and the standard error of b-value is estimated by $b_n^{err} = b_n / \sqrt{N_n}$.

4.2.2 OU parameters estimation

To estimate the parameters of Eq. (4.2), we maximize the log-likelihood function of the selected events with magnitudes above the completeness magnitude (Zhuang et al. (2012))

$$LL = \sum_{i=1}^{N_n} \ln \lambda(t_i) - \int_0^T \lambda(u) du \tag{4.4}$$

where the time t_i of the events is measured relative to the mainshock occurrence time. Here, we also account for a constant background rate μ using $\lambda(t) = \mu + K(c+t)^{-p}$. The aftershock numbers have to be normalized by the affected crustal volume to obtain the aftershock density, which can be compared for different bins. For this purpose, K is divided by the total number of grid cells with values (distance or stress metric) falling in the corresponding bin, leading to the normalized value K_n.

Eventually, the total aftershock density also depends on the c and p. It can be calculated analytically by integrating the OU law over the considered time interval $[0, T]$, which is given for $p \neq 1$ by

$$D = \frac{K_n}{p-1} \{ c^{1-p} - (c+T)^{1-p} \} \tag{4.5}$$

where we consider the activity in the first month, i.e., $T = 30$ days. To check the consistency of the parameter estimations, we compare D with the observed aftershock densities D_{obs} within the same period. We find that $D_{obs} = \mu T + D$, as theoretically expected from the maximum likelihood method (Iwata, 2016).

We note that, in contrast to b and p, the estimated values of c, K_n and D are affected by the catalog's short-term aftershock incompleteness (STAI). However, for each mainshock-aftershock sequence, STAI can be expected to similarly apply to the whole region. During the periods with a high seismicity rate immediately after the mainshock, the phases of small magnitude events, independently of where they are exactly located, cannot be recognized by the standard algorithms applied to the seismograms recorded at the regional seismic stations (Hainzl, 2016). Thus, the same fraction of events is missed in all locations, respectively in all stress and distance

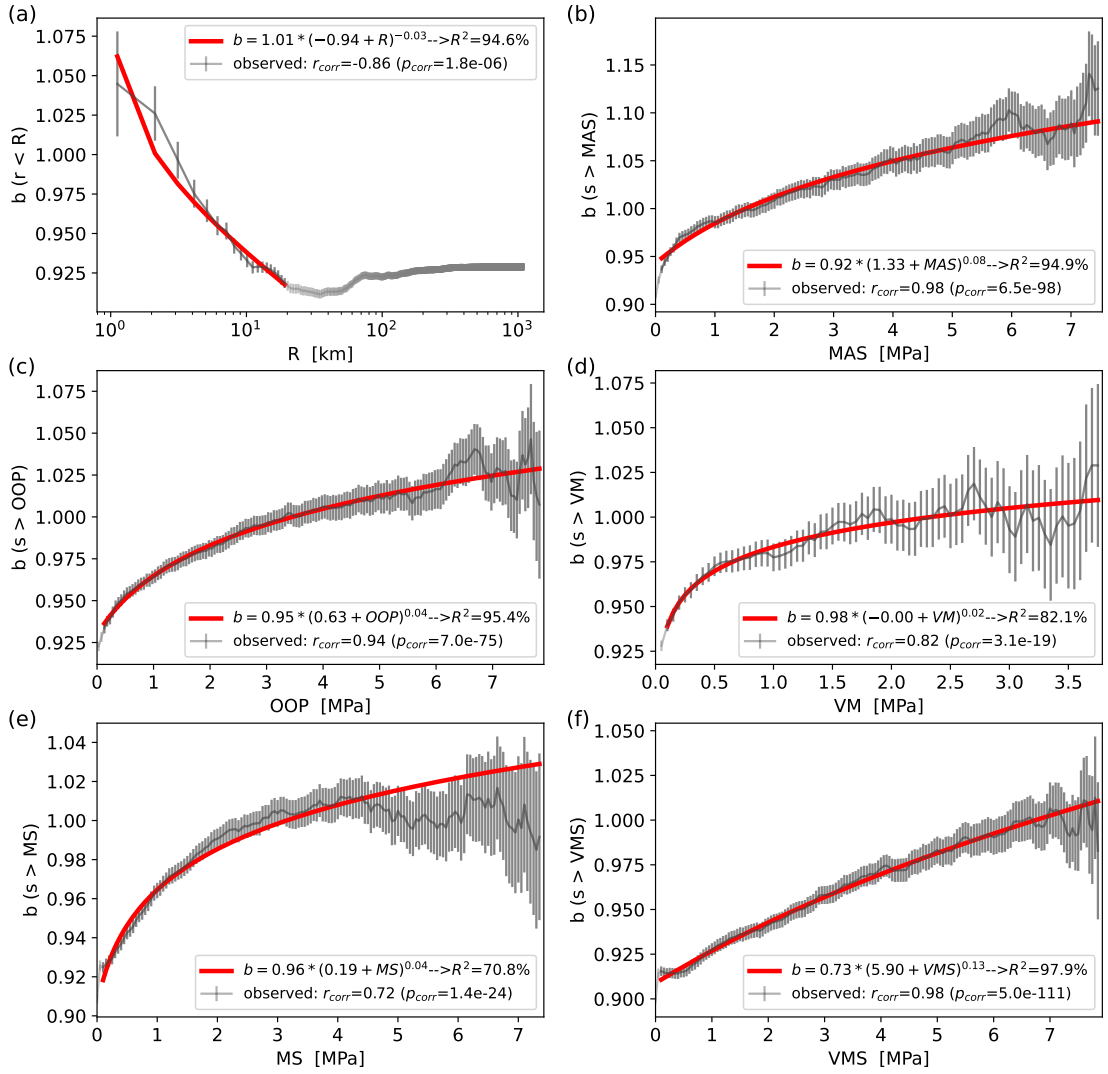

Figure 4.2: Main figures (a-f) show b-value calculations as a function of minimum distance to the mainshock (a) and induced stress metrics (b-f). The error bars refer to plus/minus one standard deviation. The intervals of the fits are marked by the black symbols, spanning [0, 20] km and [0.1, ∞] MPa, respectively. The legends give the associated fit parameters and the correlation coefficients with corresponding p_{corr}.

bins. Any systematic variation of the OU parameters with distance or stress metric, therefore, cannot be explained simply by incomplete data and likely have a physical reason.

4.3 Results

The estimated b-values are shown for cumulative bins in Figure 4.2, while a plot with non-cumulative bins can be found in the supplementary material (Fig. S6). The different panels show the dependence of the estimated b-value on either the distance or one of the stress metrics (MAS, OOP, VM, MS, and VMS). In all cases, the b-value varies systematically in a similar manner. The regions most affected by the mainshocks, i.e., with small distances and large stress changes, have a b-value of at least one, significantly higher than the b-value of about 0.9 for activity in distant regions and small stress changes. The difference is largest in regions with positive MAS values, where b varies between 0.9 and 1.1. Almost half of the aftershocks (48%) occur in regions with negative MAS values, where b also increases with the absolute stress change, but to a smaller extent. A similar but less significant trend is observed for OOP, where 22% of the aftershocks occur in stress shadows. However, because negative stress

metric	**parameter**	**fit function**	c_1	c_2	c_3	R^2	r_{corr}	p_{corr}
R	b	$c_1 + c_2 R$	0.98	-0.007	-	25.6%	0.51	1.0e-19
		$c_1(c_2 + R)^{c_3}$	1.04	0.12	-0.06	28.4%		
	c	$c_1 + c_2 R$	0.0177	0.0007	-	-1.52%	0.032	0.854
	p	$c_1 + c_2 R$	0.6021	0.0028	-	35.21%	0.607	0.000
	D	$e^{c_1} r^{c_2}$	-0.4434	-1.2105	-	96.0%	-0.176	0.207
MAS (>0)	b	$c_1 + c_2 S$	0.89	0.030	-	42.6%	0.65	2.0e-24
		$c_1(c_2 + S)^{c_3}$	0.93	0.20	0.06	46.3%		
	c	$c_1 + c_2 S$	0.1938	-0.0684	-	24.62%	-0.521	0.067
	p	$c_1 + c_2 S$	0.8329	-0.0825	-	28.94%	-0.538	0.057
	D	$e^{c_1} S^{c_2}$	-3.3949	0.5983	-	89.0%	0.336	0.074
OOP (>0)	b	$c_1 + c_2 S$	0.88	0.023	-	42.1%	0.65	1.2e-38
		$c_1(c_2 + S)^{c_3}$	0.87	0.81	0.08	45.4%		
	c	$c_1 + c_2 S$	0.0913	-0.0174	-	13.34%	-0.430	0.005
	p	$c_1 + c_2 S$	0.8087	-0.0421	-	30.40%	-0.551	0.000
	D	$e^{c_1} S^{c_2}$	-3.8054	0.3736	-	91.0%	0.913	9.44e-19
VM	b	$c_1 + c_2 S$	0.91	0.037	-	19.2%	0.44	1.4e-13
		$c_1(c_2 + S)^{c_3}$	0.96	0.08	0.04	25.0%		
	c	$c_1 + c_2 S$	0.0455	-0.0122	-	1.63%	-0.188	0.227
	p	$c_1 + c_2 S$	0.7517	-0.0923	-	18.22%	-0.426	0.004
	D	$e^{c_1} S^{c_2}$	-3.2497	0.4103	-	96.0%	0.919	1.521e-21
MS	b	$c_1 + c_2 S$	0.88	0.028	-	38.8%	0.62	2.2e-43
		$c_1(c_2 + S)^{c_3}$	0.74	2.86	0.15	41.1%		
	c	$c_1 + c_2 S$	0.0902	-0.0177	-	5.09%	-0.230	0.127
	p	$c_1 + c_2 S$	0.8139	-0.0461	-	1.10%	-0.344	0.020
	D	$e^{c_1} S^{c_2}$	-3.8774	0.4878	-	97.0%	0.950	2.177e-24
VMS	b	$c_1 + c_2 S$	0.888	0.014	-	22.9%	0.48	2.3e-23
		$c_1(c_2 + S)^{c_3}$	0.01	64.35	1.00	22.9%		
	c	$c_1 + c_2 S$	0.1584	-0.0287	-	30.35%	-0.5659	0.000
	p	$c_1 + c_2 S$	0.8752	-0.0432	-	24.55%	-0.506	0.001
	D	$e^{c_1} S^{c_2}$	-4.2422	0.5087	-	97.0%	0.960	1.67e-20

Table 4.1: Fits and correlation coefficients of the seismicity parameters (b, c, p, D) estimated in non-cumulative and non-overlapping (independent) bins as a function of either the fault distance (r) in the case of the R metric or the induced stress (S) in the case of the stress metrics (MAS, OOP, VM, MS, and VMS). The fit functions are given in the third column, while the resulting parameters of the weighted least squares fits with the corresponding variance reduction R^2 are given in columns 4-7 (corresponding to the fits in Figures 4.3-4.4 and S2). The last two columns give the Pearson's correlation coefficient and its p-value.

change estimates are likely related to unaccounted slip model uncertainties, heterogeneities, and variable receiver mechanisms (Steacy et al., 2005c; Hainzl et al., 2009), we do not focus on those results further.

For all other stress metrics, the stress values are only positive, and b increases monotonically with stress change. In contrast, b decreases in a non-linear manner monotonically with increasing R. In all cases, the shape is non-linear and can be approximated quite well by a power-law of the form $c_1(c_2 + x)^{c_3}$, where x is either distance or stress change. The corresponding fitting parameters and variance reduction are provided in the legends of Fig. 4.2 for the cumulative bins and Tab. 4.1 for the non-cumulative bins. In addition, Fig. 4.2 and Tab. 4.1 give the Pearson's correlation coefficient between the metric values and the estimated b-value. The observed correlation is found to be highly significant in all cases, with coefficients up to 0.98 and 0.65 for cumulative and non-cumulative bins, respectively.

The maximum likelihood estimations of the OU parameters are shown for non-cumulative bins in Figure 4.3, where the standard errors of the parameters are determined by the inverse of the Hessian matrix of the log-likelihood function (Eq. 4.3). The corresponding result for cumulative bins and examples of the OU fits can be found in the supplementary material. Similar to the b-value, all OU parameters show systematic trends. Although c and p estimations

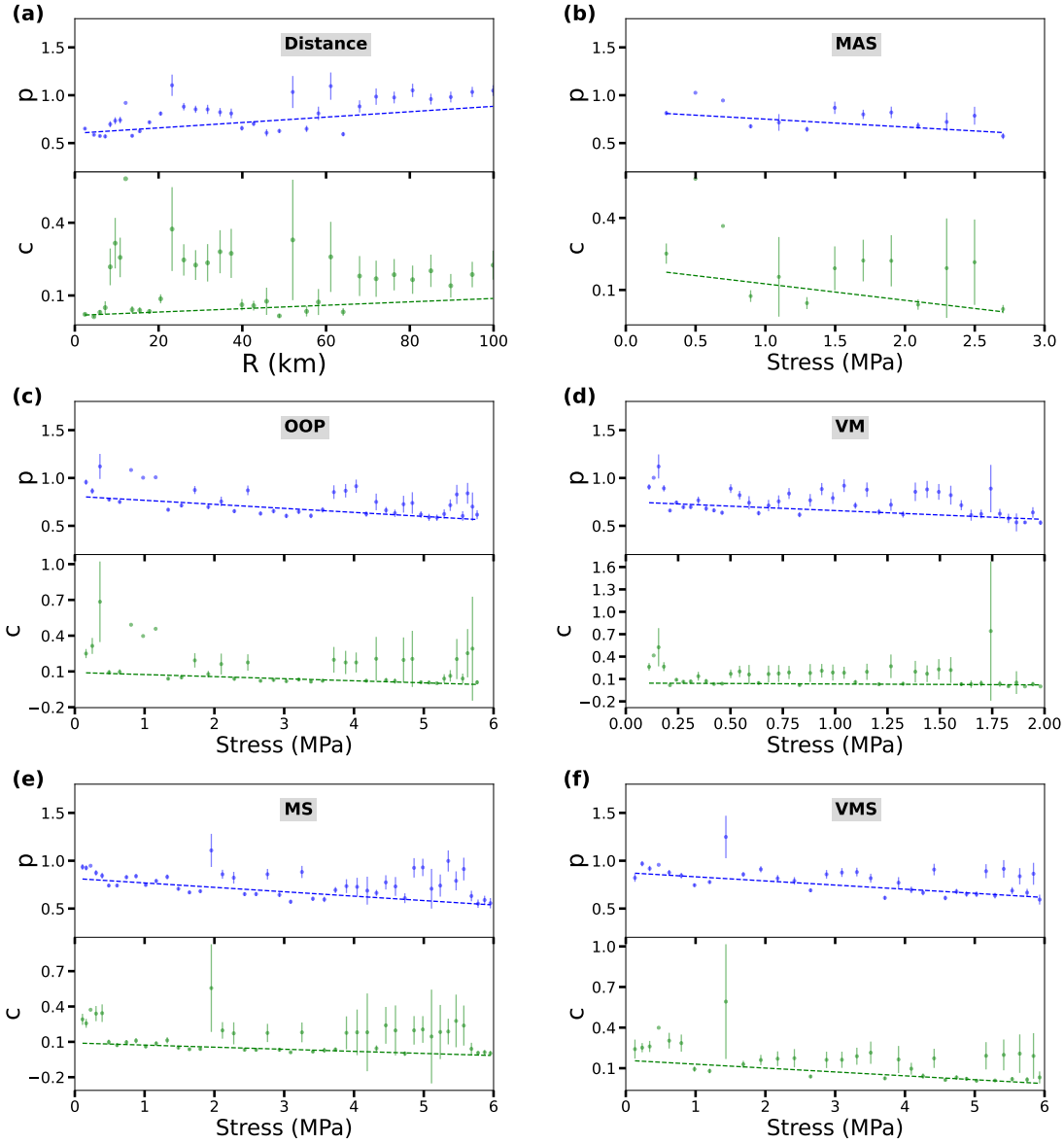

Figure 4.3: Main figures (a-f) show the estimated OU parameters as a function of the minimum distance to the mainshock (a) and induced stress metrics (b-f). The blue and green points and bars refer to the estimated p and c values with their uncertainties (plus/minus one standard deviation), respectively. The dashed blue and green lines represent the corresponding linear regressions with parameters provided in Tab. 4.1

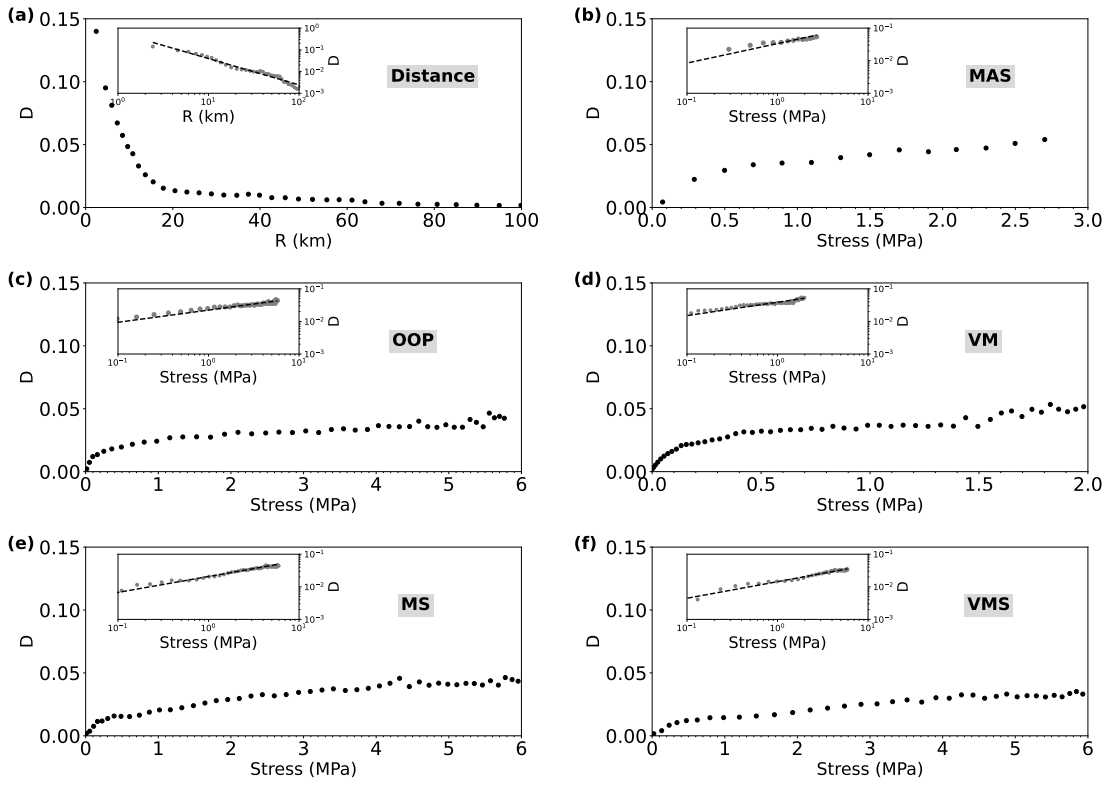

Figure 4.4: Observed aftershock density as a function of minimum distance from the mainshock and induced stress (a-f). The inset figures show the same results for a log-log scale, with lines representing the linear regressions.

are scattered, their trend can be approximated by a linear regression line in all cases (dashed lines in Figure 4.3). The corresponding fitting parameters and variance reduction values are provided in Tab. 4.1. While both parameters increase with increasing distance, they decrease with increasing stress values. This observation implies that the areas most affected by the mainshocks tend to have smaller c and p values than the almost undisturbed areas in the far-field.

The aftershock density depends on the combination of all three OU parameters according to Eq. (4.5). Figure 4.4 shows the aftershock density as a function of distance and stress metric. The decay of the aftershock density with distance follows approximately a power law. In contrast, the density of triggered aftershocks grows monotonously with the stress change. For all stress metrics, the density increases according to a power law, S^{κ} with exponents κ in the range between 0.37 and 0.60.

All correlation coefficients between the seismicity parameters and the metrics (stresses and fault distances) and the corresponding fit results with their variance reductions are given in Tab. 4.1. Out of the stress metrics, the highest correlation and variance reduction is observed for MAS and OOP in the case of b and p. At the same time, VMS and MS best describe the aftershock density.

4.4 Discussion and Conclusion

Our results show that the b-value of aftershocks increases for increasing values of the stress change caused by the mainshock. Assuming uniform prestress, our results indicate that the b-value positively correlates with absolute stress. This observation is in apparent contradiction to previous observations and models. Laboratory experiments show that the b-value of acoustic

events is inversely related to the differential stress accumulated in the source volume (Scholz, 1968; Wyss et al., 1973). Using a simple model to approximate the absolute stress state, Scholz (2015) proposed that b decreases linearly with stress for both continental and subduction zone environments. In accordance, thrust events have lower b-values as they are under higher stress than normal faults (Schorlemmer et al., 2005). The observed dependence of b on depth is also explained by increasing lithostatic stress and decreasing heterogeneity (Mori and Abercrombie, 1997; Spada et al., 2013). The effective stress acting on a fault is considered to be the only unifying factor to explain the spatial and temporal variation of b-value (El-Isa and Eaton, 2014). Once a rupture starts propagating in a highly stressed region, it is less likely to be stopped by heterogeneities, which results in larger earthquakes on average and explains the lower b-value.

In contrast to previous studies, our analysis (Figure 4.2b-f) shows an increase in the b-value with increasing stress changes and hence absolute stress, assuming uniform prestress. However, some key points should be noted here. Firstly, we analyze a global data set with mainshocks consisting of all faulting styles. Secondly, we focus on aftershocks, i.e., earthquakes that follow strong ground shaking. For aftershocks, Frohlich and Davis (1993) already found that the b-value is high near the mainshock region where the stress changes are largest. Our results are also in agreement with Gulia et al. (2018), who observed, for 58 aftershock sequences, a 20-30% increase in b-value for aftershocks and a b-value decay with distance to the mainshocks. Although we have no temporal resolution, we also observe the highest b-values in the areas most affected by the mainshocks (Figure 4.2). Using a simplified model and parameter assumptions, Gulia et al. (2018) demonstrated that the average differential stress change after an earthquake is negative, where the stress drop decreases with the distance to the rupture. This result can explain the b-value increase with decreasing distance, considering the results of the laboratory studies (Scholz, 1968; Wyss et al., 1973). However, it cannot simultaneously explain the triggering of the aftershocks, which are expected in places where stress locally increases. For demonstration, we perform a synthetic experiment similar to Gulia et al. (2018), which is described in detail in the supplementary material. For a synthetic magnitude 7.0 strike-slip earthquake, we calculate the stress changes and aftershock rates on a 3D grid of 1 km spacing by applying the Coulomb rate-state model (Dieterich, 1994). In agreement with the results of (Gulia et al., 2018), the average shear stress decreases, i.e., the average shear stress change is negative. However, most aftershocks occur where the stress increases locally. To determine the b value for the overall activity, we use the inverse relationship between the average earthquake magnitude and the b value (Aki, 1965). In contrast to the observations, we show that the b-value decreases, when an anti-correlation between stress change and b-value change is assumed, i.e., the b value is dominated by the majority of aftershocks occurring in areas of stress increase. Instead, assuming the positive correlation (i.e., $\Delta b = 0.03 \cdot \Delta MAS$ in Tab. 4.1) yields b-value changes that are consistent with the empirical observations of Gulia et al. (2018). Thus, the previous explanation of the increased b values of aftershocks as a result of the laboratory-derived anti-correlation with stress is not valid, and the observed positive correlation between b and stress changes requires alternative explanations.

At least two other factors that could explain b value variations must be considered: structural heterogeneity and strength variations, which can partially explain the observations. Large earthquakes occur on preexisting faults with surrounding damage zones, where the damaged rock is highly fractured and fault lengths are shorter (Kim et al., 2004; Powers and Jordan, 2010). Thus, aftershocks nucleating in the damage zone are likely to stop earlier due to heterogeneities and finite fault lengths, resulting in smaller average magnitudes. Because of the inverse relationship between mean magnitude and b-value, the earthquakes in the damage zone are expected to have larger b-values than events nucleating in more intact crustal volumes. Furthermore, the intense shaking induced by the mainshock in the near-field might weaken the rock. The reduced strength of the rocks facilitates the triggering of aftershocks, especially

where the induced stress change is large. However, the strength reduction lowers the stress drop of the events, making it more difficult for the rupture to propagate and limiting its magnitude. Thus, our observations can be explained by a decrease in structural heterogeneity and strength with increasing distance from the mainshock rupture.

Like the b-value, the c-value has also been proposed to depend on stress based on laboratory studies, field observations, and seismicity models. For acoustic events in rock experiments, Smirnov et al. (2019) observed an exponential decrease of c with Coulomb stress. Narteau et al. (2009) found the smallest c values for thrust events and intermediate and largest values for strike-slip and normal mainshocks, respectively. They explain this observation by varying principal stresses with the largest values for thrust events. Finally, the rate and state (RS) seismicity model of Dieterich (1994) predicts that $c \propto \exp(-S/A\sigma)/[1 - \exp(-S/A\sigma)]$. Here, $A\sigma$ is a constitutive parameter of the RS friction law governing fault friction in laboratory experiments, where σ is the effective normal stress. For stress changes S much larger than $A\sigma$, the RS model thus predicts that c exponentially decreases with S according to $c \propto \exp(-S/A\sigma)$, similarly to the results of Smirnov et al. (2019).

However, c-values for earthquake catalogs are usually difficult to determine because of the short-term incompleteness of earthquake catalogs. Seismic networks are unable to detect all earthquakes in the first minutes to hours after mainshocks because of the overlapping waves of frequent aftershocks (Hainzl, 2016). Thus, it is not possible to reveal very small c values. This problem also applies to our study, where we cannot expect to see very small c-values. However, larger c values can be correctly detected. Our results show that the largest c-values occur in the far-field, where stress changes are the smallest. Thus, the observed trend agrees with previous laboratory studies and model predictions. However, the observed p-value decrease with stress contradicts the laboratory observations of Smirnov et al. (2019), who observed an almost linear increase.

In total, our results show that the aftershock activity in the near-field is characterized by high productivity and small c and p values, indicating that the activity starts to decay early but decays slower than in the far-field.

Finally, the aftershock density is found to scale with stress change magnitude according to S^{κ}. This observation does not agree with simple clock-advance models that predict a linear dependence between event numbers and stress change (Hainzl et al., 2010a). The observed power law dependence on S with exponents in the range 0.37-0.60 points to a non-linear process that may be related to plastic deformation in the damage zone.

In conclusion, our derived relations between mainshock-induced stress changes and the statistical properties of the earthquake magnitudes and clustering can be implemented in seismicity models, which might help to improve seismic hazard assessments for aftershocks in the future.

Chapter 5

Conclusion and outlook

In this thesis, I have explored various aspects of aftershocks, in particular their spatial distribution and seismicity parameters with respect to the stress changes resulting from mainshocks. What sets this study apart is the utilization of a large dataset and more precise stress calculations distinguishing it from previous research on similar topics. The data analysis involved two main steps: (1) calculating stress tensors from slip models and evaluating different stress metrics to identify the most effective one, and (2) utilizing these metrics to create a comprehensive aftershock catalog used to investigate the relationship between seismicity parameters and induced stress. Understanding the impact of stress metrics and their correlation with seismicity parameters is crucial for assessing future seismic hazards.

5.1 Conclusion

Overall, my pursuit of advancing aftershock forecasting, I explore stress metrics, particularly Coulomb failure stress (CFS), which explains aftershock locations but has limitations due to slip model uncertainties and receiver mechanism variability. I compare scalar (MS and VMS) and receiver-dependent (MAS, OOP, and VM) stress metrics, finding receiver-independent metrics like OOP and VM often outperform MAS. I also study the 2005 Kashmir mainshock-aftershock sequence using Coulomb failure stress with variable mechanism (VM), revealing the spatial distribution of aftershocks triggered by co-seismic or post-seismic slip on the mainshock fault. While studying the stress metrics a combined catalog of aftershocks parameters and along with stress (MAS, OOP, VM, MS and VMS) at their location has been generated. This catalog is then used to study the relation between seismicity parameters and induced stress. I observe an unexpected increase in aftershock b-values with rising stress changes. This finding hints at the influence of factors such as structural heterogeneity and strength variations on b-values, challenging conventional wisdom. Additionally, I unveil the intricate interplay between mainshock-induced stress changes and the statistical properties of aftershocks, offering valuable insights for seismicity models and hazard assessments. My research underscores the dynamic nature of aftershock forecasting, calling for continued exploration in this field.

My specific conclusions concerning my main studies are the following:

- **Best stress metric for aftershock forecasting (Chapter 2)**
  CFS has been widely used to explain aftershock locations and separate positive and negative stress change areas, it has been acknowledged that aftershocks frequently occur in regions with calculated negative stress changes, known as stress shadows. This phenomenon has been attributed to uncertainties in slip models and the variability of receiver mechanisms, both of which can affect CFS predictions.

  To improve the accuracy of CFS predictions, various modifications and alternative stress metrics have been explored. I compared different stress metrics, including scalar stress metrics (MS and VMS) and receiver-dependent metrics (MAS, OOP and VM), to assess

their effectiveness in forecasting aftershock activity. The analysis showed that accounting for the variability of aftershock mechanisms in the OOP and VM metrics resulted in significantly better performance compared to the MAS-value. However, scalar metrics still performed better than receiver dependent metrics. The same result is also confirmed in the recent study of Asayesh et al. (2023) for 2017-2019 western Iran sequence.

The success of the receiver-independent metrics may be related to the uncertainities of the stress calculation and the additional efect of dynamic and post-seismic (afterslip poro/visco elastic) triggering, as well as secondary aftershock triggering (aftershocks of aftershocks).

It is worth noting that the effectiveness of stress metrics may vary based on the tectonic region and the specific characteristics of the earthquake sequence being studied. Dynamic stress changes were not considered in this analysis, but it was observed that stress metrics worked best for the largest aftershocks occurring shortly after the mainshock. Further research is needed to investigate the impact of dynamic stress changes on aftershock forecasting.

In conclusion, this part indicates that Coulomb failure stress theory remains a valuable tool for understanding earthquake triggering physics, but its effectiveness for aftershock forecasting in regions with limited fault information may be limited and simpler stress metrics are preferable. The study also highlights the importance of accounting for uncertainties and receiver variability in stress calculations to improve the accuracy of aftershock forecasts. Ultimately, the selection of an appropriate stress metric for forecasting should consider the specific characteristics of the earthquake sequence and the available fault information.

My findings doesn't discard the use of Coulomb failure stress in general as it might still describe the true underlying physics for earthquakes triggering. However, in case of limited fault information, CFS is not the best choice for aftershock forecasting while it might be. Useful, if enough information is available.

– **Application of CFS-VM metric in 2005 Kashmir mainshock-aftershock sequence (Chapter 3)**
As a particular case study, I focused on the seismotectonics of the NW Himalayan syntaxis, investigating the 2005 Kashmir earthquake and its aftershocks. I used Coulomb failure stress with variable mechanism (VM) for the analysis of the mainshock-aftershock sequence. This act as a corroborating evidence for spatio-temporal evolution of the earthquake rupture. Limited availability of data also make CFS a crucial step in understanding the triggering of aftershocks following the Kashmir mainshock rupture.

The mainshock occurred on the Muzzafarabad-Tanda fault, an active thrust fault southwest of the MBT syntaxis. It was characterized by a bilateral rupture, propagating both southeast and northwest. Through detailed modeling, it was determined that the mainshock fault had an oblique thrust mechanism on a northeast-dipping plane at approximately 10 km depth.

I performed a comprehensive analysis of Coulomb failure stress to compute stress changes on the aftershock fault planes. I observed that the moderate-to-large aftershocks, located northwest of the mainshock rupture, occurred in regions with positive Coulomb stress change. This suggests that these aftershocks were likely triggered by either co-seismic or post-seismic slip on the mainshock fault. Furthermore, the aftershocks were concentrated at the edge of the rupture termination as a blind thrust, likely occurring on the Indian Kohistan Suture Zone (IKSZ), which is a northwestward extension of the mainshock fault.

I also investigated one specific aftershock, which occurred within 48 hours of the mainshock, close to the mainshock hypocenter. This aftershock had a thrust fault mechanism with a steep dip angle, indicating the possibility of being driven by residual stresses on a mainshock fault heterogeneity or occurring on a southwest-dipping back-thrust.

In summary, Coulomb stress analysis proved valuable in revealing the spatial distribution and triggering mechanisms of aftershocks following the 2005 Kashmir earthquake. The study shed light on the complexities of faulting and rupture patterns in the NW Himalayan syntaxis, providing important insights into the seismotectonics of the region. Understanding such seismic processes is crucial for assessing seismic hazard and improving earthquake preparedness and mitigation efforts in this seismically active area.

– **Seismicity parameters dependence on induced seismic stress (Chapter 4)**
Utilizing the stress calculations, I studied the statistical properties of aftershocks and their correlation with mainshock-induced stress changes. One significant observation is the increase in the b-value of aftershocks with increasing stress changes caused by the mainshock. This finding is contrary to some previous laboratory experiments and models, which suggested an inverse relationship between the b-value and stress changes. The high b-values observed near the mainshock region, where stress changes are largest, align with earlier studies on aftershocks. Additionally, I observed the highest b-values in areas most affected by the mainshocks, further supporting the positive correlation between b-value and stress changes.

The contradictory results to lab experiments might be related to strength rather than stress changes. In particular, the variations in b-value could be attributed to structural heterogeneity and strength variations. Aftershocks occurring in damaged rock surrounding preexisting faults with shorter fault lengths may stop earlier due to heterogeneities, resulting in smaller average magnitudes and higher b-values. Intense shaking induced by the mainshock in the near-field could weaken the rock, facilitating aftershock triggering, especially where the induced stress change is significant. This reduced strength, however, limits the magnitude of aftershocks due to decreased stress drop, explaining the observed b-value increase with decreasing distance from the mainshock rupture.

Similar to the b-value, the c-value has been proposed to depend on stress based on laboratory experiments, field observations, and seismicity models, e.g. the RS seismicity model predicts an exponential decrease of c with stress changes in general. My observation of larger c-values in the far-field, where stress changes are smallest, are consistence with previous laboratory studies and those model predictions. However, the observed decrease in the p-value with stress changes contradicts some laboratory observations.

My study highlights the complexity of aftershock behavior and suggests that the aftershock activity in the near-field starts decaying early but decays slower than in the far-field. The scaling of aftershock density with stress change magnitude points to a non-linear process, possibly related to plastic deformation in the damage zone.

In conclusion, the relationships between mainshock-induced stress changes and the statistical properties of aftershocks revealed in this study offer valuable inputs for seismicity models. Implementing these findings may improve seismic hazard assessments for aftershocks, leading to better earthquake preparedness and mitigation strategies in the future. However, further research and data analysis are needed to fully understand the complex interplay between stress changes and aftershock behavior.

5.2 Outlook

The conclusions drawn from this study open up promising avenues for future research and applications in the field of seismology and earthquake forecasting. Several key areas can be explored to further advance our understanding of aftershock triggering and seismicity:

1. **Refining Stress Metrics**: While Coulomb failure stress (CFS) has been a valuable tool in studying aftershock triggering, there is room for improvement in stress metrics. Future research can focus on developing more accurate and reliable stress metrics that consider dynamic stress changes, poro/visco-elastic deformations, and other complex geological processes. These refined stress metrics may provide better forecasts of aftershock activity and improve seismic hazard assessments.

2. **Experimental Validation**: Laboratory experiments and controlled field studies can be conducted to validate stress-magnitude relationships and test the effectiveness of various stress metrics in real-world scenarios. Such validation is crucial for refining and calibrating forecasting models.

3. **Incorporating External Factors**: Investigate regional variability in stress-magnitude relationships, considering specific seismic zone characteristics for region-specific aftershock forecasting models. Additionally, prioritize improved fault data collection and advanced imaging techniques for accurate fault characterization, while incorporating geological and geophysical factors like fault heterogeneity, rock properties, and fluid movement to enhance forecasting models.

4. **Coupling with Other Models**: Integrating stress metrics with other earthquake forecasting models can enhance overall accuracy. For example, coupling stress-based models with machine learning techniques or time-dependent seismicity, such as the Epidemic-Type Aftershock Sequence models can provide more comprehensive and reliable aftershock forecasts.

5. **Real-Time Aftershock Forecasting**: Developing real-time aftershock forecasting tools based on stress metrics and other seismic parameters can significantly improve earthquake preparedness and response strategies. Such tools can help authorities make informed decisions and mitigate the impact of aftershock sequences.

Overall the conclusions drawn from this study highlight the importance of continuous research and development in aftershock forecasting and seismotectonics. By exploring the outlined research avenues, the seismic community can make significant strides in understanding earthquake triggering processes and mitigating the impact of aftershocks on vulnerable regions. Ultimately, the goal is to develop more accurate and reliable forecasting tools that can contribute to enhancing earthquake resilience and safety worldwide.

Supplementary information

Supplementary information for Chapter 2

1. Figure S1: Location of mainshocks from SRCMOD database on a global map.

2. Figure S2: Proximity test by excluding grid points (and aftershocks) in the vicinity of mainshock rupture.

3. Figure S3: ROC analysis for the distance-based model suggested by Mignan and Broccardo (2019) using Equation 5 of main text.

4. Figure S4: ROC analysis for OOP metric using different regional stress values. The mainshock is assumed to release all the regional stress $\Delta\sigma_0$, calculated by using the formula

$$\Delta\sigma_0 = -Gs/L \tag{5.1}$$

where, $G = 33$ GPa is the shear modulus, the mean slip s and rupture length L (Mignan, 2018). The background stress $\Delta\sigma_0$ is adjusted in such a way that the stress drop equals the shear stress for the mainshock mechanism before the occurrence of the event. We use three setups for the magnitude of the background stress: (i) a constant differential stress $\sigma_1 - \sigma_3 = 3$ MPa for all slip models, and $\sigma_1 - \sigma_3$ calculated individually for each mainshock using Eq. 5.1 with s equal to (ii) the mainshock slip (iii) or the mean slip.

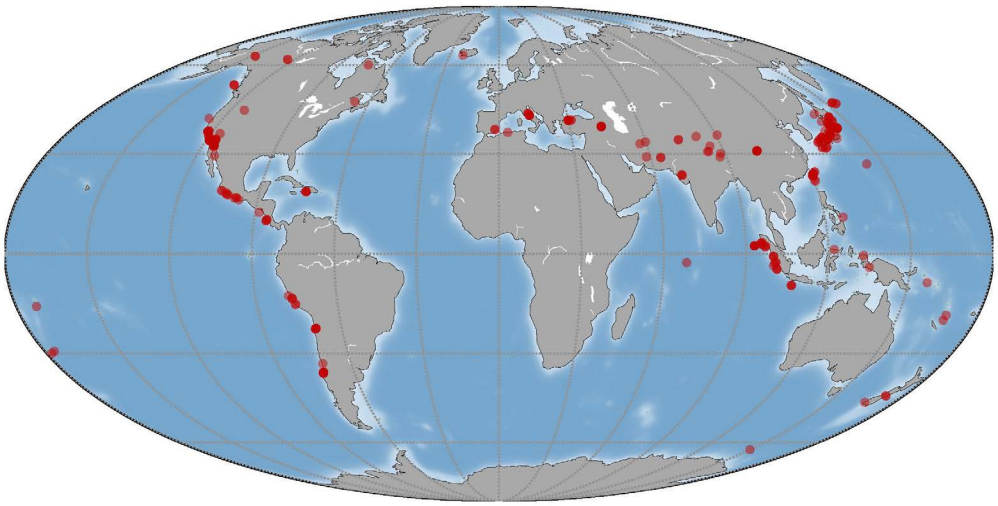

Figure S1: Epicenter location of mainshocks taken from SRCMOD database on a global map.

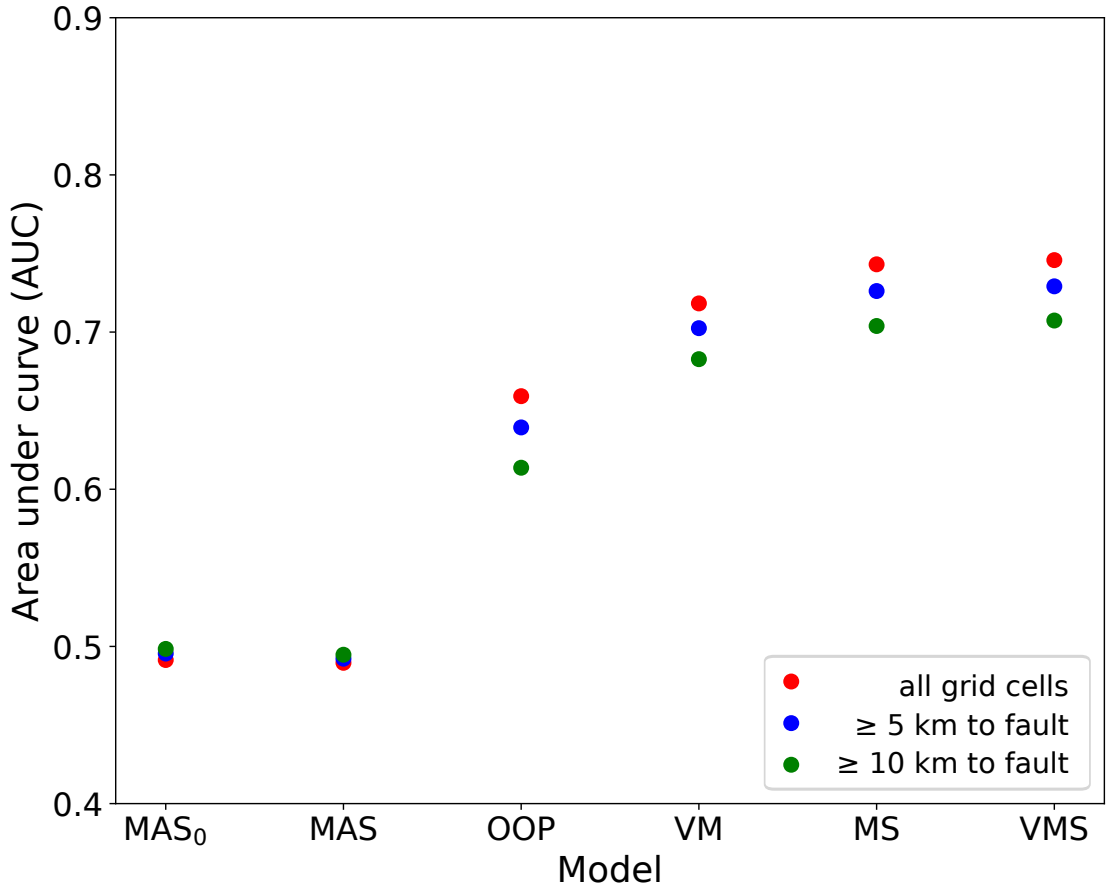

Figure S2: AUC values calculated by excluding grid points and aftershocks in the close proximity of the mainshock fault. Red dots are AUC values calculated without excluding any grid points. Blue and green dots are the AUC values calculated by excluding grid points within 5 and 10 km of the mainshock rupture, respectively.

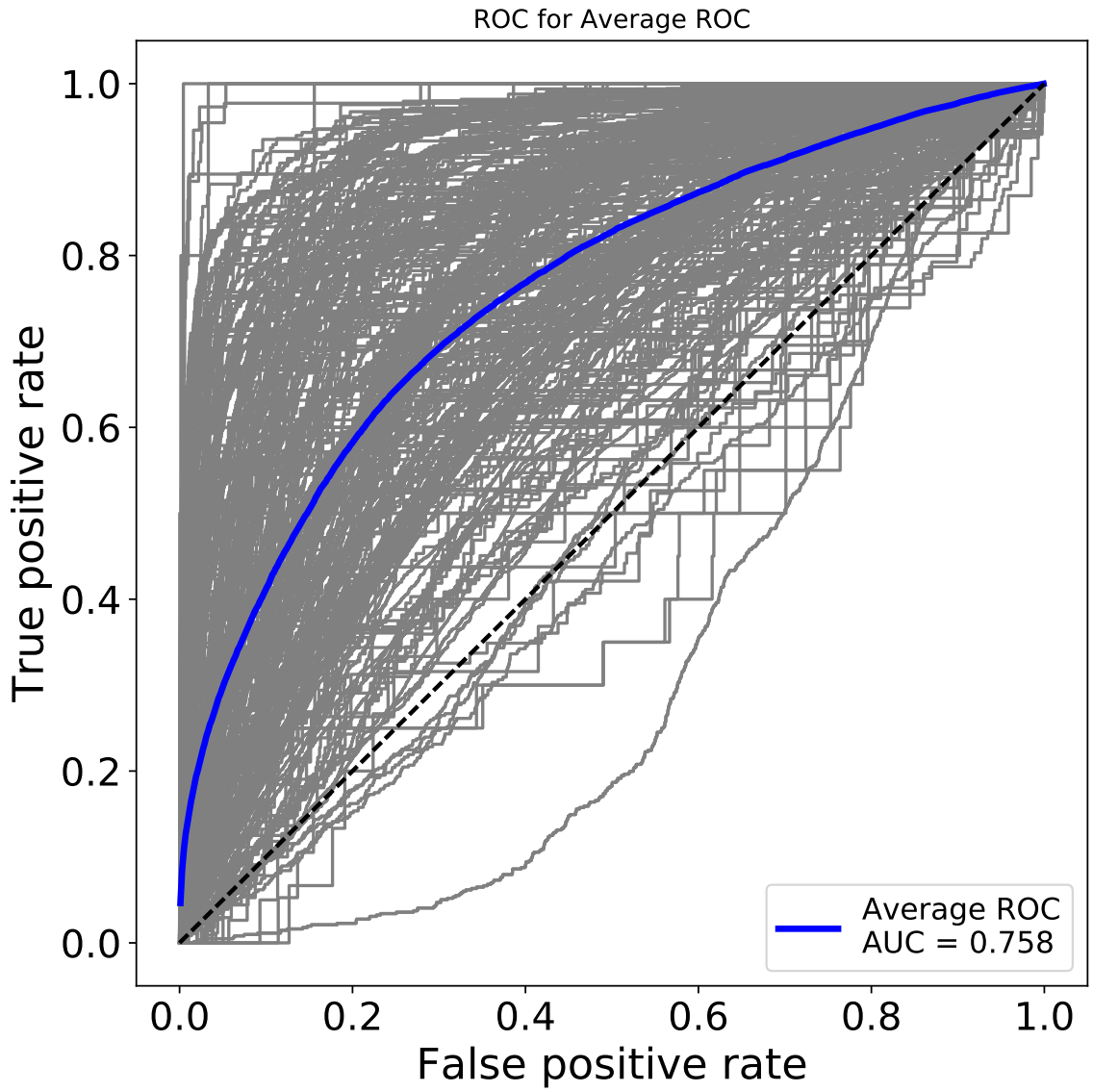

Figure S3: ROC curves for distance-based model, where thin lines refer to individual slip models and thick blue line is the binned average of all slip models.

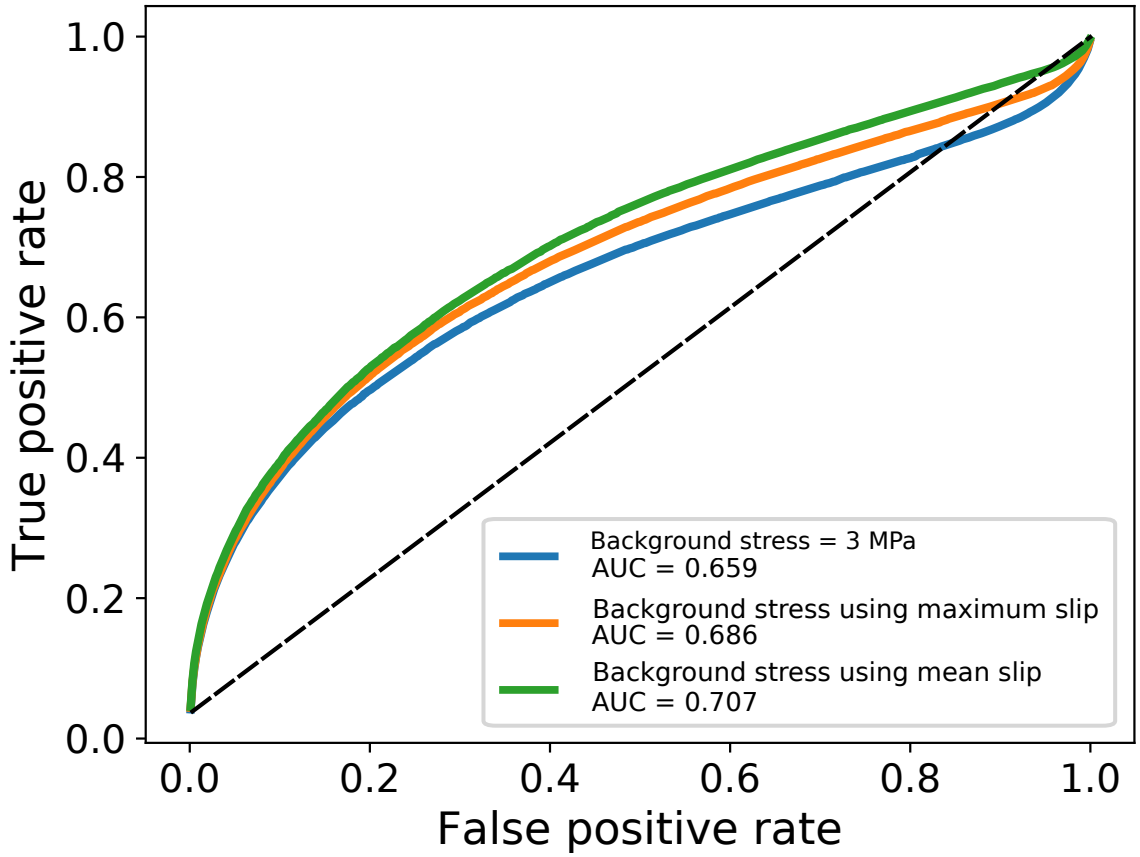

Figure S4: ROC analysis for alternative models of background stress amplitude which are considered for the OOP metric.

Supplementary information for Chapter 4

1. Supporting Figures S5-S13
2. Supporting Text describing our synthetic experiment similar to that of Gulia et al. (2018).

Supporting Figures

This file contains supporting figures as follows:

1. Figure S5: b-value estimation for different definitions of the distance (R) between aftershocks and the mainshock rupture, where the inset is a zoom into the first 15 km. R relates to the minimum distance of the aftershock's hypocenter to any of the slip patches related to the rupture. Because the slip inversions include many patches with insignificant slip, we define the rupture area by the patches where slip exceeded a certain level (see legend). Slip inversions usually use large fault planes to map the earthquake's slip and apply smoothing constraints. Thus, actual slip occurred likely only at a portion of the model space. The analysis of the different cutoff values shows that the b-value first increases and then decreases within the first kilometers if small slip patches are included. A continuous decay only occurs for rupture areas defined by the largest slip patches (>= 80% of maximum slip).
2. Figure S6: Corresponding figure to chapter Fig. 4.2 showing the estimated b-value as a function of the minimum distance from the mainshock rupture and induced stress metrics, but for non-cumulative and non-overlapping bins. Each bin consists of 300 earthquakes.
3. Figure S7: Corresponding figure to chapter Fig. 4.3 showing the maximum likelihood estimations of Omori-Utsu (OU) parameters, but for cumulative bins.
4. Figure S8: Exemplary frequency-magnitude distributions corresponding to b-values plotted in chapter Fig. 4.2. The examples refer to the beginning and end of the x-axis in Fig. 4.2.
5. Figure S9: Examples of Omori-Utsu parameters fit for R, MAS, OOP, VM, MS, and VMS.
6. Figure S10: Stress changes, seismicity rates, and b-value changes for a synthetic M7 strike-slip earthquake using the Coulomb Rate-State (CRS) model (see Supporting Text below for details).
7. Figure S11: Examples of frequency-magnitude distributions and the estimated maximum curvature magnitudes $M_{c,0}$.
8. Figure S12: The same figure as chapter Fig. 4.2, but for an increased $M_{c,0}$ value by 0.2.
9. Figure S13: Similar figure as chapter Fig. 4.2 but using reversed cumulative bins: The b-value is estimated using distances larger, respectively stress smaller than the given value on the x-axis.

Supporting Text

For the experiment, we assume a half-space with uniform pre-stress, where a magnitude 7.0 strike-slip earthquake occurs on a vertical fault. The rectangular rupture is centered at a depth of 10 km and has a length (L) and width (W) of $L = 58$ km and $W = 18$ km according to the scaling relationships of Wells and Coppersmith (1994). We calculate the stress changes in a 3D grid with 1 km spacing, symmetrically ordered around the rupture

plane with a minimum distance of 0.5 km, avoiding any singularities in the stress calculation. Furthermore, we use a shear modulus (μ) of 30 GPa and determine the uniform slip value (s) by the relation, $M_0 = \mu LWs$, where M_0 is the seismic moment corresponding to an M7 event. At each grid point, we calculate the stress tensor using the analytic solution (Okada, 1992) and determine the induced shear stress and the Coulomb Failure Stress (CFS), assuming the aftershock mechanisms to be identical to the mainshock's mechanism and a friction coefficient of 0.6. Figure S10(a) shows the mean stress changes in the three distance intervals $0 < R < 5$ km, $5 \leq R < 15$ km, and $15 \leq R < 25$ km, indicating that the shear stress and CFS indeed decrease, on average, as shown by Gulia et al. (2018).

However, due to the areas with positive stress changes, the total earthquake rate increases instantaneously and decays afterward with time t, according to the Coulomb Rate-State (CRS) model introduced by Dieterich (1994). In particular, the earthquake rate evolution with time for a stress step ΔS at time $t = 0$ is given by $R(t|\Delta S) = r/\left[\left(e^{-\Delta S/A\sigma} - 1\right) e^{-t/t_a} + 1\right]$, where we use typical values of $A\sigma = 0.02$ MPa and a relaxation time of $t_a = 1000$ days. The cumulative earthquake rates in the three different distance ranges are shown in Figure S10(b).

We assume a background b-value of one and that b depends on the stress change ΔS according to $b(\Delta S) = 1 + \kappa \Delta S$. Using the inverse relation between b and the mean earthquake magnitude $\bar{m}$ (Aki, 1965), $\bar{m}$ depends on ΔS according to $\bar{m}(\Delta S) = M_c + \log_{10}(e) \,/\, b(\Delta S)$, where M_c is the cutoff magnitude of the catalog. Thus, for each distance interval, we can calculate the average magnitude at time t by

$$\bar{m}(t) = \sum_i R_i(t|\Delta S_i)\, \bar{m}_i(\Delta S_i) \,/\, \sum_i R_i(t|\Delta S_i) \ ,$$

where i is the index of the grid nodes in the distance interval. Finally, we calculate the b-value of the cumulative activity by $b = \log_{10}(e)/(\bar{m}(t) - M_c)$. The results are shown in Figure S10(c) using shear stress changes and $\kappa = -0.0012$ according to Scholz (2015) and in Figure S10(d) using MAS and $\kappa = 0.03$ according to the results of our study. In contrast to the observations of Gulia et al. (2018) and our study, the b value is found to decrease slightly using the standard inverse relation between stress and b value. However, our derived relation leads to a significant b-value increase in agreement with the empirical observations.

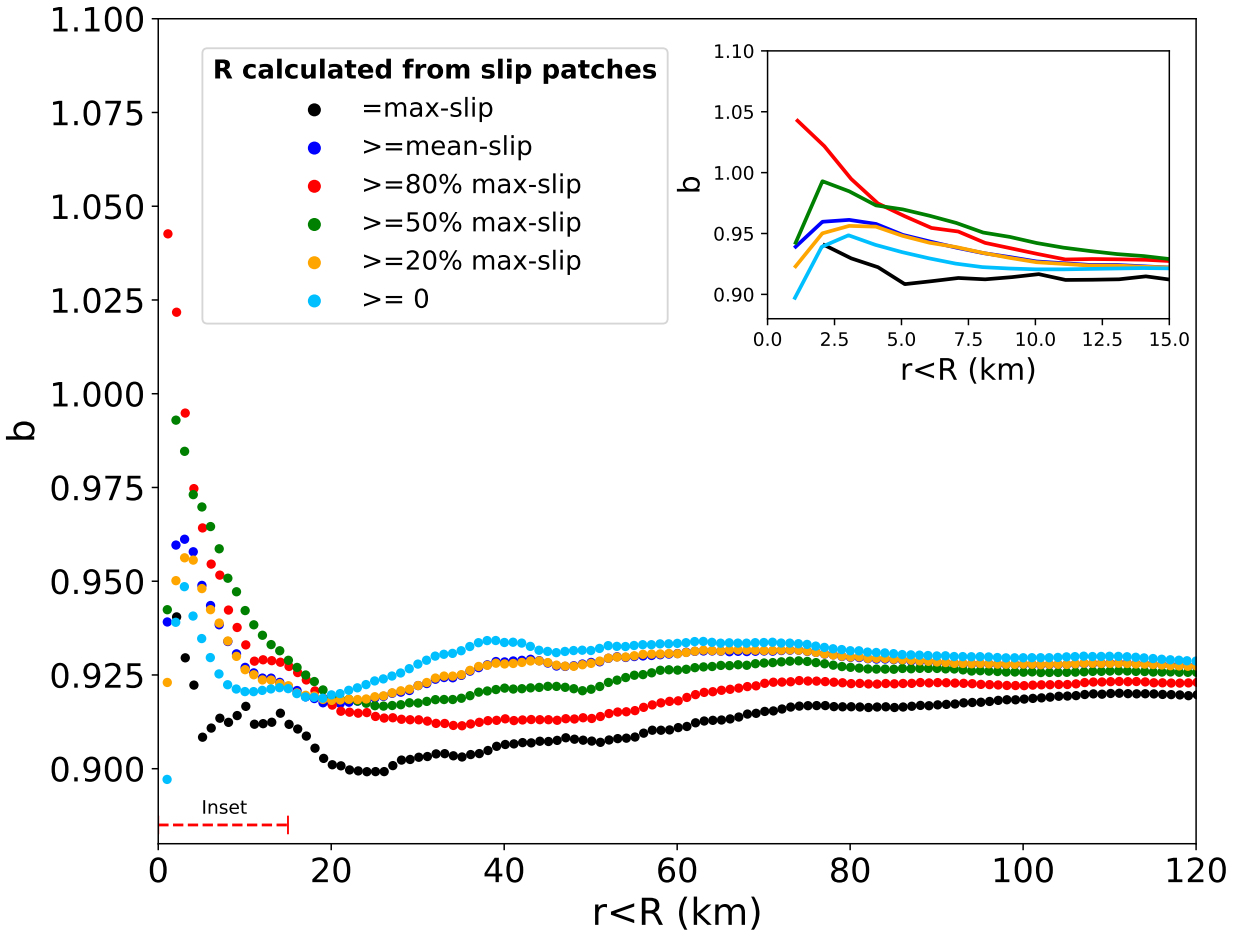

Figure S5: b-value variation with distance (R) to the mainshock for different definitions of the rupture area.

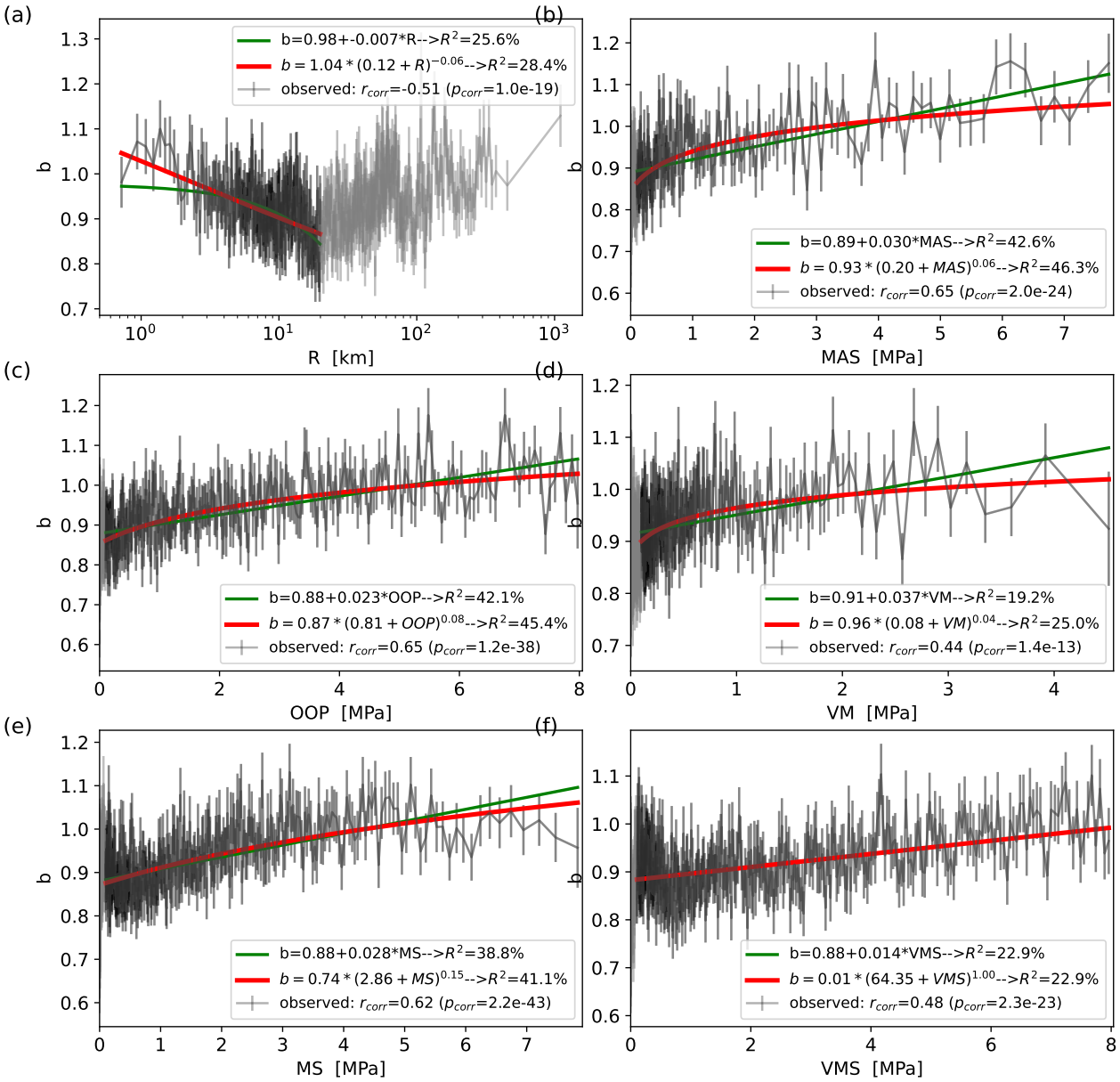

for non-cumulative and non-overlapping bins, where each bin includes 300 earthquakes. The lines refer to the functional fits provided in the legend, along with Pearson's correlation coefficient and its p_{corr}. Note that the fits are limited to regions with distances less than 20 km and stress exceeding 0.1 MPa, respectively, which are marked in black.

Figure S6: *b*-value estimates with their uncertainties

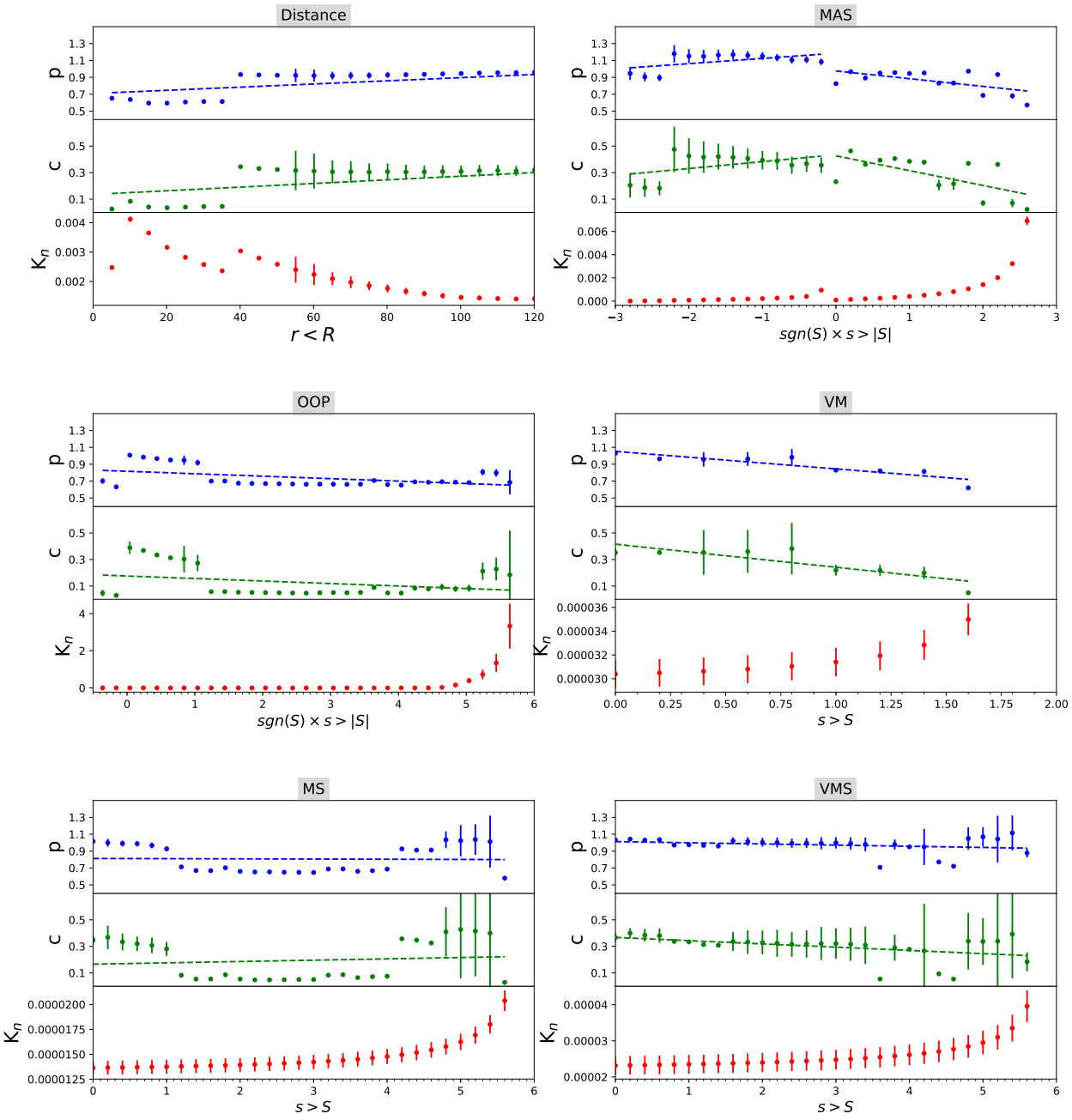

Figure S7: Maximum likelihood estimates of OU parameters for cumulative bins as a function of the minimum distance to the mainshock and induced stress metrics. The blue, green, and red dots refer to the p, c, and k_n values, respectively. Linear fits of p and c are shown by dashed lines.

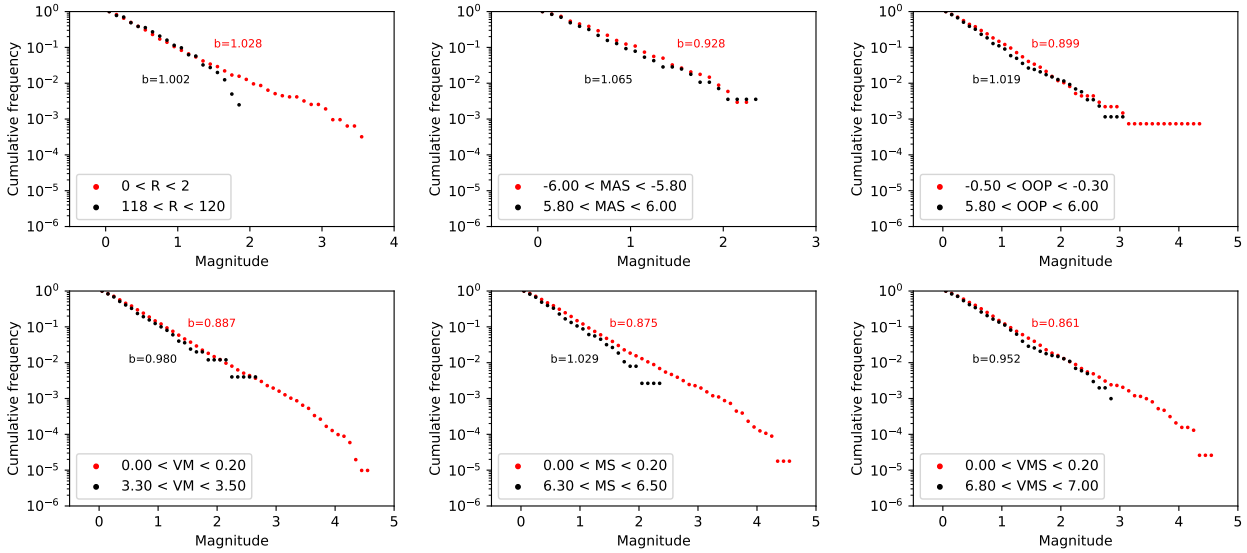

Figure S8: Exemplary frequency-magnitude distributions for selected bins of R and the different stress metrics.

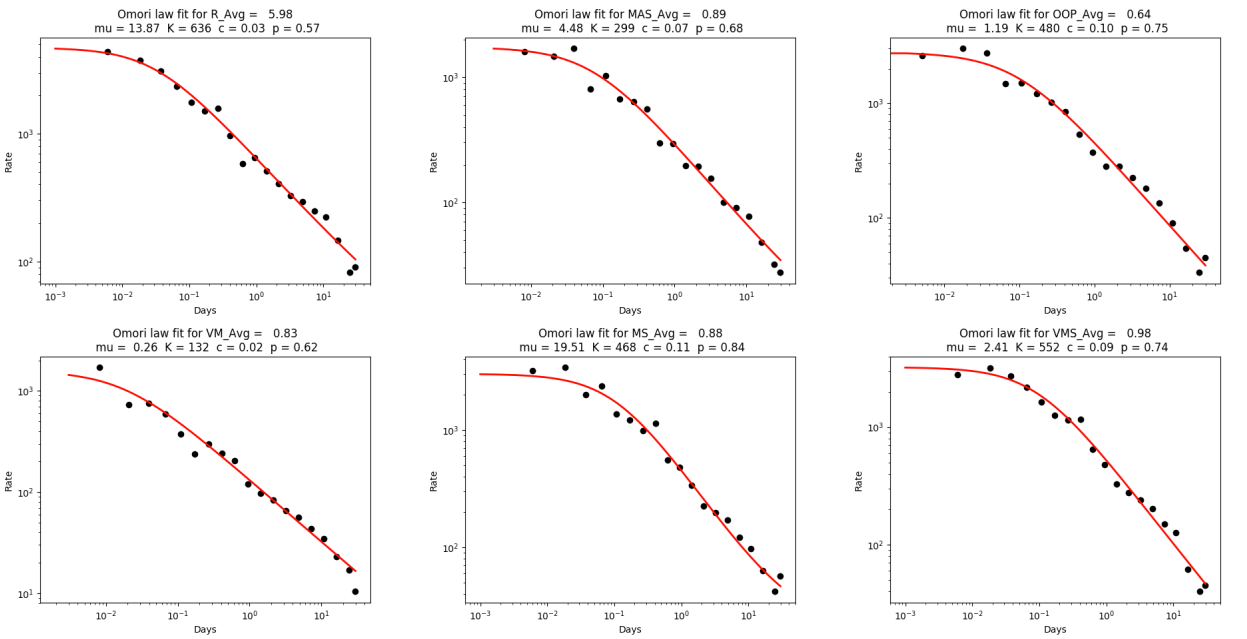

Figure S9: Examples of OU law fits.

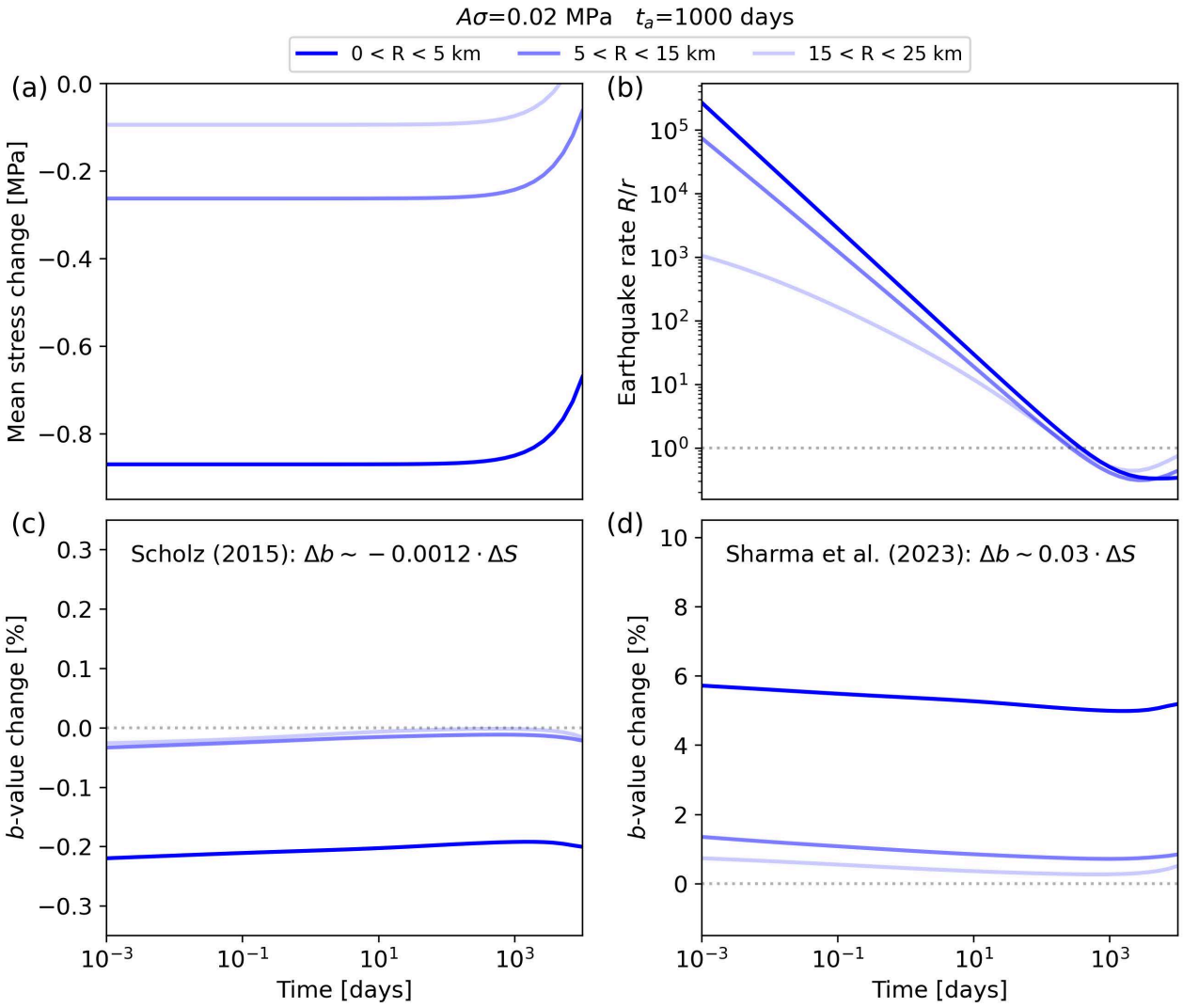

Figure S10: Results for a synthetic M7.0 strike-slip earthquake: (a) Average stress changes at three different distance ranges to the rupture plane. Note that the result is identical for shear stress and MAS values. (b) The corresponding normalized earthquake rates, assuming the CRS model. (c, d) The resulting b-value changes (in percent) using either the relation from (c) Scholz (2015) or (d) this paper. Gulia et al. (2018) observed a mainshock-induced b-value increase that remains almost constant with time, in general agreement with (d) and in contrast to panel (c).

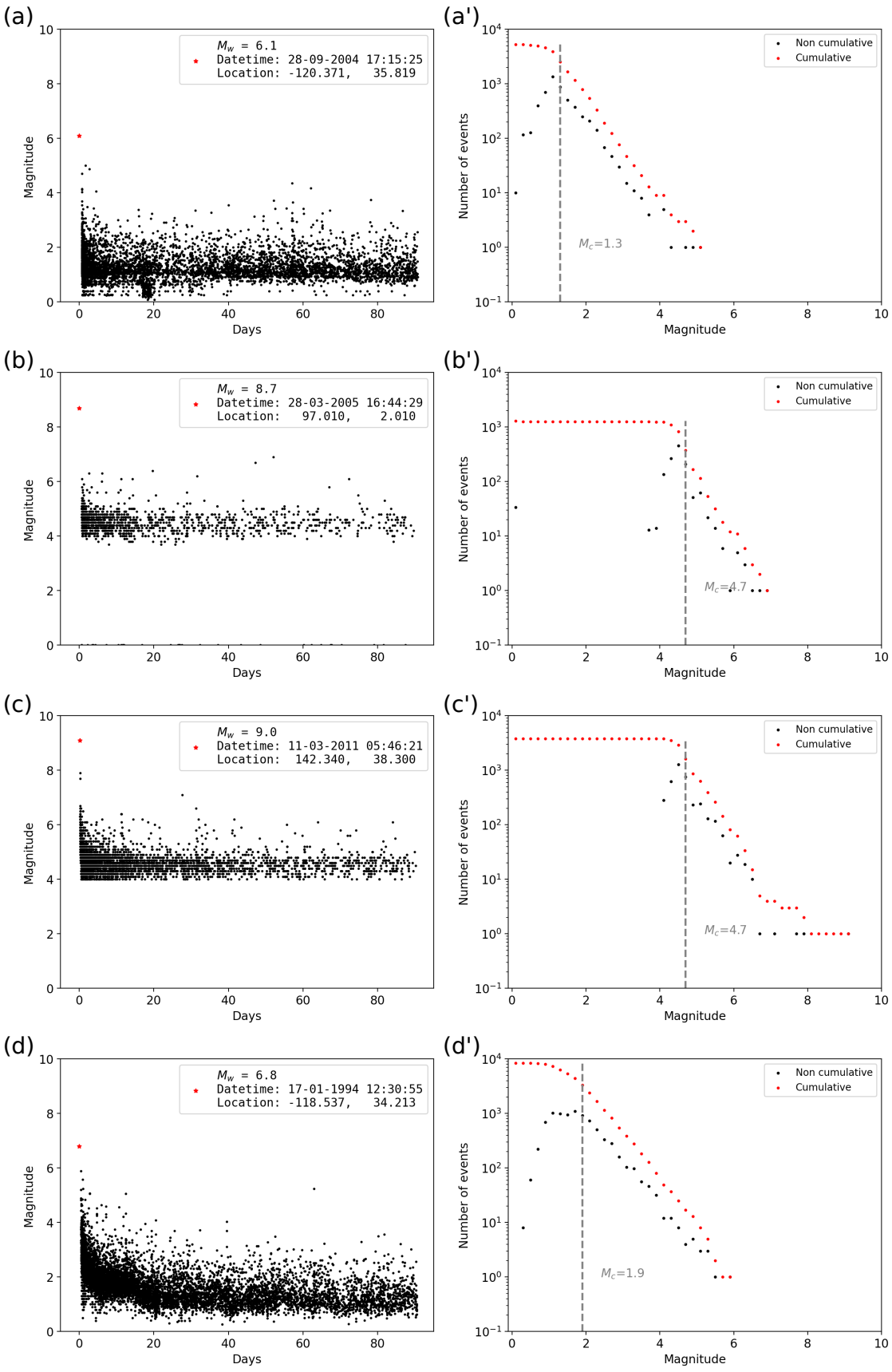

Figure S11: Four exemplary mainshock-aftershock sequences. Left column: Earthquake magnitudes as a function of the time relative to the mainshock, where the mainshock information is provided in the legend. Right column: Frequency-magnitude distribution, where the vertical dashed line indicates the chosen minimum completeness magnitude $M_{c,0}$.

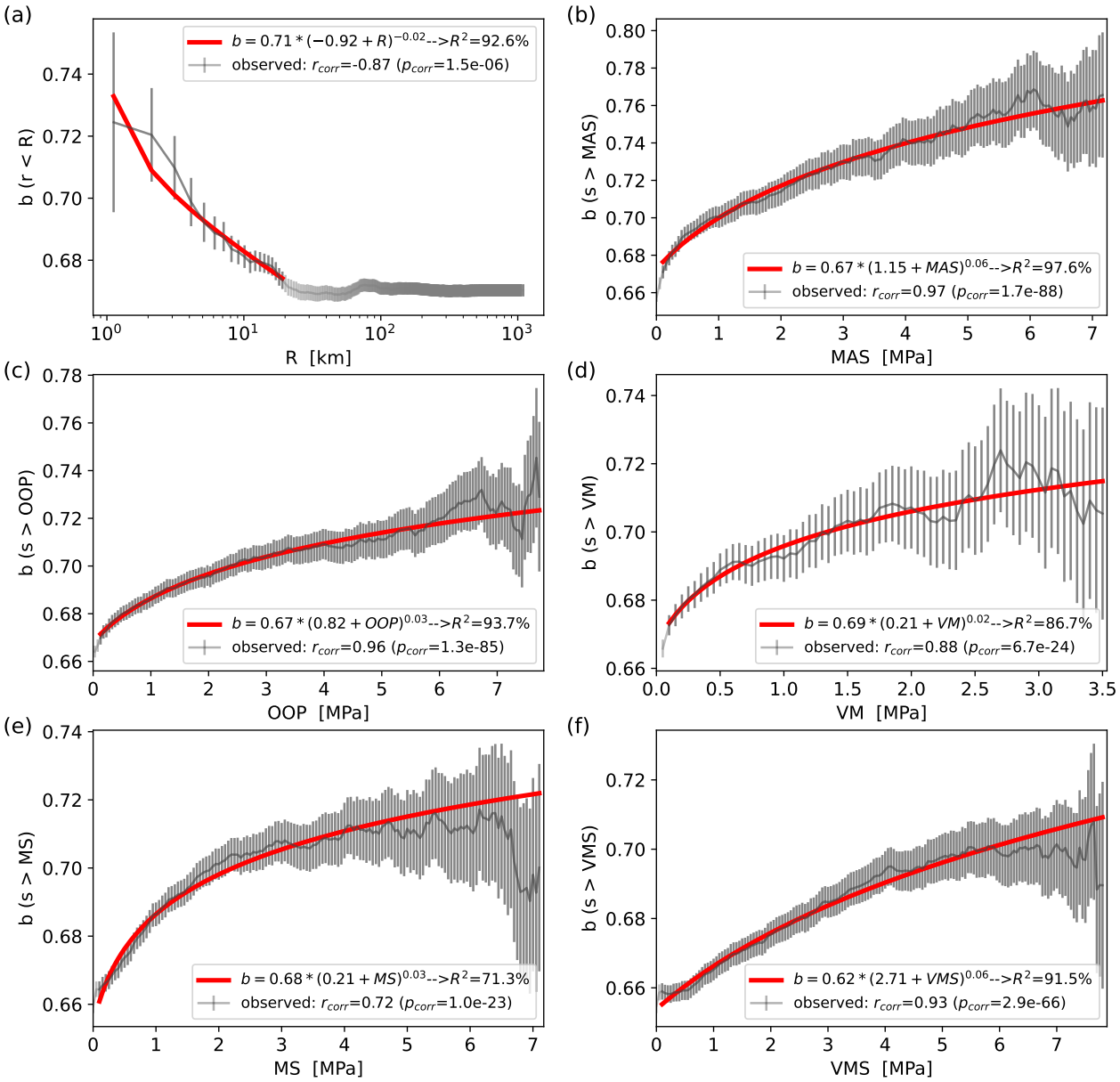

Figure S12: The same as manuscript Fig. 2 but considering only aftershocks with magnitudes exceeding $M_{c,0} + 0.2$.

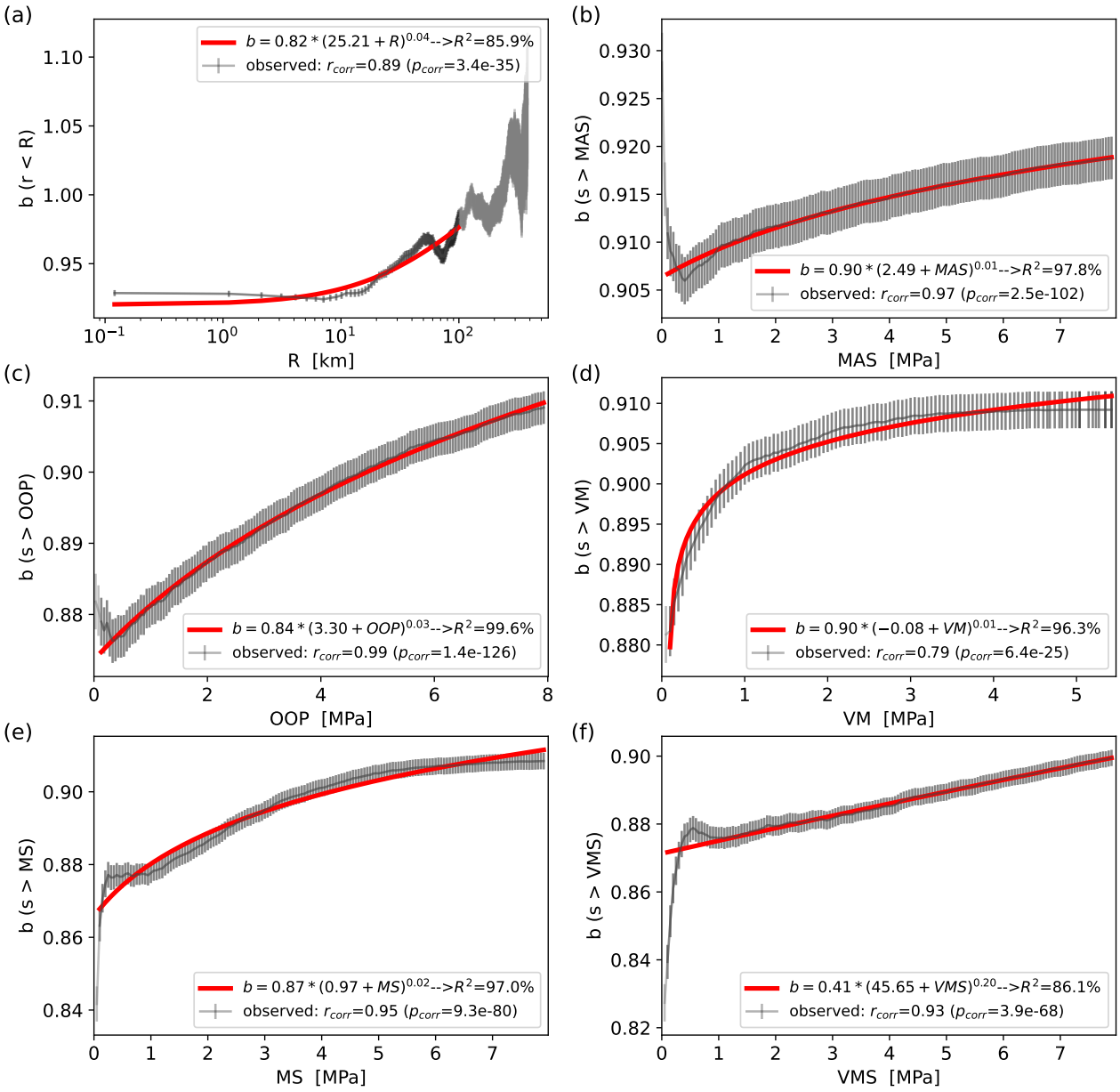

Figure S13: The same as manuscript Fig. 2 but for aftershocks with distances larger, respectively stress lower than the values given at the x-scale of the panels.

Bibliography

Ader, T., Avouac, J.-P., Liu-Zeng, J., Lyon-Caen, H., Bollinger, L., Galetzka, J., Genrich, J., Thomas, M., Chanard, K., Sapkota, S. N., et al. (2012). Convergence rate across the nepal himalaya and interseismic coupling on the main himalayan thrust: Implications for seismic hazard. *Journal of Geophysical Research: Solid Earth*, 117(B4).

Aki, K. (1965). Maximum likelihood estimate of b in the formula log n = a-bm and its confidence limits. *Bull. Earthq. Res. Inst., Tokyo Univ.*, 43:237–239.

Allmann, B. P. and Shearer, P. M. (2009a). Global variations of stress drop for moderate to large earthquakes. *Journal of Geophysical Research: Solid Earth*, 114(B1).

Allmann, B. P. and Shearer, P. M. (2009b). Global variations of stress drop for moderate to large earthquakes. *Journal of Geophysical Research*, 114:B01310.

Armbruster, J., Seeber, L., and Jacob, K. (1978). The northwestern termination of the himalayan mountain front: active tectonics from microearthquakes. *Journal of Geophysical Research: Solid Earth*, 83(B1):269–282.

Asayesh, B. M., Zafarani, H., Hainzl, S., and Sharma, S. (2023). Effects of large aftershocks on spatial aftershock forecasts during the 2017–2019 western iran sequence. *Geophysical Journal International*, 232(1):147–161.

Avouac, J.-P. (2003). Mountain building, erosion, and the seismic cycle in the nepal himalaya. *Advances in geophysics*, 46:1–80.

Avouac, J.-P., Ayoub, F., Leprince, S., Konca, O., and Helmberger, D. V. (2006). The 2005, mw 7.6 kashmir earthquake: Sub-pixel correlation of aster images and seismic waveforms analysis. *Earth and Planetary Science Letters*, 249(3-4):514–528.

Bach, C. and Hainzl, S. (2012). Improving empirical aftershock modeling based on additional source information. *Journal of Geophysical Research: Solid Earth*, 117(B4).

Bassin, C. (2000). The current limits of resolution for surface wave tomography in north america. *EOS Trans. AGU. 81: Fall Meet. Suppl., Abstract.*

Bendick, R., Bilham, R., Khan, M. A., and Khan, S. F. (2007). Slip on an active wedge thrust from geodetic observations of the 8 october 2005 kashmir earthquake. *Geology*, 35(3):267–270.

Berberian, M., Jackson, J., Qorashi, M., Khatib, M., Priestley, K., Talebian, M., and Ghafuri-Ashtiani, M. (1999). The 1997 may 10 zirkuh (qa'enat) earthquake (m w 7.2): faulting along the sistan suture zone of eastern iran. *Geophysical Journal International*, 136(3):671–694.

Bilham, R. et al. (2004). Earthquakes in india and the himalaya: tectonics, geodesy and history. *Annals of GEOPHYSICS*.

Cao, A. and Gao, S. S. (2002). Temporal variation of seismic b-values beneath northeastern Japan island arc. *Geophysical Research Letters*, 29(9):48–1.

Cao, C., Wu, X., Yang, L., Zhang, Q., Wang, X., Yuen, D. A., and Luo, G. (2021). Long short-term memory networks for pattern recognition of synthetical complete earthquake catalog. *Sustainability*, 13(9):4905.

Cattania, C., Hainzl, S., Wang, L., Enescu, B., and Roth, F. (2015). Aftershock triggering by postseismic stresses: A study based on Coulomb rate-and-state models. *Journal of Geophysical Research: Solid Earth*, 120(4):2388–2407.

Cattania, C., Hainzl, S., Wang, L., Roth, F., and Enescu, B. (2014). Propagation of Coulomb stress uncertainties in physics-based aftershock models. *Journal of Geophysical Research: Solid Earth*, 119(10):7846–7864.

Cattania, C., Werner, M. J., Marzocchi, W., Hainzl, S., Rhoades, D., Gerstenberger, M., Liukis, M., Savran, W., Christophersen, A., Helmstetter, A., et al. (2018). The forecasting skill of physics-based seismicity models during the 2010–2012 canterbury, new zealand, earthquake sequence. *Seismological Research Letters*, 89(4):1238–1250.

Cocco, M., Hainzl, S., Catalli, F., Enescu, B., Lombardi, A., and Woessner, J. (2010). Sensitivity study of forecasted aftershock seismicity based on Coulomb stress calculation and rate-and state-dependent frictional response. *Journal of Geophysical Research: Solid Earth*, 115(B5).

Cocco, M. and Rice, J. R. (2002). Pore pressure and poroelasticity effects in Coulomb stress analysis of earthquake interactions. *Journal of Geophysical Research: Solid Earth*, 107(B2):ESE–2.

DeVries, P. M., Viégas, F., Wattenberg, M., and Meade, B. J. (2018). Deep learning of aftershock patterns following large earthquakes. *Nature*, 560(7720):632.

Dieterich, J. (1994). A constitutive law for rate of earthquake production and its application to earthquake clustering. *Journal of Geophysical Research: Solid Earth*, 99(B2):2601–2618.

Dieterich, J., Cayol, V., and Okubo, P. (2000). The use of earthquake rate changes as a stress meter at kilauea volcano. *Nature*, 408(6811):457–460.

Dziewonski, A. M., Chou, T.-A., and Woodhouse, J. H. (1981). Determination of earthquake source parameters from waveform data for studies of global and regional seismicity. *Journal of Geophysical Research: Solid Earth*, 86(B4):2825–2852.

Ekström, G., Nettles, M., and Dziewoński, A. (2012). The global cmt project 2004–2010: Centroid-moment tensors for 13,017 earthquakes. *Physics of the Earth and Planetary Interiors*, 200:1–9.

El-Isa, Z. (2013). Continuous-cyclic variations in the b-value of the earthquake frequency-magnitude distribution. *Earthquake Science*, 26:301–320.

El-Isa, Z. H. and Eaton, D. W. (2014). Spatiotemporal variations in the b-value of earthquake magnitude–frequency distributions: Classification and causes. *Tectonophysics*, 615:1–11.

Felzer, K. R. and Brodsky, E. E. (2005). Testing the stress shadow hypothesis. *Journal of Geophysical Research: Solid Earth*, 110(B5).

Felzer, K. R. and Brodsky, E. E. (2006). Decay of aftershock density with distance indicates triggering by dynamic stress. *Nature*, 441(7094):735.

Frohlich, C. and Davis, S. D. (1993). Teleseismic b values; or, much ado about 1.0. *Journal of Geophysical Research: Solid Earth*, 98(B1):631–644.

Gavillot, Y., Meigs, A., Yule, D., Heermance, R., Rittenour, T., Madugo, C., and Malik, M. (2016). Shortening rate and holocene surface rupture on the riasi fault system in the kashmir himalaya: active thrusting within the northwest himalayan orogenic wedge. *Bulletin*, 128(7-8):1070–1094.

Gerstenberger, M. C., Wiemer, S., Jones, L. M., and Reasenberg, P. A. (2005). Real-time forecasts of tomorrow's earthquakes in California. *Nature*, 435(7040):328–331.

Gross, S. (2001). A model of tectonic stress state and rate using the 1994 northridge earthquake sequence. *Bulletin of the Seismological Society of America*, 91(2):263–275.

Gross, S. and Kisslinger, C. (1997). Estimating tectonic stress rate and state with landers aftershocks. *Journal of Geophysical Research: Solid Earth*, 102(B4):7603–7612.

Gu, C., Schumann, A. Y., Baiesi, M., and Davidsen, J. (2013). Triggering cascades and statistical properties of aftershocks. *Journal of Geophysical Research: Solid Earth*, 118(8):4278–4295.

Gulia, L., Rinaldi, A. P., Tormann, T., Vannucci, G., Enescu, B., and Wiemer, S. (2018). The effect of a mainshock on the size distribution of the aftershocks. *Geophysical Research Letters*, 45(24):13–277.

Gulia, L. and Wiemer, S. (2019). Real-time discrimination of earthquake foreshocks and aftershocks. *Nature*, 574(7777):193–199.

Gutenberg, B. and Richter, C. F. (1944). Frequency of earthquakes in California. *Bulletin of the Seismological society of America*, 34(4):185–188.

Hainzl, S. (2016). Rate-dependent incompleteness of earthquake catalogs. *Seismological Research Letters*, 87(2A):337–344.

Hainzl, S., Brietzke, G. B., and Zöller, G. (2010a). Quantitative earthquake forecasts resulting from static stress triggering. *Journal of Geophysical Research: Solid Earth*, 115(B11).

Hainzl, S., Enescu, B., Cocco, M., Woessner, J., Catalli, F., Wang, R., and Roth, F. (2009). Aftershock modeling based on uncertain stress calculations. *Journal of Geophysical Research: Solid Earth*, 114(B5).

Hainzl, S. and Marsan, D. (2008). Dependence of the omori-utsu law parameters on main shock magnitude: Observations and modeling. *Journal of Geophysical Research: Solid Earth*, 113(B10).

Hainzl, S., Zöller, G., and Wang, R. (2010b). Impact of the receiver fault distribution on aftershock activity. *Journal of Geophysical Research: Solid Earth*, 115(B5).

Harris, R. A. (1998). Introduction to special section: Stress triggers, stress shadows, and implications for seismic hazard. *Journal of Geophysical Research: Solid Earth*, 103(B10):24347–24358.

Harris, R. A. and Simpson, R. W. (2002). The 1999 m w 7.1 hector mine, California, earthquake: a test of the stress shadow hypothesis? *Bulletin of the Seismological Society of America*, 92(4):1497–1512.

Helmstetter, A., Kagan, Y. Y., and Jackson, D. D. (2005). Importance of small earthquakes for stress transfers and earthquake triggering. *Journal of Geophysical Research: Solid Earth*, 110(B5).

Helmstetter, A., Kagan, Y. Y., and Jackson, D. D. (2006). Comparison of short-term and time-independent earthquake forecast models for southern California. *Bulletin of the Seismological Society of America*, 96(1):90–106.

Helmstetter, A. and Shaw, B. E. (2006). Relation between stress heterogeneity and aftershock rate in the rate-and-state model. *Journal of Geophysical Research: Solid Earth*, 111(B7).

Huang, J., Wang, X., Zhao, Y., Xin, C., and Xiang, H. (2018). Large earthquake magnitude prediction in taiwan based on deep learning neural network. *Neural Network World*, 28(2):149–160.

Ishii, M., Shearer, P. M., Houston, H., and Vidale, J. E. (2007). Teleseismic p wave imaging of the 26 december 2004 sumatra-andaman and 28 march 2005 sumatra earthquake ruptures using the hi-net array. *Journal of Geophysical Research: Solid Earth*, 112(B11).

Iwata, T. (2016). A variety of aftershock decays in the rate and state-friction model due to the effect of secondary aftershocks: Implications derived from an analysis of real aftershock sequences. *Pure Appl. Geophys.*, 173:21–33.

Jackson, J. and Yielding, G. (1983). The seismicity of kohistan, pakistan: source studies of the hamran (1972.9. 3), darel (1981.9. 12) and patan (1974.12. 28) earthquakes. *Tectonophysics*, 91(1-2):15–28.

Jordan, T. H. (2006). Earthquake predictability, brick by brick. *Seismological Research Letters*, 77(1):3–6.

Jordan, T. H. and Sverdrup, K. A. (1981). Teleseismic location techniques and their application to earthquake clusters in the south-central pacific. *Bulletin of the Seismological Society of America*, 71(4):1105–1130.

Kagan, Y. Y. (2004). Short-term properties of earthquake catalogs and models of earthquake source. *Bulletin of the Seismological Society of America*, 94(4):1207–1228.

Kennett, B. and Engdahl, E. (1991). Traveltimes for global earthquake location and phase identification. *Geophysical Journal International*, 105(2):429–465.

Khan, P. K., Mohanty, S., and Mohanty, M. (2010). Geodynamic implications for the 8 october 2005 north pakistan earthquake. *Surveys in geophysics*, 31:85–106.

Kim, Y.-S., Peacock, D. C., and Sanderson, D. J. (2004). Fault damage zones. *Journal of Structural Geology*, 26(3):503–517.

King, G. C., Stein, R. S., and Lin, J. (1994). Static stress changes and the triggering of earthquakes. *Bulletin of the Seismological Society of America*, 84(3):935–953.

Kiser, E. and Ishii, M. (2012). Combining seismic arrays to image the high-frequency characteristics of large earthquakes. *Geophysical Journal International*, 188(3):1117–1128.

Kiser, E., Ishii, M., Langmuir, C. H., Shearer, P., and Hirose, H. (2011). Insights into the mechanism of intermediate-depth earthquakes from source properties as imaged by back projection of multiple seismic phases. *Journal of Geophysical Research: Solid Earth*, 116(B6).

Kumar, A., Singh, S. K., Mitra, S., Priestley, K., and Dayal, S. (2017). The 2015 april 25 gorkha (nepal) earthquake and its aftershocks: implications for lateral heterogeneity on the main himalayan thrust. *Geophysical Journal International*, 208(2):992–1008.

Ma, K.-F., Mori, J., Lee, S.-J., and Yu, S. (2001). Spatial and temporal distribution of slip for the 1999 chi-chi, taiwan, earthquake. *Bulletin of the Seismological Society of America*, 91(5):1069–1087.

Mai, P. M. and Thingbaijam, K. (2014). SRCMOD: An online database of finite-fault rupture models. *Seismological Research Letters*, 85(6):1348–1357.

Marsan, D. (2006). Can coseismic stress variability suppress seismicity shadows? insights from a rate-and-state friction model. *Journal of Geophysical Research: Solid Earth*, 111(B6).

McCaffrey, R. and Nabelek, J. (1987). Earthquakes, gravity, and the origin of the bali basin: an example of a nascent continental fold-and-thrust belt. *Journal of Geophysical Research: Solid Earth*, 92(B1):441–460.

Meade, B. J., DeVries, P. M., Faller, J., Viegas, F., and Wattenberg, M. (2017). What is better than Coulomb failure stress? a ranking of scalar static stress triggering mechanisms from 105 mainshock-aftershock pairs. *Geophysical Research Letters*, 44(22):11–409.

Mignan, A. (2018). Utsu aftershock productivity law explained from geometric operations on the permanent static stress field of mainshocks. *Nonlinear Processes in Geophysics*, 25(1):241–250.

Mignan, A. (2020). Forecasting aftershocks: Back to square one after a deep learning anticlimax. *Temblor*.

Mignan, A. and Broccardo, M. (2019). One neuron versus deep learning in aftershock prediction. *Nature*, 574(7776):E1–E3.

Mignan, A. and Broccardo, M. (2020). Comment on "elastic strain energy and pore-fluid pressure control of aftershocks" by terakawa et al.[earth planet. sci. lett. 535 (2020) 116103]. *Earth and Planetary Science Letters*, 544:116402.

Mitra, S., Wanchoo, S., and Priestley, K. (2014). Source parameters of the 1 may 2013 mb 5.7 kishtwar earthquake: Implications for seismic hazards. *Bulletin of the Seismological Society of America*, 104(2):1013–1019.

Moradpour, J., Hainzl, S., and Davidsen, J. (2014). Nontrivial decay of aftershock density with distance in southern california. *Journal of Geophysical Research: Solid Earth*, 119(7):5518–5535.

Mori, J. and Abercrombie, R. E. (1997). Depth dependence of earthquake frequency-magnitude distributions in California: Implications for rupture initiation. *Journal of Geophysical Research: Solid Earth*, 102(B7):15081–15090.

Nanjo, K., Hirata, N., Obara, K., and Kasahara, K. (2012). Decade-scale decrease inb value prior to the m9-class 2011 tohoku and 2004 sumatra quakes. *Geophysical Research Letters*, 39(20).

Nanjo, K. and Yoshida, A. (2021). Changes in the b value in and around the focal areas of the m 6.9 and m 6.8 earthquakes off the coast of miyagi prefecture, japan, in 2021. *Earth, Planets and Space*, 73:1–10.

Narteau, C., Byrdina, S., Shebalin, P., and Schorlemmer, D. (2009). Common dependence on stress for the two fundamental laws of statistical seismology. *Nature*, 462(7273):642–645.

Ogata, Y. (1988). Statistical models for earthquake occurrences and residual analysis for point processes. *Journal of the American Statistical association*, 83(401):9–27.

Ogata, Y., Imoto, M., and Katsura, K. (1991). 3-d spatial variation of b-values of magnitude-frequency distribution beneath the Kanto district, Japan. *Geophysical Journal International*, 104(1):135–146.

Okada, Y. (1992). Internal deformation due to shear and tensile faults in a half-space. *Bulletin of the Seismological Society of America*, 2(2):1018–1040.

Omori, F. (1895). *On the after-shocks of earthquakes*. PhD thesis, The University of Tokyo.

Parsons, T. (2020). On the use of receiver operating characteristic tests for evaluating spatial earthquake forecasts. *Geophysical Research Letters*, page e2020GL088570.

Parsons, T., Stein, R. S., Simpson, R. W., and Reasenberg, P. A. (1999). Stress sensitivity of fault seismicity: A comparison between limited-offset oblique and major strike-slip faults. *Journal of Geophysical Research: Solid Earth*, 104(B9):20183–20202.

Parsons, T., Yeats, R. S., Yagi, Y., and Hussain, A. (2006). Static stress change from the 8 october, 2005 m= 7.6 kashmir earthquake. *Geophysical Research Letters*, 33(6).

Pathier, E., Fielding, E., Wright, T., Walker, R., Parsons, B., and Hensley, S. (2006). Displacement field and slip distribution of the 2005 kashmir earthquake from sar imagery. *Geophysical research letters*, 33(20).

Paul, H., Mitra, S., Bhattacharya, S., and Suresh, G. (2015). Active transverse faulting within underthrust indian crust beneath the sikkim himalaya. *Geophysical Journal International*, 201(2):1072–1083.

Paul, H., Priestley, K., Powali, D., Sharma, S., Mitra, S., and Wanchoo, S. (2018). Signatures of the existence of frontal and lateral ramp structures near the kishtwar window of the jammu and kashmir himalaya: evidence from microseismicity and source mechanisms. *Geochemistry, Geophysics, Geosystems*, 19(9):3097–3114.

Powers, P. M. and Jordan, T. H. (2010). Distribution of seismicity across strike-slip faults in California. *Journal of Geophysical Research: Solid Earth*, 115(B5).

Prejean, S., Hill, D., Brodsky, E., Hough, S., Johnston, M., Malone, S., Oppenheimer, D., Pitt, A., and Richards-Dinger, K. (2004). Remotely triggered seismicity on the united states west coast following the m w 7.9 denali fault earthquake. *Bulletin of the Seismological Society of America*, 94(6B):S348–S359.

Quittmeyer, R. and Jacob, K. (1979). Historical and modern seismicity of pakistan, afghanistan, northwestern india, and southeastern iran. *Bulletin of the Seismological Society of America*, 69(3):773–823.

Ridzwan, N. S. M. and Yusoff, S. H. M. (2023). Machine learning for earthquake prediction: a review (2017–2021). *Earth Science Informatics*, pages 1–17.

Schiffman, C., Bali, B. S., Szeliga, W., and Bilham, R. (2013). Seismic slip deficit in the kashmir himalaya from gps observations. *Geophysical Research Letters*, 40(21):5642–5645.

Scholz, C. H. (1968). The frequency-magnitude relation of microfracturing in rock and its relation to earthquakes. *Bulletin of the Seismological Society of America*, 58(1):399–415.

Scholz, C. H. (2015). On the stress dependence of the earthquake b value. *Geophysical Research Letters*, 42(5):1399–1402.

Schorlemmer, D., Wiemer, S., and Wyss, M. (2005). Variations in earthquake-size distribution across different stress regimes. *Nature*, 437(7058):539–542.

Seeber, L. and Armbruster, J. G. (1981). Great detachment earthquakes along the himalayan arc and long-term forecasting. *Earthquake prediction: an international review*, 4:259–277.

Seeber, L. et al. (1980). Seismotectonics of pakistan: A review of results from network data and implications for the central himalaya.

Shao, G. and Ji, C. (2005). Preliminary result of the oct 8, 2005 mw 7.64 pakistan earthquake. *UCSB http://www. geol. ucsb. edu/faculty/ji/big_earthquakes/2005/10/smooth/2005pakistan. html (accessed 2 June 2018)*.

Sharma, S., Hainzl, S., Zöeller, G., and Holschneider, M. (2020). Is Coulomb stress the best choice for aftershock forecasting? *Journal of Geophysical Research: Solid Earth*, 125(9):e2020JB019553.

Smirnov, V., Ponomarev, A., Stanchits, S., Potanina, M., Patonin, A., Dresen, G., Narteau, C., Bernard, P., and Stroganova, S. (2019). Laboratory modeling of aftershock sequences: stress dependences of the Omori and Gutenberg–Richter parameters. *Izvestiya, Physics of the Solid Earth*, 55(1):124–137.

Smith, W. D. (1981). The b-value as an earthquake precursor. *Nature*, 289(5794):136–139.

Spada, M., Tormann, T., Wiemer, S., and Enescu, B. (2013). Generic dependence of the frequency-size distribution of earthquakes on depth and its relation to the strength profile of the crust. *Geophysical Research Letters*, 40(4):709–714.

Steacy, S., Gerstenberger, M., Williams, C., Rhoades, D., and Christophersen, A. (2013). A new hybrid Coulomb/statistical model for forecasting aftershock rates. *Geophysical Journal International*, 196(2):918–923.

Steacy, S., Gomberg, J., and Cocco, M. (2005a). Introduction to special section: Stress transfer, earthquake triggering, and time-dependent seismic hazard. *Journal of Geophysical Research: Solid Earth*, 110(B5).

Steacy, S., Marsan, D., Nalbant, S. S., and McCloskey, J. (2004). Sensitivity of static stress calculations to the earthquake slip distribution. *Journal of Geophysical Research: Solid Earth*, 109(B4).

Steacy, S., Nalbant, S. S., McCloskey, J., Nostro, C., Scotti, O., and Baumont, D. (2005b). Onto what planes should Coulomb stress perturbations be resolved? *Journal of geophysical research: Solid Earth*, 110(B5).

Steacy, S., Nalbant, S. S., McCloskey, J., Nostro, C., Scotti, O., and Baumont, D. (2005c). Onto what planes should Coulomb stress perturbations be resolved? *Journal of Geophysical Research: Solid Earth*, 110:B05S15.

Stein, R. S. (1999). The role of stress transfer in earthquake occurrence. *Nature*, 402(6762):605.

Stramondo, S., Kyriakopoulos, C., Bignami, C., Chini, M., Melini, D., Moro, M., Picchiani, M., Saroli, M., and Boschi, E. (2011). Did the september 2010 (darfield) earthquake trigger the february 2011 (christchurch) event? *Scientific reports*, 1:98.

Tahir, M. and Grasso, J. R. (2015). Faulting style controls for the space–time aftershock patterns. *Bulletin of the Seismological Society of America*, 105(5):2480–2497.

Terakawa, T., Matsu'ura, M., and Noda, A. (2020). Elastic strain energy and pore-fluid pressure control of aftershocks. *Earth and Planetary Science Letters*, 535:116103.

Toda, S., Stein, R. S., Reasenberg, P. A., Dieterich, J. H., and Yoshida, A. (1998). Stress transferred by the 1995 mw= 6.9 kobe, Japan, shock: Effect on aftershocks and future earthquake probabilities. *Journal of Geophysical Research: Solid Earth*, 103(B10):24543–24565.

Toda, S., Stein, R. S., and Sagiya, T. (2002). Evidence from the ad 2000 izu islands earthquake swarm that stressing rate governs seismicity. *Nature*, 419(6902):58–61.

Utsu, T., Ogata, Y., et al. (1995). The centenary of the Omori formula for a decay law of aftershock activity. *Journal of Physics of the Earth*, 43(1):1–33.

Wadia, D. (1931). The syntaxis of the northwest himalaya: its rocks, tectonics and orogeny. *Rec. Geol. Surv. India*, 65(2):189–220.

Wang, R., Lorenzo-Martín, F., and Roth, F. (2006). PSGRN/PSCMP–a new code for calculating co-and post-seismic deformation, geoid and gravity changes based on the viscoelastic-gravitational dislocation theory. *Computers & Geosciences*, 32(4):527–541.

Wells, D. L. and Coppersmith, K. J. (1994). New empirical relationships among magnitude, rupture length, rupture width, rupture area, and surface displacements. *Bulletin of the Seismological Society of America*, 84(4):974–1002.

Wiemer, S. and Katsumata, K. (1999). Spatial variability of seismicity parameters in aftershock zones. *Journal of Geophysical Research: Solid Earth*, 104(B6):13135–13151.

Wiemer, S. and Wyss, M. (2000). Minimum magnitude of completeness in earthquake catalogs: Examples from Alaska, the western United States, and Japan. *Bulletin of the Seismological Society of America*, 90(4):859–869.

Wyss, M. et al. (1973). Towards a physical understanding of the earthquake frequency distribution. *Geophys. JR Astron. Soc*, 31(4):341–359.

Zhuang, J., Harte, D., Werner, M. J., Hainzl, S., and Zhou, S. (2012). Basic models of seismicity: Temporal models. *Community Online Resource for Statistical Seismicity Analysis*, 5.